Air Force Institute of Technology
AFIT Scholar

Theses and Dissertations | Student Graduate Works

9-2019

Effects of Carbon-based Ablation Products on Hypersonic Boundary Layer Stability

Olivia S. Elliott

Follow this and additional works at: https://scholar.afit.edu/etd

 Part of the Aerospace Engineering Commons, and the Engineering Science and Materials Commons

Recommended Citation

Elliott, Olivia S., "Effects of Carbon-based Ablation Products on Hypersonic Boundary Layer Stability" (2019). *Theses and Dissertations*. 2374.
https://scholar.afit.edu/etd/2374

This Dissertation is brought to you for free and open access by the Student Graduate Works at AFIT Scholar. It has been accepted for inclusion in Theses and Dissertations by an authorized administrator of AFIT Scholar. For more information, please contact AFIT.ENWL.Repository@us.af.mil.

Effects of Carbon-based Ablation Products on Hypersonic Boundary Layer Stability

DISSERTATION

Olivia S. Elliott, Lt Col, USAF

AFIT-ENY-DS-19-S-074

DEPARTMENT OF THE AIR FORCE
AIR UNIVERSITY

AIR FORCE INSTITUTE OF TECHNOLOGY

Wright-Patterson Air Force Base, Ohio

DISTRIBUTION STATEMENT A. APPROVED FOR PUBLIC RELEASE;

DISTRIBUTION IS UNLIMITED

The views expressed in this document are those of the author and do not reflect the official policy or position of the United States Air Force, the United States Department of Defense or the United States Government. This is an academic work and should not be used to imply or infer actual mission capability or limitations.

AFIT-ENY-DS-19-S-074

EFFECTS OF CARBON-BASED ABLATION PRODUCTS ON HYPERSONIC BOUNDARY LAYER STABILITY

DISSERTATION

Presented to the Faculty
Graduate School of Engineering and Management
Air Force Institute of Technology
Air University
Air Education and Training Command
in Partial Fulfillment of the Requirements for the
Degree of Doctor of Philosophy

Olivia S. Elliott, B.S., M.Phil, M.A., M.Sc.
Lt Col, USAF

September 2019

DISTRIBUTION STATEMENT A. APPROVED FOR PUBLIC RELEASE;
DISTRIBUTION IS UNLIMITED

AFIT-ENY-DS-19-S-074

EFFECTS OF CARBON-BASED ABLATION PRODUCTS ON HYPERSONIC BOUNDARY LAYER STABILITY

Olivia S. Elliott, B.S., M.Phil, M.A., M.Sc.
Lt Col, USAF

Approved:

//signed//	24 July 2019
Dr. Robert B. Greendyke, PhD Chairman	Date
//signed//	19 Aug 2019
Lt Col Jeffrey R. Komives, PhD Member	Date
//signed//	23 Aug 2019
Dr. Kevin C. Gross, PhD Member	Date
//signed//	21 Aug 2019
Dr. Mark F. Reeder, PhD Member	Date

Accepted:

//signed//	23 Aug 2019
Adedeji B. Badiru Dean, Graduate School of Engineering and Management	Date

Abstract

One of the technical challenges that face designers of hypersonic vehicles is the high thermal loads that theses vehicles encounter in flight. The Thermal Protection System (TPS) is the main system which deals with these high thermal loads. The dominant factor affecting the TPS design is the predicted transition location and characteristics as turbulent boundary layers can produce up to ten times higher thermal loads than laminar boundary layers [1]. The heating rates of turbulent boundary layers and the length of flight time under turbulent boundary layer conditions drives the material choice and thickness of thermal protection system. The materials used for the thermal protection systems, along with many other factors, affects the stability and transition of the boundary layer. Many thermal protection systems use ablation as a means of dissipating thermal energy. These systems add new species to the boundary layer changing the chemistry and introduce instabilities with the blowing of mass into the flow. Carbon-based ablators in particular have gained popularity due to their ablative characteristics. The addition of carbon species, specifically CO_2, into a hypersonic boundary layer has the known effect of damping out second mode instabilities at hypersonic flight conditions due to the ability of CO_2 to absorb disturbance energy into the multiple vibrational modes.

Using current gas-surface chemistry models and controlled freestream CO_2 concentrations, the effect of CO_2 on the stability was examined over both sharp and blunt cones. A concentration study was conducted to determine the required CO_2 concentration in the boundary layer to effect transition characteristics. The boundary layer was saturated at a specific CO_2 concentration, and it was held constant throughout the boundary layer. The results of the concentration study showed that, due to the

higher temperatures in the boundary layer of a blunt cone, lower concentrations of CO_2 were required to obtain the same delay in transition as compared to a sharp cone. Also, as the enthalpy of the flow increased, lower concentrations of CO_2 were required to obtain the same transition delay, highilighting the importance of boundary layer temperature on the effects of CO_2 damping.

An examination of the current air-carbon gas-surface interaction models was also conducted to determine if ablation provided sufficient concentrations of CO_2 in the boundary layer. The gas-surface interaction models currently used for carbon-based ablators include the Park76, Park, Zhluktov and Abe, Modified Zhluktov and Abe, Zhluktov and Abe with nitridation and a MURI carbon oxidation model. Study results showed that the ablation models can produce sufficient concentrations of CO_2 in the boundary layer to affect transition location. However, the actual efficacy of CO_2 damping depends on the freestream conditions, the boundary layer temperature profile and the geometry of the vehicle. Flows with higher enthalpy over a blunt cone showed the greatest delay in transition due to CO_2 damping.

The stability of the boundary layer is complex, with interdependence of multiple factors. Furthermore, uncertainties exist in the air-carbon gas-surface interaction models which affect the production of CO_2 on the surface and in the gas. Therefore, a parametric study of the interplay between freestream flight conditions based on altitude, surface temperature and the gas-surface interaction model parameters was completed to determine the sensitivity of the boundary layer to these changes. The effect of increased surface temperature showed that there existed a complex interplay between the amount of CO_2 created and the surface temperature which stabilized the boundary layer and the increased mass flux from a hotter surface that destabilized the boundary layer. Overall, the higher surface temperature increased the stability of the flow even though it did not always increase the total CO_2 concentration. The

site density parameter controls the number of adsorbed surface reactions that can occur. This parameter is not well characterized based on material or experimental data and is usually arbitrarily chosen for the simulation. Each model responded differently to a change in this parameter, but the overall stability of the boundary layer remained basically insensitive to these changes due, again, to the competing mechanisms of increased CO_2 damping versus the destabilization of increased mass flux. The altitude parameter study was conducted using typical reentry trajectory characteristics and standard atmospheric conditions [2]. The results of the altitude parameter study showed an increased efficacy of CO_2 damping as altitude decreased to approximately 40,000 ft in altitude. Below this altitude, second mode instabilities became less dominant in the boundary layer and CO_2 damping was no longer effective.

To my wonderful husband for his unfailing support and to my children for reminding me of what is important in life.

Acknowledgements

I want to thank Dr. Greendyke for his exceptional patience, direction and dedication to this research. I want to thank Lt Col Komives and Dr. Candler for sharing their awesome numerical wisdom and gridding expertise. I want to thank Dr. Wagnild, Dr. Jewell and Dr. Leyva for their added support and incredible insight into the CO_2damping mechanism. I want to thank Dr. Schneider for starting the whole effort.

Olivia S. Elliott

Table of Contents

Page

Page

List of Figures

Figure Page

Figure Page

Figure Page

Figure Page

Figure Page

Figure Page

Figure Page

Figure Page

List of Tables

List of Abbreviations

List of Symbols

A, A_o	amplitude and initial amplitude of disturbance
A_s, B_s, C_s, A_4, A_5	constants
c_s	average species molecular speed
c_g, c_i, c_r	disturbance speed
c_p, c_v, c_{vs}	specific heats
D_{sr}	binary diffusion constant
E	total energy
E_v	total vibrational energy
e_{vs}	vibrational energy per unit species
$\vec{F}$, $\vec{F_I}$, $\vec{F_V}$	flux, inviscid flux and viscous flux
f_{2nd}	second mode frequency
G_q^o	Gibbs free energy
g_s	degeneracy of species s
h_s	specific enthalpy of species s
h_s^o	heat of formation of species s
K_{eq}, K_f, K_b	reaction coefficients
Le	Lewis number (dimensionless)
M_e	edge Mach number (dimensionless)
N	N factor (dimensionless)
P	pressure
Pr	Pradtl number (dimensionless)
Q_{t_v}	translational vibrational energy exchange
Q	steady state flow amplitude
q_i, q_{vi}	heat transfer

q'	disturbance amplitude
R, $\mathcal{R}$	gas constant, universal gas constant
R	$\sqrt{Re}$ (dimensionless)
r	density disturbance value
Re_∞	freestream unit Reynold's number (dimensionless)
Re_N	nose radius Reynold's number (dimensionless)
Re_{tr}, Re^*_{tr}	transition Reynold's number (dimensionless)
T, T_v	temperature, vibrational temperature
u'	contravariant velocity
V	volume
v_{si}	diffusion velocity
x, y, z	Cartesian coordinates
X_{sw}	swallowing length
α_i	spacial amplification
α_{sq}, β_{sq}	stoichiometric coefficients (dimensionless)
δ	boundary layer thickness
δ^*	displacement thickness
δ_{vs}	limiting cross section
κ	heat conductivity
μ	dynamic viscosity
ν	viscosity
ρ	density
τ	relaxation time
τ_{ij}	stress tensor
θ	temperature disturbance value
θ^*	momentum thickness

θ_{vs}	characteristics temperature
ω_i	frequency
ω_s	species production

EFFECTS OF CARBON-BASED ABLATION PRODUCTS ON
HYPERSONIC BOUNDARY LAYER STABILITY

1. Introduction

In 1904, Prandtl first observed the existence of the thin boundary layer in a fluid flow where viscous effects were confined. Since then, instability and transition of the boundary layer has been a focus of over a century of research. The boundary layer is a thin region in a fluid field where viscous forces become significant and cause a "no-slip" condition at the solid surface, requiring the relative velocity to go to zero. A boundary layer is characterized by three main types: laminar, turbulent or transitional. A laminar boundary layer is characterized by smooth flow over the vehicle with parallel streamlines and viscous diffusion is the main force acting on the flow from the body. A turbulent boundary layer is characterized by random and chaotic motion caused by vortices of various sizes. This motion causes mixing of the high-speed inviscid flow with the slower boundary layer flow creating higher gradients in the velocity and temperature profiles in the boundary layer, as well as increases the thickness of the boundary layer. The higher gradients cause increased skin friction drag and heat transfer. The transitional boundary layer is characterized by processes by which the laminar boundary layer becomes unstable, eventually leading to turbulent flow. It is this transition process that remains, despite years of study, difficult to predict and model.

Predicting the boundary layer transition is difficult due to the interdependence on numerous mechanisms that cause transition. Tollmein and Schlichting were among the first to identify the source of the instability causing transition from a laminar

to turbulent boundary layer in the subsonic regime near the body and these disturbances are now called Tollmein-Schlichting (TS) waves [18]. An extension of the TS waves are commonly called first mode disturbances in compressible flow and are the dominant instabilities in low speed flows. However, as Mach increases, this first mode is stabilized. In hypersonic flight regimes, second mode disturbances, first theorized by Mack and characterized as high frequency, acoustic-type waves, are the dominant instability and the cause of transition [19]. Mack hypothesized that for a slender body, second mode disturbances become the dominant instability mode as early as Mach 2.5, but are dependent on the edge velocity of the boundary layer [19]. The hypothetical second mode instability was later proven to exist through the experiments of Demetriades, Kendall and Stetson et. al. [20, 21, 22]. With the assumption that second mode instabilities will dominate the transition process in the hypersonic boundary layer, understanding what stabilizes or destabilizes this mode, mainly nose bluntness [23] and wall heating [24], becomes critical to accurate predictions. However, as speed increases into the hypersonic regime, the real gas effects and the interactions of the gas with the surface become increasingly important as they not only affect the fluid properties of the gas but also impact the characteristics of the boundary layer in both size and composition. At hypersonic speeds, the inclusion of the chemical and thermal state of the gas, including the gas-surface interactions for an ablating surface, is imperative for an accurate understanding of transition.

Significant wind tunnel experimentation in stability and transition characterization has occurred since the early 1960s. One recent conclusion drawn from high enthalpy testing was that as enthalpy increased in the flow, transition was delayed [7, 25, 17]. The hypothesis from this result was that real gas effects and chemical reactions within the boundary layer help stabilize it, and thus, the need to accurately model the chemical effects in the flow becomes essential to understanding and predic-

tion of transition [25]. Numerical simulations show that endothermic or exothermic reactions can dampen or amplify energy fluctuations, respectively [8]. This hypothesis has been supported from an increased transition Reynolds number in flows with higher oxygen concentrations due to the higher dissociation energy of N_2 than O_2 [8]. Hypersonic flows containing CO_2, which has a lower dissociation energy, have been shown to be even more stable due to the dissociation and the multiple internal modes in which energy can be stored [8]. The damping effect of CO_2 on disturbances in the boundary layer have been known since the 1960s [26]. Camac determined that the vibrational modes of CO_2 had nominally the same relaxation time and this was hypothesized to allow a large amount of energy to be stored in the internal vibrational modes at high enough flow velocities [26]. If the chemical composition and the types of reactions, which includes the gas-surface chemical reactions, that take place within the boundary layer affect stability it is imperative to understand and accurately model these reactions to predict transition.

Along with studying experimental results to understand the nature of the transition process, progress has been made in the modeling tools to predict it. Stability analysis is one of the preferred means of predicting transition. It is based on the analysis of the amplification of wave-like disturbances within the boundary layer and determining the distance along the vehicle when these disturbances amplify to a specific value signifying transition. There are two main types of stability analysis: Linear Stability Theory (LST) [27] and Parabolized Stability Equations (PSE) [28]. Both tools have been improved to provide highly accurate modal disturbance growth predictions. As computing power has increased, the ability to produce highly accurate numerical flow solutions as an input to the stability analysis has further increased the fidelity of the results. Specifically, the inclusion of high fidelity models of the real gas effects has provided a more realistic flow simulation and stability result [8].

Despite the difficulty in transition prediction, it remains an invaluable asset to designing a hypersonic vehicle. Determining the transition of a vehicle is important, especially at hypersonic speeds, due to the impact on the design parameters that govern the vehicle: aerodynamic forces, skin friction drag and surface heating. Specifically, the impact of transition on surface heating is critical to the design of the Thermal Protection System (TPS), a vital design component for a hypersonic vehicle. Understanding the transition process and accurately determining when a boundary layer transitions from laminar to turbulent, where surface heating rates can be ten times higher [29], allows for engineers to optimize the TPS design. This optimization includes not only determining the correct thickness of the TPS, and thus weight of the system, to prevent burn-through, but also in the choice of material used for the TPS. Since turbulent boundary layers increase surface heating, maintaining a laminar boundary layer may help maximize the efficacy of the TPS while minimizing the weight. Under-design the TPS and the vehicle will fail in flight. Over-designing the TPS wastes resources and limits the total possible payload due to the increased weight of the basic vehicle.

1.1 Research Questions, Tasks, and Scope

The main purpose of this research was to identify the effect of real gas and gas-surface interactions on the stability of the hypersonic boundary layer. Specifically, this research will examine the effects of carbon-based ablative products on the dominant second mode instability. To accomplish this goal, two areas of study were considered. First, a study was performed to determine the minimum concentration of CO_2 required in the boundary layer to have a stabilizing effect which was set as a 10 cm delay in transition location. Second, numerical flow simulations and linear stability analyses using current carbon gas-surface models were conducted and com-

pared to determine if sufficient CO_2 could be produced by ablation of carbon-based materials to affect boundary layer stability. As each gas-surface interaction model produces different concentrations of chemical species, each boundary layer was unique. Additionally, as there exists uncertainties in these gas-surface models, a parameter study on the effects of altitude, surface temperature and surface characteristics were conducted to determine the sensitivity of the results.

In order to meaningfully advance the research in this area, the scope is limited to simple geometries and focused only on how CO_2 affected the stability of the boundary layer. Simple geometries allow for an in-depth study of the thermophysics and gas dynamics within the boundary layer without introducing added complexities into the flow. A 10 degree half-angle cone with a sharp and 12.7 mm radius blunt nosetip were used for the study. A sharp cone geometry allowed for a detailed examination of the gas-surface interactions affects without geometry effects caused by a blunted nose and could be compared to wind tunnel experimental results. However, this sharp cone model is not a flight representative geometry as the heating rates on a sharp nose tip in flight would be too high. Thus, to fully comprehend the impact of CO_2 in flight regimes, a blunt cone model was also used. Due to the limited models available and the focus on the study of CO_2 effects on boundary layer stability, the surface for the study was modeled as a carbon graphite, introducing only carbon-based ablative products into the flow. Other ablative species are not known to have similar damping effects and will not be examined in this study.

Specific research questions relating to the study objectives are:

1. What is the sensitivity of a hypersonic boundary layer to changes in the species concentrations of carbon-based ablative species, specifically CO_2, at both wind tunnel and flight representative freestream parameters?

2. What are the variations in the current gas-surface chemical models and what effects do these variations have on the CO_2 concentrations and the stability of a hypersonic boundary layer over a sharp and blunt cone?

3. What is the sensitivity of the current gas-surface chemical models to changes in the freestream flow parameters, surface temperature and site density and what are the stability effects?

The research used US3D, a parallel, implicit CFD solver developed at the University of Minnesota, to simulate the flow over a simple 10 degree half-angle cone with a sharp nose and a 12.7 mm nose radius [30]. A dedicated study to determine the total concentration of CO_2 needed in the boundary layer to affect the stability characteristics was conducted. The input freestream parameters for the flow solver were used to set specific CO_2 concentration in the boundary layer. After determination of the CO_2 concentration requirements, a study was conducted examining the addition of CO_2 into the boundary layer through the multiple air-carbon gas-surface interaction models. The US3D solver included a user-defined module to allow for the manipulation of ablation model and the gas-surface chemistry boundary conditions. Six current air-carbon gas-surface ablation models were used in determining the boundary conditions in the simulations: Park [31], Park76 [32], Zhluktov and Abe [14], modified Zhluktov and Abe [15], Zhluktov and Abe with nitridation [15] and the MURI carbon oxidation model [16]. A set of parameter studies were also conducted to determine the interdependence of the flow conditions, surface characteristics and the chemical models on the stability of the boundary layer. Stability and Transition Analysis for Hypersonic Boundary Layers (STABL3D), a linear stability analysis code developed to utilize the results of a US3D flow simulation to determine transition and stability parameters, was used to determine the stability characteristics of the boundary layer [33].

Several assumptions and limitations needed to be made to successfully bound the research tasks outlined above.

1. The changes in the shape of the body, specifically the nose, due to ablation are considered to be negligible. This assumption was made based on the small total shape change of past flight vehicles. For the sharp cone, it was necessary to maintain a sharp nose to avoid geometry effects. For the blunted nose cone, a slight increase in the nose bluntness was assumed to be small enough when compared to the original nose radius so as not to have a significant impact.

2. Surface roughness was not included in this study. Though ablation is known to cause roughening of the surface, roughness has been shown to have a transient growth, or even a bypass transition, effect which would not be modeled by the linear stability theory. These effects are typically non-linear in nature and are not captured in the traditional modal analysis of LST. Excluding surface roughness allows the focus of the study to remain on the real gas effects only.

3. The surface was modeled only as graphite. While many TPS materials and designs have become more advanced, others remain carbon based. Significant research has been done on the sublimation and oxidation of graphite under hypersonic flow conditions, and as such the surface properties are well known and used. Multiple carbon gas-surface interaction models have been developed from experimental data and are well characterized. CO_2 is added to the flow only by the ablation of the carbon surface. This limitation allowed for the in-depth study of the effects of CO_2 without unduly increasing the computational requirement with other ablative species.

4. Linear stability analysis is used in the stability study despite the simplifying assumption of parallel, or locally parallel flow and the linearization of the equa-

tions of motion of the flow. This assumption was valid as the damping effect of CO_2 affects only the second mode instabilities of a hypersonic boundary layer. The second mode instability is a linear instability, and therefore these effects could be captured with an LST analysis. In order to capture non-linear effects, a non-linear PSE or a Direct Numerical Simulation (DNS) would need to be conducted at great computational cost but without a direct focus on research questions.

5. No freestream disturbances were included in the flow simulations. This assumption is valid at all flight representative freestream conditions due to it being a low noise environment as flight conditions contain no continuous freestream disturbances.

6. All flow simulations are assumed to be at zero angle of attack. This assumption also simplifies the flow and allows for lower computational requirements as the flow can be modeled axi-symmetrically.

Chapter 2 provides an overview of boundary layer instability concepts including receptivity, transition mechanisms, transition characteristics, nose bluntness effects and CO_2 damping effects on stability. Chapters 3 reviews the mathematical models and numerical methods used in the study. Chapter 4 reviews the methodology used for the numerical simulation and stability analysis. Chapter 5 reviews the results from the CO_2 concentration study. Chapter 6 reviews the results from the gas-surface interaction study and the parameter study. Chapter 7 provides conclusions and proposed future work. A separate appendix will be provided comparing flight test transition data with the stability analysis results of the simulations using each of the aforementioned models.

2. Boundary Layer Instability

2.1 Disturbances and Instability

2.1.1 Receptivity and Transition Mechanisms.

Receptivity of the boundary layer is defined as the process by which disturbances generate instability waves in the boundary layer and the instability initial conditions are created. Receptivity is influenced by such flow characteristics as ablation, surface roughness, nose bluntness, and Mach number [34]. The growth or recession of the disturbance in the boundary layer is determined by how receptive the boundary layer is to the specific disturbance characteristics. If it is receptive, the initial disturbance will be amplified by one or more of the instabilities, which can also interact with each other [35]. Numerous instabilities exist for a hypersonic boundary layer and the conditions at the surface, geometry and the boundary layer edge flow determines which is, or are, the dominant instability mechanism [36]. Fedorov [37] outlined the four main paths to transition: traditional modal, modal transient growth, non-modal transient growth and large amplitude forcing. Traditional modal growth mechanisms are the first and second modes, crossflow and Gortler instabilities which all occur in low-disturbance environments. Modal transient growth disturbances provide a higher initial amplitude to the eigenmode path but remains linear in nature in the process to transition, such as tunnel noise or large surface roughness [37]. Non-modal transient growth mechanisms are generally the supposition of nonorthogonal, highly oblique waves onto the modal system and have a nonlinear effect. Both the transient growth mechanisms bypass the traditional modal growth concept and, along with the large amplitude forcing functions on a nonlinear nature, are referred to as bypass transition and exists outside the linear growth regime [37].

First mode instability is a Tollmien-Schlichting type wave with maximum amplification occurring when the wave fronts are oblique to the streamwise direction[19]. First mode instabilities tend to dominate the flow at only at sub- or low supersonic speeds, so are not usually the dominant instability in hypersonic boundary layers. The second mode instability are trapped, acoustic-type waves which are the most amplified when the wave fronts are normal to the streamwise direction [19]. These are the dominant instabilities in hypersonic flows, especially with cold walls, and usually require an edge Mach number of 2.5 or above to be the dominant transition mechanism [19]. Due to the relative supersonic mean flow, relative to the disturbance phase velocity, the boundary layer acts as an acoustic wave-guide, where the disturbances are reflected between the surface and the relative sonic line [37]. Second mode tends to dominate the stability of a flow as its growth rates are higher than first mode [37]. Crossflow instabilities are the result of a pressure gradients outside the boundary layer, which causes curved streamlines and the creation of a secondary flow in the boundary layer that is perpendicular to the inviscid streamline [34]. The crossflow instability are co-rotating vorticies in the flow which exists in three-dimensional boundary layers and typically occur on swept geometries or cones at angles of attack. These instabilities are not present over axi-symmetric geometries and are not considered to be a likely transition mechanism for this study. Gortler instabilities form with concave walls or with the existence of concave streamline curvature and are characterized by the presence of counter-rotating vorticies [35]. Again, these instabilities are considered to be absent in this study, based on the geometry and flow direction used.

There are also non-linear transition mechanisms that have been identified: secondary instabilities, non-modal instabilities and bypass instabilities. These instabilities are not modeled or predicted by Linear Stability Theory (LST) or Parabolized

Stability Equations (PSE), and other methods of prediction, such as Direct Numerical Simulation or Input/Output Analysis are needed to visualize and predict these instabilities [38]. Secondary instabilities arise after the linear growth period of the modal instabilities where non-linear interactions between instabilities can no longer be neglected [39]. When the linear instabilities, often referred to as primary instabilities, begin to breakdown and/or experience interactions with other primary instabilities, the result is a non-linear region of the instabilities, which often occurs right before the boundary layer transition [39]. There also exist non-modal instabilities that affect the boundary layer flow. These first became important to help explain the blunt body transition reversal phenomena seen in Stetson's windtunnel experiments [23, 4, 40]. This work is explained in detail in Section 2.2. Also of interest are entropy layer instabilities as a result of nose bluntness. These instabilities are discussed in more detail in Section 2.2.1.

2.1.1.1 Second Mode Instabilities.

The second mode instability is the focus of the research effort due to the fact that is often the dominant instability in axi-symmetric hypersonic flow, and it is the instability most affected by the vibrational damping of CO_2. The increased freestream Mach number at hypersonic speeds translated directly to increased velocity in the boundary layer. It was discovered by Mack [41] that in hypersonic boundary layers there exists flow where the relative Mach number (the difference between the mean velocity and the disturbance phase velocity) is at or greater than 1. When the flow reaches these values, Mack showed that the disturbance equations become hyperbolic, rather than parabolic, in nature and thus instead of a single solution at each frequency, there exist a family of solutions, which he named "modes". Of these modes, Mack showed that the second mode is the dominant mode for instability [42]. The existence of sec-

ond mode instabilities has been supported by wind tunnel experiments conducted by Kendall(1974), Demetriades(1978) and Stetson and Kimmel(1982) showing stability characteristics consistent with second mode disturbances [21, 20, 22].

Second mode disturbances are often classified as high-frequency, acoustical type disturbance which grow faster than the Tollmien-Schlichting (first mode) disturbances and dominate the hypersonic boundary layer. The higher frequency nature of these instabilities cause the hypersonic boundary layer becomes "tuned" to only those frequencies which amplify these instabilities. It was found that a wavelength of approximately twice the boundary layer thickness are amplified the most, especially when aligned with the mean flow [23]. Analyses using LST have shown that second mode disturbances are well-predicted on sharp cones. Nose bluntness, however, tends to stabilize second mode instabilities when the entropy layer thickness exceeds the boundary layer thickness [43]. However, once the entropy layer is entrained into the boundary layer, the stability of the flow become more difficult to predict. Real gas effects destabilizes second mode disturbances [44] while chemical non-equilibrium has a slight stabilizing effect [45].

2.1.2 Transition.

The purpose of understanding the causes of instability in a boundary layer is mainly to determine how to better predict the transition from laminar to turbulent flow, with respect to location and mean flow conditions. Predicting the initial breakdown of laminar flow through the amplification of these instabilities is only the start of the transition process as the flow then passes through a series of instabilities. Herbert [39] stated that the evolution of transition happens in three instabilities: primary instability, as seen with the growth of traditional modal instabilities, secondary instabilities, with the growth of three-dimensional spanwise disturbances commonly know

as lambda-type vorticies, and tertiary instability, where the flow exhibits turbulent spots. The secondary and tertiary instabilities are decidedly non-linear in nature. While LST analysis does not consider the non-linear effects of the secondary and tertiary instabilities, it is still able to predict the onset of transition which is considered to be dominated by linear processes and occurs before secondary instabilities start to dominate the flow [39].

White [3] provides a pictorially representation of transition in a boundary layer in Figure 2.1

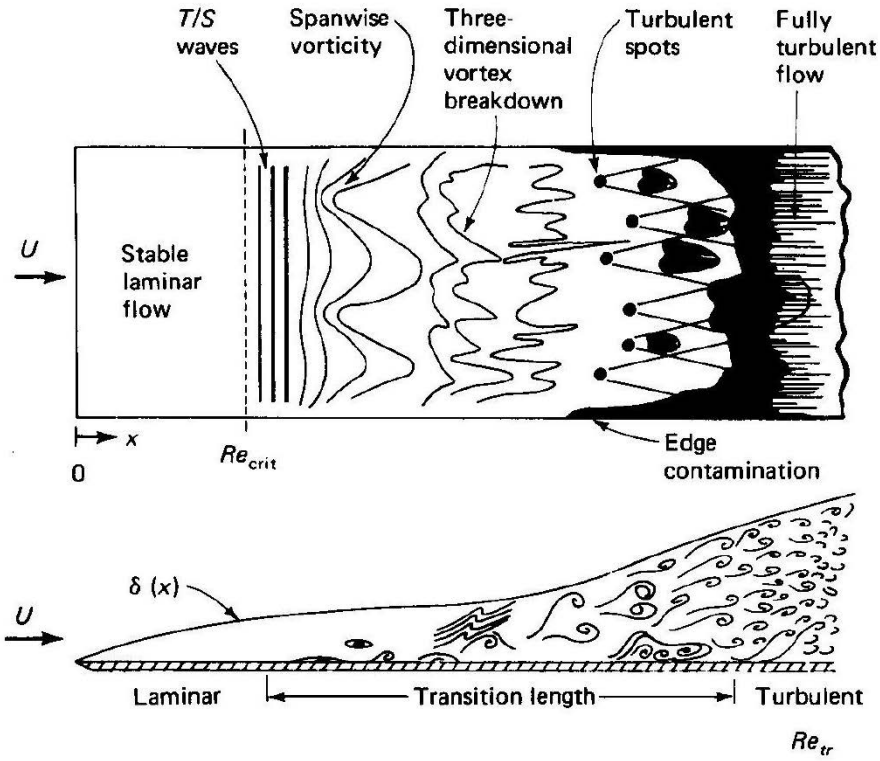

Figure 2.1. Paths to Turbulence [3] (with permission)

Factors affecting the transition include freestream and edge of the boundary layer Mach numbers, nose bluntness, angle of attack, external or freestream disturbances, wall temperature, surface roughness, pressure gradient, non-equilibrium flow and mass transfer [23]. Morkovin showed that for hypersonic vehicles the main mechanisms for

transition are pressure gradient, cross-flow disturbances and ablation, which causes mass injection into the boundary layer at and near the surface [46].

2.1.3 Transition Prediction: e^N Method.

Understanding the stability theory and the stability of a flow, however, does not provide a determination of the transition point. Semi-empirical methods to predict transition were first developed by Smith and Gamberoni [47] and Van Ingen [48] and later updated by Jaffe, Okamura and Smith in 1970 [49]. Using wind tunnel data at that time and applying an LST analysis, both Smith and Van Ingen independently developed the e^9 method, in which the ratio of the disturbance amplitude at a initial time or x-location and a place later in the flow can be calculated from

$$\frac{A}{A_o} = exp\left(\int_{t_o}^{t} \omega_i dt\right) \tag{2.1}$$

$$\frac{A}{A_o} = exp\left(\int_{x_o}^{x} -\alpha_i dx\right) \tag{2.2}$$

where the quantity $\int_{t_o}^{t} \omega_i dt$ or $\int_{x_o}^{x} -\alpha_i dx$ is known as the amplification factor, σ^*. From their work, an amplification factor of 7.8 indicated the start of transition, while an amplification factor of 10 indicated the end of transition [48].

This method was later renamed e^N. Instead of using an amplification ratio of 9 to signify transition, an N-factor was introduced as

$$N = \ln\left(\frac{A}{A_o}\right) = \int_{x_o}^{x} -\alpha_i dx \tag{2.3}$$

where N is the amplification factor and α_i is the amplification in the imaginary direction. Calculating N facotrs as a function of the x for a range of frequencies provides a set of N-curves. The envelope of these curves gives the maximum amplification

factor which occurs at any x location [50]. While widely accepted, this method is not useful in flows dominated by non-linear instabilities, such as cross-flow, and requires knowledge of the neutral stability point amplitude, A_o [48]. This method of prediction requires that a mean flow be known at a large number of streamwise locations and, at each of these locations, an LST analysis performed for all the frequencies for the normal modes, both of which can be computationally expensive to do [50]. Also, the results of this method are empirical in nature and the value of N which represents transition comes directly from experimentation[47]. In wind tunnels, transition is noted to occur by an N factor of 10 (given quiet tunnel operations) while flight N factors at transition range from 8.5 to 14 [51]. Despite these weaknesses, this method remains the most widely used for predicting transition location.

2.2 Nosetip Bluntness Effects

2.2.1 Entropy Layer.

Entropy is the thermodynamic quantity which represents the unavailability of energy for conversion to mechanical work and is often described as the degree of randomness in a system or the direction which a thermodynamic process is allowed to take. The second law of thermodynamics states that the direction a process takes will always increase, or maintain constant, the total entropy. Generation of entropy is due to irreversible processes, such as dissipative phenomena of viscosity, thermal conductivity and mass diffusion[52]. A shock is an irreversible process which increases the entropy of the system, equivalent to the total pressure loss across the shock. This increase is directly related to the strength of the shock; a normal shock is stronger than an oblique shock thus a higher increase in entropy. A blunt body traveling at hypersonic speeds will create a curved shock, known as a bow shock. At the nose, a streamline travels through the nearly normal shock at the center-line and

has a large increase in entropy. Each subsequent streamline that passes through the bow shock will have a smaller increase in entropy, creating an entropy gradient along the streamlines called the entropy layer. Figure 2.2 shows a representation of the entropy layer. For hypersonic regimes, the entropy layer is initially larger than the boundary layer, however, at some distance down the body, depending on nose radii and Reynolds number, the boundary layer entrains, or "swallows", the entropy layer. The entropy layer has been shown to have a stabilizing effect on the second mode instabilities through experimentation, but there has been limited work done on determining the mechanism of that stabilization. Recent work by Kuehl et al. examined the theoretical possibility that in an entropy layer, the density gradients vary due to the entropy variations which limit the second mode disturbances ability to amplify and are in the process of matching theory to experimental results [53]. Despite not understanding the mechanisms in the entropy layer which stabilized the boundary layer, experimentation by Stetson showed that before a critical nose bluntness, based on the ratio of the nose radius to the base radius, the entropy layer stabilized the boundary layer until it was "swallowed" and then the boundary layer rapidly transitioned to turbulence which was attributed to entropy-layer instabilities [6].

The effect of instabilities in the entropy layer on the stability of the boundary layer is not well understood and remains an area of active study. The entropy layer is a region of strong vorticity due to the high gradients based on Crocco's Theorem. This vorticity causes entropy-layer instabilities [54]. Entropy layer instabilities are an inviscid phenomenon and the most amplified waves are not necessarily oblique waves [6]. Stetson et al. measured entropy layer instabilities in blunted cone experiments and found that these disturbances grew slowly outside the boundary layer, then quickly amplified inside the boundary layer to cause transition [6].

2.2.2 Swallowing Distance.

In flight vehicles, nose tip bluntness, both in vehicle design and as a result of ablation, further complicates the physics of the boundary layer and transition prediction. The simplest approach to calculate the boundary layer edge parameters is to neglect the coupling of the inviscid flow with the boundary layer region. While this method is acceptable for sharp cone designs, in the early 1950's work by Ferri and Libby [55] showed that the entropy gradients induced by the bow shock curvature around a blunted nose produced a coupling effect between these two regions. The external streamline vorticity and continuously varying entropy aft of the nose region affects the stability of the flow in the boundary layer. To account for the variable boundary layer entropy, the concept of a swallowing distance was introduced by Zakkay and Krause [56] and later quantified by Rotta [5]. Rotta developed a method to quantify the effects of shock curvature on the flow and identified a location where the streamlines that crossed the curved portion of the shock become entrained in the lower entropy viscous boundary layer, which he called the "swallowing distance" [5]. Stetson later described the swallowing distance as the location on frustum where the local Mach number and the flow properties at the edge of the boundary layer were nearly (0.96 to 0.98) the same as would be found on a sharp cone [4]. Figure 2.2 shows the geometry of the blunt nose and the resulting curved shock and entropy layer. The overall result of Rotta's computations for the swallowing distance was to show that the swallowing distance was proportional to $Re_\infty/ft^{\frac{1}{3}}$ and $R_N^{\frac{4}{3}}$. These results were simplified in a graph shown in Figure 2.3. This concept of swallowing distance has been used extensively in analyzing wind tunnel data on the effect of nose bluntness on stability.

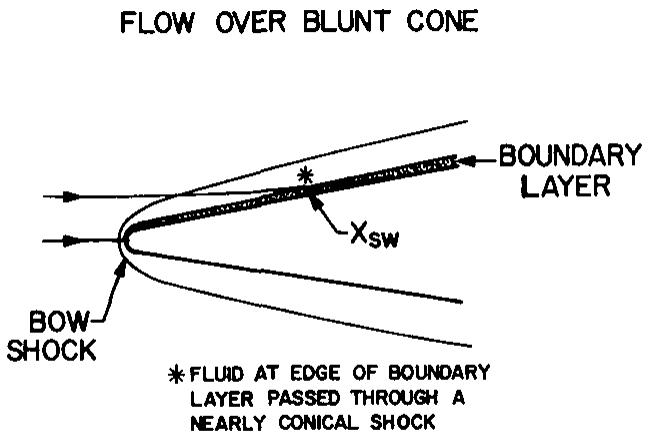

Figure 2.2. Entropy Layer over a Blunt Cone (taken from [4])

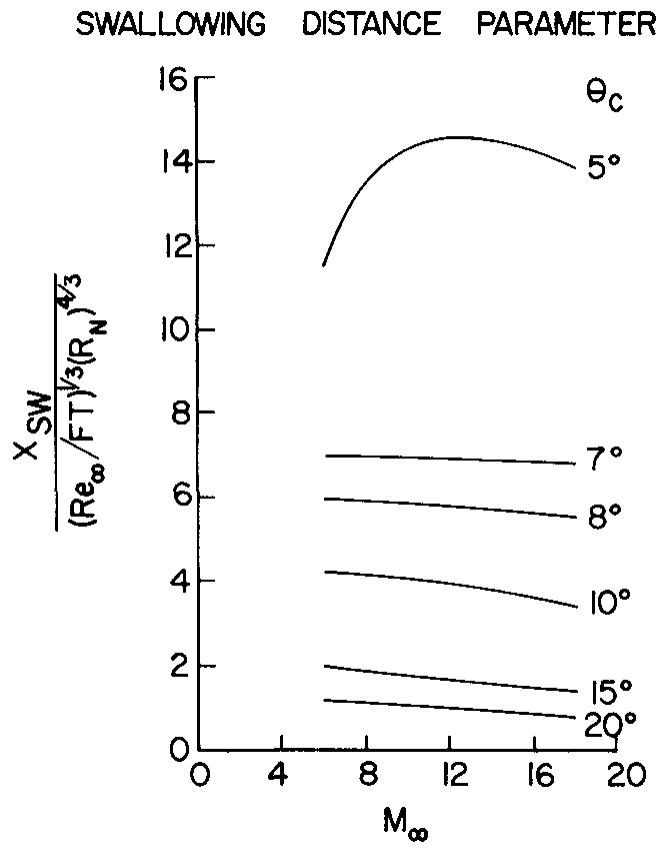

Figure 2.3. Rotta's Swallowing Distance (taken from [5])

2.2.3 Bluntness Effects on Stability.

Wind tunnel experiments have been conducted since the 1960's looking at the effect of nose bluntness on boundary layer transition [57, 58, 40, 4, 59]. Despite the number of different experiments, the work done by Stetson is considered the most comprehensive. Early work by Stetson and Rushton in 1967 [40], conducted on an 8 degree half-angle cone at Mach 5.5, showed that the transition on a blunt cone was mainly affected by the reduction in the local Reynolds number, calculated using the boundary layer edge conditions, as a result of the blunt nose. This decrease resulted in a rearward movement of the transition location compared to a sharp nose until the nose radius reached a critical bluntness. As the nose bluntness increased past this critical bluntness, a reversal was seen and the transition location moved forward on the cone indicating an optimum nose radius for a given flow condition. Stetson and Rushton also introduced swallowing distance as a parameter to examine the effects of nose bluntness on transition, thus allowing cones with different half-angle and nose radii, as well as different freestream flow characteristics to be compared [6].

Between 1978 and 1982, Stetson conducted 196 sharp and blunt cone experiments run in the Air Force Research Lab's (AFRL) Mach 6 wind tunnel and Arnold Engineering Development Center (AEDC) Mach 9 wind tunnel. The results of his sharp cone experiments verified Mack's theory that the hypersonic boundary layer was dominated by the second mode disturbances and were very selective in the frequencies that were amplified [4]. These frequencies were directly related to the boundary layer thickness as predicted. They also provided Stetson with a basis for analysis for the effects of nose bluntness.

For his blunt cone experiments, Stetson used the same model and facilities, but made the nose tip interchangeable to allow for varying nose bluntness. The conclusion to most of his bluntness analysis was that the blunting effects competed for the

dominant role in transition and large changes in transition Reynolds number were believed to be dependent on what transition mechanism was dominant. Stetson identified three regions of interest when looking at the effects of bluntness. In the region where the transition location was approximately the same as the swallowing distance, the nosetip had a stabilizing effect on the boundary layer and the transition Reynolds number was greater than on a sharp cone [4]. Near the front of the cone, when $\frac{X_T}{X_{SW}} = 0.03$, the flow was dominated by the nosetip flow and the surface conditions and lower transition Reynolds number were found [6]. However, the location where $\frac{X_T}{X_{SW}} = 0.1$ showed a transition Reynolds number less than a sharp cone but Stetson could not identify the dominant instability producing transition [4]. He was able to show, however, that the rearward displacement of transition was very sensitive to freestream Mach number as well as the nose tip bluntness [6]. This effect is shown in Figure 2.4. Overall, for the different bluntness tested, the maximum transition Reynolds number was shown to be where transition occurred right before the entropy layer was swallowed. Figure 2.5 shows Stetson's results.

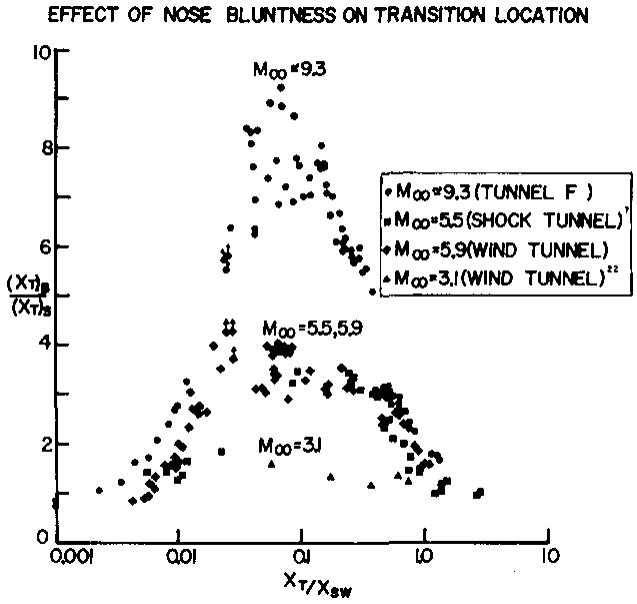

Figure 2.4. Bluntness effects on transition location (taken from [6])

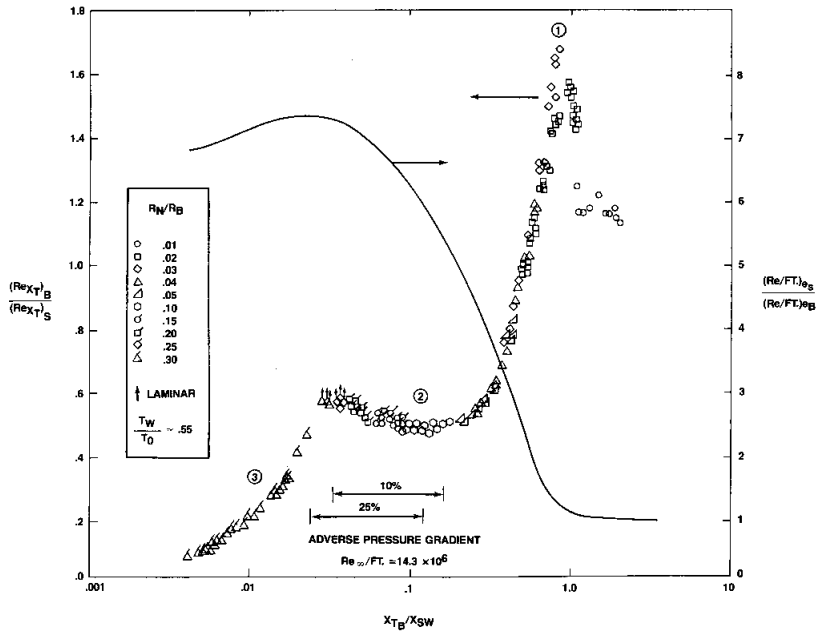

Figure 2.5. Bluntness effects on transition Reynolds number (taken from [6])

2.3 CO_2 Damping

2.3.1 Carbon Ablative Surfaces.

Significant characterization of carbon graphite oxidation and sublimation was done in the late 1960s. Blyholder and Eyring noted that many of the oxidation characteristics were based on the purity, porosity and defects in the material itself and noted that as graphite ablates significant variations in the surface area or active sites were noted [60]. Through oxidation experiments with graphite at high temperatures (though overall surface temperatures were limited to 1300 F), Blyholder determined a general number of active carbon sites in graphite to be $3.5x10^{15}\frac{atom}{cm^2}$ or $5.81x10^{-8}\frac{kmol}{m^2}$ and that the sites were mobile in nature, where the adsorbed O atom could move sites along the surface [60].

Further work done by Scala and Gilbert examined the sublimation reactions of graphite where the total number of active sites were found to be a function of the surface temperature and ambient pressure [61]. However, these conclusions were also dependent on ratio of sublimation to oxidation and it was noted that as the surface temperature increased, sublimation became the dominant reaction thus reducing the amount of oxygen adsorbed more so than the number of active sites [61]. Also, Scala's work showed nominal concentrations of C_4 and C_5 in the sublimation flow thus only C, C_2 and C_3 needed to be included for accurate sublimation results. In similar sublimation experiments, Metzger et al. showed that the mass loss rate and diffusion controlled oxidation was independent of the crystalline structure of the material and dependent on surface temperature and pressure [62]. Lundell et al. later determined through high temperature experiments, that as the surface temperature of graphite approaches 4000 K, the vaporization temperature of graphite, mass loss reactions become independent of pressure and varies only with temperature making the sublimation rates different as the material approaches these high temperatures

[63]. This change in rates typically leads to over prediction of mass loss at hypersonic speeds. While these results are valid for graphite, carbon fiber materials are not able to use the same assumptions and work is currently being conducted to determine how the carbon fiber structure affects the overall ablation rates [64, 65]. Modern carbon gas-surface ablation models still use the active site number and limit the sublimation reaction to C, C_2 and C_3.

2.3.2 CO_2 Properties.

Molecular vibrational relaxation is a non-equilibrium process that depends on a specific relaxation time [66]. The theory of relaxation processes absorbing energy from acoustic waves was detailed by Vincenti and Kruger [67] in 1965. A general understanding of the process is for a gas in non-equilibrium, and the characteristic acoustic time is close to the relaxation time of the gas, then the changes in density due to the pressure differential of the disturbance lag that of the gas pressure as a number of collisions are required for the gas to achieve the new value. If the acoustic wave has a frequency that is higher than that of the optimum absorption frequency, then the energy does not have time to transfer to the internal modes and the gas appears frozen. If the acoustic wave frequency is lower than the absorption, then the gas equilibrates as the wave travels through the gas. The damping effect is decreased as the vibrational mode is in equilibrium.

While molecules can absorb energy by the vibrational relaxation process, the specific vibrational characteristics of the CO_2 molecule provide specific damping capabilities in hypersonic flows. CO_2 is a linear, tri-atomic molecule that possesses a circular axial symmetry around an axis passing through the three atoms[68]. CO_2 has three vibrational modes: a double degenerate transverse bending mode (ν_2) with a characteristic vibrational temperature of $\theta_2 = 960.1K$, a symmetric longitudinal

stretching mode (ν_1) with a $\theta_1 = 1992.5K$ and an asymmetric longitudinal stretching mode (ν_3) with $\theta_3 = 3380.2K$. The uniqueness of this molecule comes from the fact that the vibrational modes all have approximately the same relaxation time as discovered by Camac in 1966 [26]. Camac, testing with shock tubes, discovered that at higher freestream velocities, above 6.5 $\frac{mm}{\mu sec}$, the internal vibrational modes of the molecule were completely coupled. Specifically for his tests with CO_2, he saw that all four vibrational modes could be excited simultaneously and were completely coupled from 2000-6000K with approximately the same relaxation time [26]. From his experimentation, he determined the relaxation time for all four modes to be

$$ln\left(A_4 \tau_{CO_2} p\right) = A_5 T^{-\frac{1}{3}} \tag{2.4}$$

where $A_4 = 4.8466x10^2 \frac{Pa}{s}$ and $A_5 = 36.5 \deg K^{\frac{1}{3}}$.

This coupling of the vibrational modes of the CO_2 molecule comes from the VV (vibrational-vibrational) relaxation between the modes which is responsible for the vibrational energy redistribution within each isolated mode [69]. Polyatomic molecules can have two or more vibrational levels corresponding to different vibrational modes that have nearly the same activation energy and same symmetry type which causes an "accidental" degeneracy known as Fermi resonance [70]. For CO_2, this mutual interaction between the vibrational modes ν_1 and $2\nu_2$ and ν_3 and $3\nu_2$ results in energy transfer between them and is essentially non-linear in nature [71, 72]. However, these intra-mode VV energy exchanges are almost resonant and very rapid when compared to other energy transitions (such as vibrational-translational exchanges) and thus do not affect the overall fluid dynamic variables of the flow [69].

2.3.3 High Enthalpy Tunnel Testing.

The damping effect from the presence of CO_2 in the boundary layer is well documented by numerous wind tunnel experiments in the California Institute of Technology's Graduate Aeronautical Laboratory at the California Institute of Technology (GALCIT) piston-free T5 wind tunnel. High enthalpy wind tunnel testing was conducted by Germain and Hornung [25] and Adam and Hornung [7] in which a sharp, 5 degree half angle cone was used. These experiments were the first to look at transition at high Mach numbers but not in a cold flow facility. Since cold flow facilities achieve high Mach numbers by lowering the speed of sound, the kinetic energy remains too low to look at kinetic effects on the molecules in the flow. Using freestream gases of air, N_2 and CO_2, this testing showed that as enthalpy increased so did transition Reynolds number and it was noted that all the testing done with CO_2 yielded a slightly higher Reynolds number than the other gases [25]. Adam noted that while there seemed to be little correlation with enthalpy when comparing Re_{tr}, when compared to a reference temperature (Equation 2.6), the transition Reynolds number for flows with CO_2 showed a significant increase[7]. Figures 2.6 and 2.7 shows these results. It was determined from these studies that CO_2 showed the greatest absorption when the freestream enthalpy was between 3 and 11 $\frac{MJ}{kg}$. Above this value, the energy of the flow as high enough to cause most of the CO_2 to dissociate.

$$Re^*_{tr} = \frac{\rho^* u_e x_{tr}}{\mu^*} \tag{2.5}$$

$$\frac{T^*}{T_e} = 0.5 + 0.039 M_e^2 + 0.5 \frac{T_w}{T_e} \tag{2.6}$$

These results were studied computationally by Johnson who focused his examination on the effects of chemical reactions on the stability of the boundary layer that

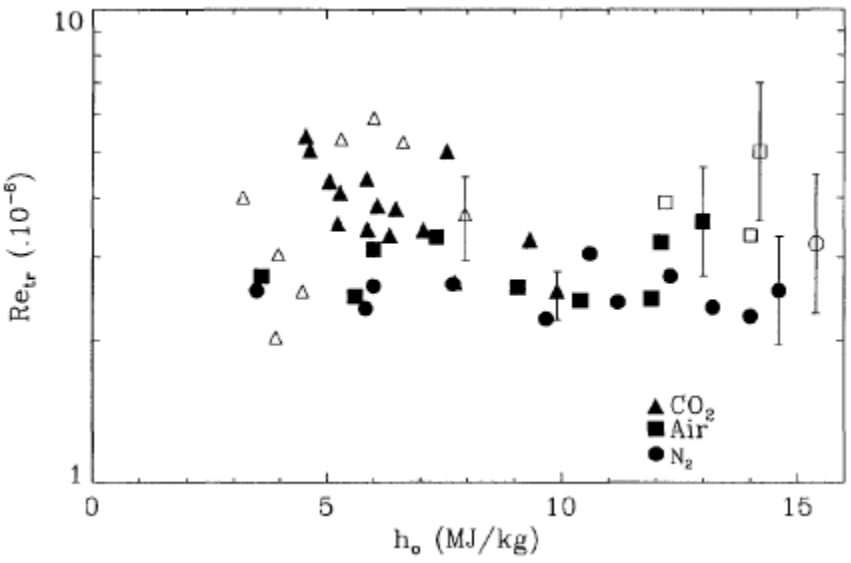

Figure 2.6. Transition Reynolds number versus stagnation enthalpy [7] (with permission)

were seen at these high enthalpy flows [8]. While his results showed a similar effect of higher enthalpy increasing transition Reynolds number, he related these results to the effects of the chemical reactions on amplification of disturbances at high frequencies. Johnson conducted stability analyses on the flow twice, once with chemical effects enabled and once with the chemical reactions disabled. Figure 2.8 highlights the difference in the amplification of disturbances with a reacting and non-reacting gas [8]. Johnson concluded that due to the lower dissociation energies (an endothermic and therefore stabilizing reaction) and the larger number of vibrational modes of CO_2 which transitioned the kinetic energy from the disturbance into internal vibrational energy was the cause of the transition delay [8]. As was stated above, for CO_2, if the flow has a high enough enthalpy, or high enough temperatures to activate the vibrational modes, then all four modes can be used to absorb energy at the same frequency as the disturbance frequency.

Fujii and Hornung continued this research focusing on correlating CO_2 absorption frequencies to the second mode instability frequencies [9]. Using the absorption

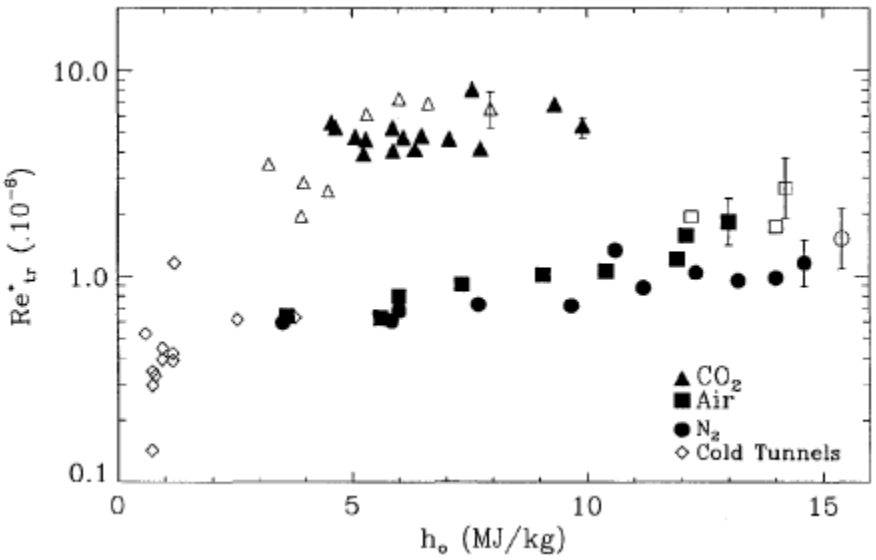

Figure 2.7. Transition Reynolds number at reference temperature versus stagnation enthalpy [7] (with permission)

estimation procedures found in Vincenti and Kruger [67], Fujii showed that the frequencies at which CO_2 had the maximum absorption rate could be estimated. Using the frequency estimation procedure, Fujii calculated the absorption rates for CO_2 from 1000-6000K (Figure 2.9, where the maximum absorption peaks between 500 kHz to 10 MHz [9]). Combining this with the estimate of the most amplified second mode frequency, estimated by Equation 2.7 [22], Fujii was able to determine when the frequencies of maximum CO_2 absorption coincided with the second mode instability frequencies.

$$f_{2nd} = A\frac{u_e}{2\delta} \tag{2.7}$$

where u_e is the boundary layer edge velocity, δ is the boundary layer thickness, and A has been estimate to be between 0.7 [10] to 1 [9].

Fujii and Hornung were able to show that the absorption rates for CO_2 were similar to the amplification rates for the instabilities from 1-10 MHz for the high enthalpy flows from 3 to 15 $\frac{MJ}{kg}$. This range of frequencies is coincident with the second

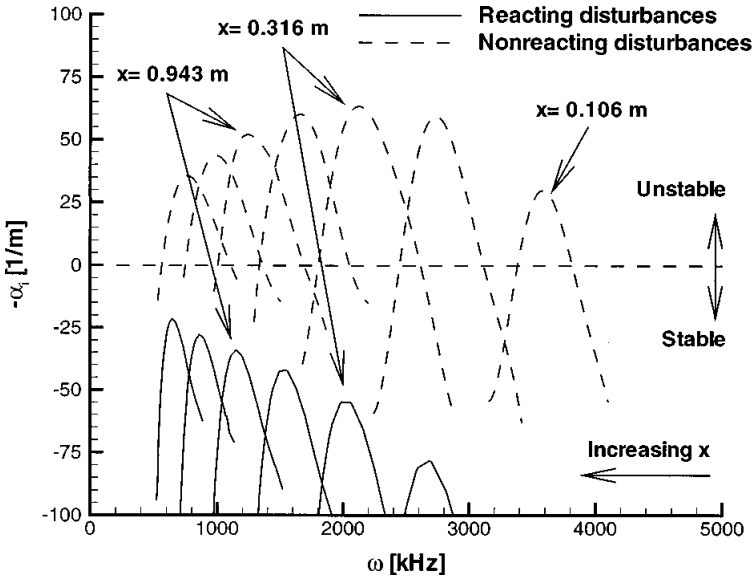

Figure 2.8. Amplification rate versus frequency in flows with CO_2 [8] (with permission)

mode disturbances in hypersonic boundary layers. Figures 2.10 and 2.11 shows the numerical stability results for air and CO_2[9]. From these results, it is clearly seen that in air, the instability frequencies are much higher than where air is able to absorb energy. However, for the flow with CO_2, the instability frequencies coincide with the absorption frequencies.

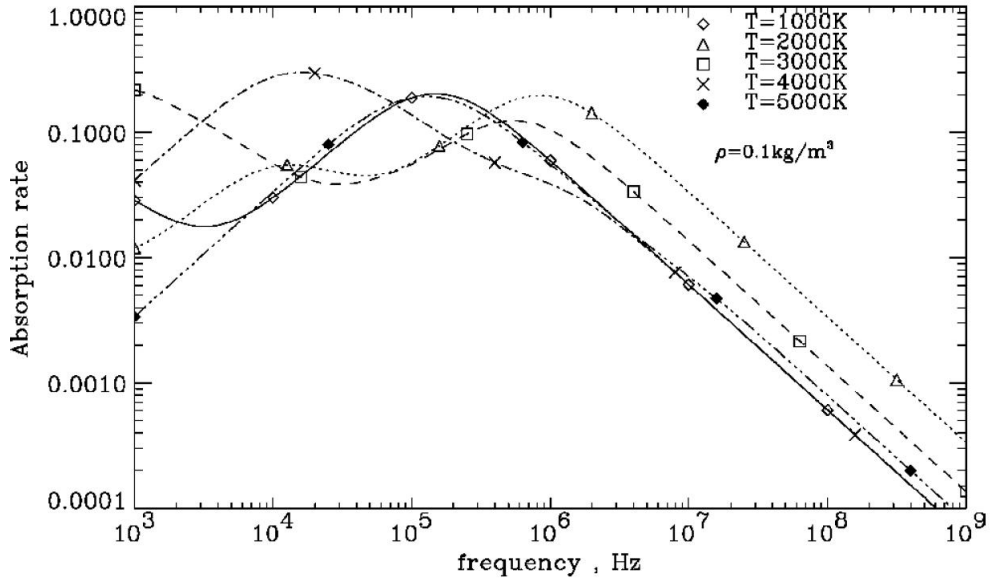

Figure 2.9. Absorption rates at different temperatures [9] (with permission)

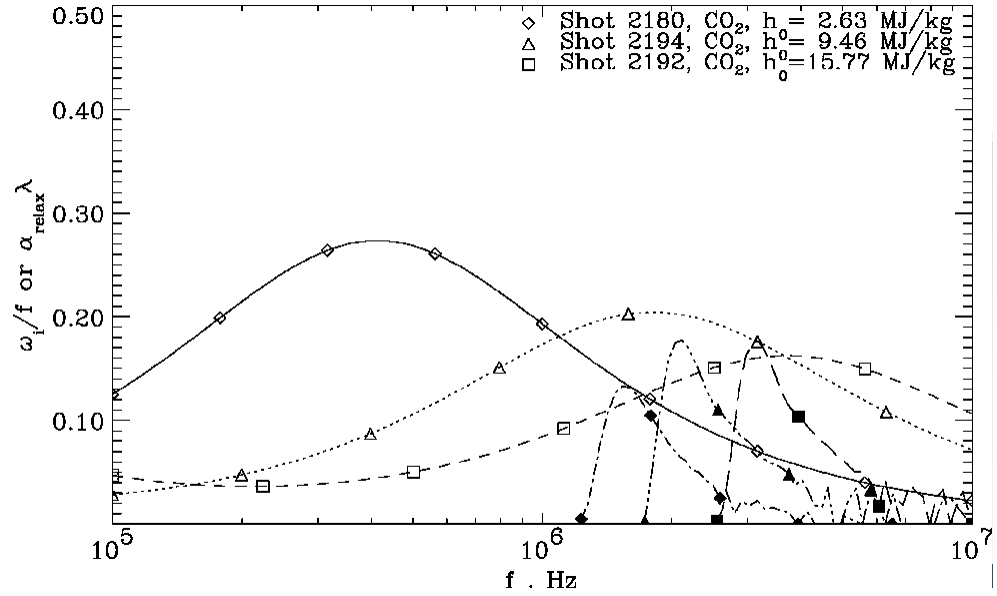

Figure 2.10. Disturbance frequencies compared to absorption rate of CO_2 [9] (with permission)

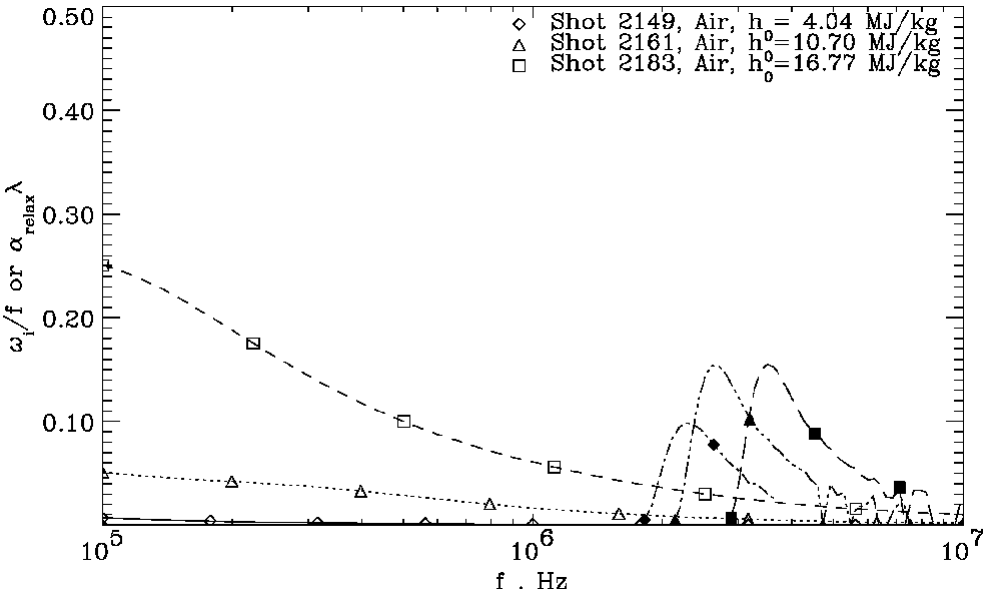

Figure 2.11. Disturbance frequencies compared to absorption rate of air [9] (with permission)

These results led directly to the research done by Leyva et al [73] to try to determine if injection of CO_2 into the boundary layer would provide boundary layer stabilization. Leyva et al. used the same geometry as the previous T5 experiments but injected CO_2 into the boundary layer via a porous section near the tip of the cone. Their research showed that for a specific range of mass injection flow rates and flow conditions, increased transition Reynolds number could be achieved, however, the disturbance of the injection of the gas into the boundary layer for most flow conditions caused transition of the boundary layer at the injection site [73]. Examining the experimental results in numerical simulations, Wagnild showed the same results that were experimentally determined by Leyva [51] for a wider variation of flow conditions.

Jewell et al., working as part of the same research effort, used the same 5 degree half-angle cone geometry examining the variation of enthalpy and concentration of CO_2 in the freestream [10]. Jewell showed results comparing the effect of reacting versus non-reacting gas flow but also the impact of freestream total enthalpy on flows with CO_2 present. Figure 2.12 and Figure 2.13 show the results of changing the reacting nature of the gas as well as the freestream versus CO_2 mass fraction. Figure 2.12 shows the numerical result of a constant flow enthalpy while varying the CO_2 concentration. The result shows an asymptotically decreasing effect as CO_2 concentrations decrease until the reacting flow shows similar results to the frozen flow. Figure 2.13 compares results of varying enthalpy with the changing concentrations of CO_2. At high enthalpy conditions, a large effect is seen in the increased transition location. However, at lower enthalpies, the effect is greatly decreased. These results were used to determine the range of enthalpy values used in the current CO_2 concentration study.

These experiments and numerical simulation all used CO_2 in the freestream as the delineating condition. However, these are not conditions that would be seen in flight

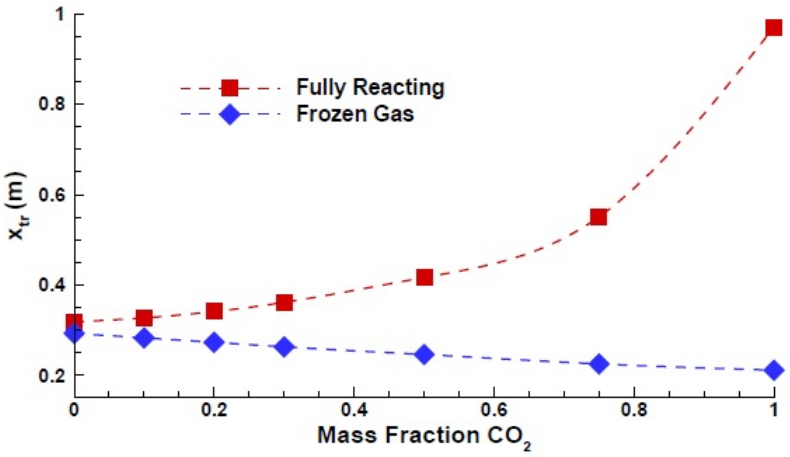

Figure 2.12. Numerical simulations with reacting and non-reacting flows on transition location [10] (with permission)

conditions here on Earth. As CO_2 has a lower dissociation energy than either N_2 or O_2 , there is an amount of freestream CO_2 that dissociates before the boundary layer. Neither the experiments nor the numerical simulations attempted to assess the actual concentration within the boundary layer or the effects of CO_2 dissociation across the shock and the consequent gas property changes.

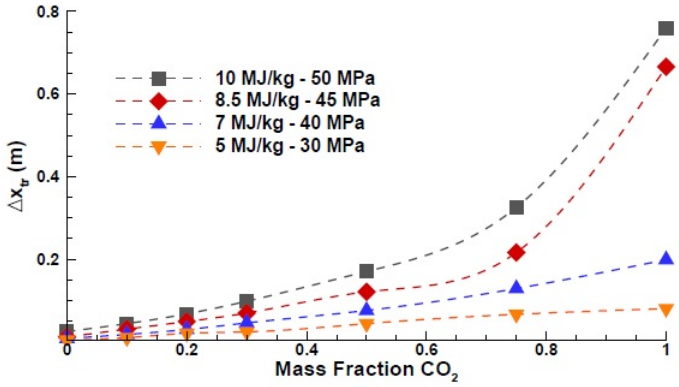

Figure 2.13. Numerical results of enthalpy and CO_2 concentration changes on transition location [10] (with permission)

3. Mathematical Models

3.1 Governing Equations

3.1.1 Conservation Equations.

To adequately model the physical processes in hypersonic flows, an enhanced set of the Navier-Stokes equations are required, including both chemical reactions and vibrational-electronic energy. Due to the inclusion of chemical reactions, each species in the flow must have a conservation equation. Also, a vibrational-electronic energy equation is included along with the translational-rotational energy equation. The divergence form of the conservation equations below are expressed in Einstein notation using Cartesian coordinates.

The species conservation equation is Equation 3.1 where ρ_s is the mass density of the species s, u_i is the fluid velocity in the x_i direction and v_{si} is the diffusion velocity of the species in the x_i direction. The term ω_s is the species chemical source term for species creation and is determined by the reactions allowed in the gas model as well as the gas-surface interaction model. The sum of all species densities will still preserve the total mass of the system.

$$\frac{\partial \rho_s}{\partial t} + \frac{\partial}{\partial x_i}(\rho_s u_i) = -\frac{\partial}{\partial x_i}(\rho_s v_{si}) + \omega_s \tag{3.1}$$

The conservation of mixture mass is given in Equation 3.2 where ρ is defined as the mixture density.

$$\frac{\partial \rho}{\partial t} + \frac{\partial}{\partial x_i}(\rho u_i) = 0 \tag{3.2}$$

$$\rho = \sum_s \rho_s \tag{3.3}$$

The conservation of momentum is given by Equation 3.4 where p is the fluid pressure, ρ is defined by 3.3 and τ_{ij} is the viscous stress tensor.

$$\frac{\partial}{\partial t}(\rho u_i) + \frac{\partial}{\partial x_i}(\rho u_i u_j) = -\frac{\partial p}{\partial x_i} + \frac{\partial \tau_{ij}}{\partial x_i} \tag{3.4}$$

The total energy of the system is conserved and given by Equation 3.5 where q_i is the heat transfer of translational and rotational energy and q_{vi} is the vibrational heat transfer in the i-direction and h_s is the enthalpy of species s.

$$\frac{\partial E}{\partial t} + \frac{\partial}{\partial x_j}(u_j(E+p)) = \frac{\partial}{\partial x_j}(u_i \tau_{ij}) - \frac{\partial q_i}{\partial x_i} - \frac{\partial q_{vi}}{\partial x_i} - \frac{\partial}{\partial x_i}\left(\sum_s \rho_s h_s v_{si}\right) \tag{3.5}$$

A vibrational-electronic energy conservation equation is added to the compressible Navier-Stokes equations and is given by Equation 3.6 where e_{vs} is the vibrational energy per unit mass of species s and Q_{t-v} is the translational-vibrational energy exchange.

$$\frac{\partial E_v}{\partial t} + \frac{\partial}{\partial x_i}(u_i E_v) = -\frac{\partial q_{vi}}{\partial x_i} - \frac{\partial}{\partial x_i}\left(\sum_s \rho_s e_{vs} v_{si}\right) + Q_{t-v} + \sum_s e_{vs} w_s \tag{3.6}$$

3.1.2 State Equations.

The total fluid pressure is found using the ideal gas law:

$$P = \rho R T = \sum_s \frac{\rho_s}{M_s} \mathcal{R} T \tag{3.7}$$

For this equation, T is the translational-rotational temperature, R is the gas constant specific to the mixture and $\mathcal{R}$ is the universal gas constant. The assumption

of a single translational-rotational temperature is valid due to the equilibration of the rotational state to the translational state within a few molecular collisions.

The total energy per unit volume of the fluid is defined as the sum of the kinetic energy and the internal energy states of the species in the flow, given by Equation 3.8.

$$E = \frac{1}{2}\rho u_i u_i + \sum_s \rho_s c_{vs} T + \sum_s^{nms} \rho_s e_{vs} + \sum_s \rho_s h_s^o \tag{3.8}$$

$$c_{vs} = c_{vs}^{tr} + c_{vs}^{rot} = \frac{3}{2}\frac{R}{M_s} + \frac{R}{M_s} \tag{3.9}$$

$$e_{vs} = g_s \frac{R}{M_s} \frac{\theta_{v,m}}{e^{\frac{\theta_{v,m}}{T_v}} - 1} \tag{3.10}$$

On a per-unit-volume basis, the first term is the kinetic energy of the flow. The second term, $\sum_s \rho_s c_{vs} T$ represents the internal energy in the species based on the translational-rotational temperature, T. The vibrational energy in the flow is given by $\sum_s^{nms} \rho_s e_{vs}$, where e_{vs} is determined by Equation 3.10 and $\theta_{v,m}$ is the characteristic vibrational temperature of mode m, nms is the number of vibrational modes and T_v is the vibrational temperature. The inclusion of the two temperature model, first developed by Park [31], allows for non-equilibrium in the flow. The formation energy of the species is defined by $\sum_s \rho_s h_s^o$, where h_s^0 is the formation enthalpy of species s. The specific heat at constant volume per species assumes a linear polyatomic structure and the vibrational energy per unit mass of species s, e_{vs}, assumes a harmonic oscillator model and a Boltzmann distribution for the vibrational states and g_s is the degeneracy for species s.

3.1.3 Transport Properties.

The Navier-Stokes equations above are closed through the relations for the transport properties of mass, momentum and heat. The transport of mass is expressed by the species diffusion as given by Fick's Law of mass diffusion which is:

$$\rho_s v_{si} = -\rho D_{sr} \frac{\partial}{\partial x_i} \left(\frac{\rho_s}{\rho} \right) \tag{3.11}$$

where D_{sr} is the binary diffusion constant of species s through species r, derived from a constant Lewis number. Lewis number represents the relationship between the thermal conductivity to the mass diffusion and is defined as:

$$Le = \frac{\kappa}{\rho c_p D} \tag{3.12}$$

where c_p and κ are mixture values. The mixture values of c_p, c_v, h^o and e_v are found using a mass-weighted average based on species concentration from Equation 3.13.

$$\phi = \sum_{s}^{ns} \phi_s \frac{\rho_s}{\rho} \tag{3.13}$$

The shear stress, τ_{ij}, is expressed by equation 3.14 and describes the transportation of momentum in the system where μ is the dynamic viscosity of the mixture. Stoke's hypothesis where $\lambda = -\frac{2}{3}\mu$ is used to determine the bulk viscosity. There has been some debate at the to suitability of Stoke's hypothesis on flows with poly-atomic particles, especially at hypersonic speeds [74]. It has been shown that the second coefficient of viscosity, λ, is nearly $10^3\mu$ for flows containing high concentrations of CO_2 [75]. However, despite nearly 150 years of debate, there still remains limited agreement on a viable alternative to Stoke's simplification.

$$\tau_{ij} = \mu \left(\frac{\partial u_i}{\partial x_j} + \frac{\partial u_j}{\partial x_i} + \frac{2}{3} \frac{\partial u_k}{\partial x_k} \delta_{ij} \right) \tag{3.14}$$

Finally, the heat flux is defined using Fourier's Law and allows for non-equilibrium based on the two temperature model for the translational and vibrational temperatures.

$$q_i = -\kappa \frac{\partial T}{\partial x_i} \tag{3.15}$$

$$q_v = -\kappa_v \frac{\partial T_v}{\partial x_i} \tag{3.16}$$

where κ is the translational-rotational heat conductivity of the gas mixture and κ_v is the vibrational heat conductivity.

The gas mixture viscosity and conductivity are found by using Wilke's mixing rule given by Equations 3.17 through 3.20

$$\mu = \sum_s \frac{\mu_s \rho_s M}{\phi_s \rho M_s} \tag{3.17}$$

$$\kappa = \sum_s \frac{\kappa_s \rho_s M}{\phi_s \rho M_s} \tag{3.18}$$

$$\kappa_v = \sum_s \frac{\kappa_{vs} \rho_s M}{\phi_s \rho M_s} \tag{3.19}$$

$$\phi_s = \sum_r \frac{\rho_r M}{\rho M_r} \left[1 + \sqrt{\frac{\mu_s}{\mu_r}} \left(\frac{M_r}{M_s} \right)^{\frac{1}{4}} \right]^2 \left[8 \left(1 + \left(\frac{M_s}{M_r} \right) \right) \right]^{-\frac{1}{2}} \tag{3.20}$$

The species viscosity is found using Blottner's model

$$\mu_s = 0.1 exp\left[\left(A_s lnT + B_s \right) lnT + C_s \right] \tag{3.21}$$

In this model, the constants A_s, B_s and C_s are constants determined for each species in the flow. The species conductivity is computed from Eucken's relation for translation, rotation and vibration:

$$\kappa_{tr,s} = \frac{5}{2}\mu_s c_{vs} \tag{3.22}$$

$$\kappa_{rot,s} = \mu_s c_{vs} \tag{3.23}$$

$$\kappa_{v,s} = \mu_s c_{vvs} = \mu_s \frac{\partial e_{vs}}{\partial T_v} \tag{3.24}$$

3.1.4 Chemical Source Term.

The chemical reaction considered in the models include dissociation and exchange reactions. The chemical production rate of a species, s, in a reaction q, is represented by [76]:

$$\omega_{s,q} = (\beta_{sq} - \alpha_{sq}) \left[k_{f,q} \prod_j \left(\frac{\rho_j}{M_j} \right)_{sq}^{\alpha} - k_{b,q} \prod_j \left(\frac{\rho_j}{M_j} \right)_{sq}^{\beta} \right] \tag{3.25}$$

where α and β are the stoichiometric coefficients for the reactions.

Using this production rate for for each reaction, the total source term for the species mass conservation is given by:

$$\omega_s = M_s \sum_q \omega_{s,q} \tag{3.26}$$

The dissociation reaction forward rates are based on Park's [31, 77, 78] geometric average of the translational-rotation and the vibrational-electronic temperatures

$$T = \sqrt{T T_v} \tag{3.27}$$

which also accounts for the vibrational-dissociation coupling [79] or the two temperature kinetic model[80]

$$T = T_v^q T^{1-q} \tag{3.28}$$

where q is a value between 0.3 and 0.5. US3D uses Equation 3.27 to calculate the temperature [30].

The backwards rates are determined from the forward rate and the equilibrium constants.

$$k_{b,q} = \frac{k_{f,q}}{K_{eq,q}} \tag{3.29}$$

$$K_{eq,q} = K_{a,q} \left(\frac{p_0}{RT} \right)^{\nu_{gq}} \tag{3.30}$$

$$\nu_{gq} = \sum_{k=1}^{K_g} \left(\nu_{kq}^{''} - \nu_{kq}^{'} \right) \tag{3.31}$$

$$K_{a,q} = exp \left[\frac{-\Delta G_q^o(T)}{RT} \right] = exp \left[- \sum_{k=1}^{K} \nu_{kq} \left(\frac{H_k(T)}{RT} - \frac{S_k(T)}{R} \right) \right] \tag{3.32}$$

where ν_{gq} is the stoichiometric exponent, ν_{kq} is the net stoichiometric constant for species k in reaction q and $G_q^o(T)$ is the Gibbs free energy. The US3D code uses the NASA Chemical Equilibrium with Applications(CEA) [81] database to compute the activity and concentration-based equilibrium constants.

3.1.5 Vibrational Source Terms.

The translational-vibrational energy exchange rate is calculated using the Landau-Teller model where $Q_{t-v,s}$ is the energy exchange rate between the vibrational-electronic and translational-rotational energy modes, $e_{v,s}$ is the vibrational energy evaluated at the translational-rotational temperature or the vibrational-electronic temperature at a relaxation time, τ_s.

$$Q_{t-v,s} = \rho_s \frac{e_{v,s}(T) - e_{v,s}(T_v)}{\tau_s} \tag{3.33}$$

The rate of change in vibrational state assumes molecules behave as harmonic oscillators and vibrational levels are restricted to one quantum level change at a time [67].

The relaxation time, τ_s, is found from the species averaged relaxation time

$$\tau_s = \frac{\sum_r X_r}{\sum_r \frac{X_r}{\tau_{sr}}} \tag{3.34}$$

The inter-species relaxation time is modeled using the Millikan and White [82] curve fit

$$\tau_{sr} = \frac{1}{p} exp\left[A_{sr}(T^{-\frac{1}{3}} - 0.015\mu_{ms}^{\frac{1}{4}}) - 18.42\right] \tag{3.35}$$

$$A_{sr} = 1.16x10^{-3}\mu_{sr}^{\frac{1}{2}}\theta_{v,s}^{\frac{4}{3}} \tag{3.36}$$

$$\mu_{sr} = \frac{M_s M_r}{M_s + M_r} \tag{3.37}$$

For these simulations, the relaxation time is corrected by a collision limited relaxation time if the flow reaches a very high temperatures, τ_{cs} [31]

$$\tau_{cs} = \frac{1}{\sigma_v c_s N} \tag{3.38}$$

$$c_s = \sqrt{\frac{8RT}{\pi M_s}} \tag{3.39}$$

$$\sigma_v = \sigma_{vs}\left(\frac{50000}{T}\right)^2 m^2 \tag{3.40}$$

where σ_{vs} is the limiting cross section for species s and can be found in Park [77], N is the number density for the mixture and c_s is the average molecular speed. In the

US3D code, if the limiting cross section is not specified the value defaults to that for Nitrogen, $3 \times 10^{-21} m^2$.

3.1.6 Boundary Layer Equations.

Using the Navier-Stokes equations from section 3.1.1, the conservation equations for the boundary layer can be derived and has been accomplished at varying levels of difficulty by multiple authors [83, 18, 52]. The basis for boundary layer theory was originally developed by Prandtl to explain the viscous effects near the surface where the no-slip boundary condition brings the fluid to rest and shear stresses exist. As these viscous effects are confined to a thin layer near the surface of the body, it is convenient to solve the inviscid flow and the more complex viscous boundary layer flow separately. There are defined three different boundary layers thicknesses used in defining a boundary layer: velocity boundary layer thickness, thermal boundary layer thickness and the species concentration boundary layer thickness. Each boundary layer thickness relates to the physical conservation on momentum, energy and mass, respectively. The thicknesses of each boundary layer increases with distance from the leading edge. The main purpose of the boundary layer theory is to determine the gradients in velocity and temperature to define the shear stress and the heat transfer to the surface. Some fundamental boundary layer dimension quantities are the displacement thickness and momentum thickness. These values are often used to determine an edge Reynolds number or edge Mach number often used in stability theory.

The displacement thickness is defined as

$$\delta^* = \int_0^\infty [1 - \frac{u}{U_\infty}] dy \tag{3.41}$$

and proportional to the $\sqrt{\nu}$, the kinematic viscosity. The physical interpretation of the displacement thickness is the amount an streamline in the mean flow is deflected due to the presence of the boundary layer.

Similarly, the momentum thickness is defined as the decrease in momentum flow due to the presence of the boundary layer and is defined by the equation

$$\theta^* = \int_0^\infty \frac{u}{U_\infty}\left[1 - \frac{u}{U_\infty}\right] dy \tag{3.42}$$

To calculate the governing equations of the boundary layer, an order of magnitude analysis is made on the complete Navier-Stokes equations using the assumption that the boundary layer thickness is much less than the length scale used, the flow is steady-state, and the Reynolds number is large [18]. For a simple, two-dimensional flow, this reduction of the conservation equations results in Equations 3.43 through 3.46.

$$\frac{\partial}{\partial x_i}(\rho_s u_i) = -\frac{\partial}{\partial y}(\rho_s v_{si}) + \omega_s \tag{3.43}$$

$$\rho u\frac{\partial u}{\partial x} + \rho v\frac{\partial u}{\partial y} = -\frac{\partial p}{\partial x} + \frac{\partial}{\partial y}\left(\mu\frac{\partial u}{\partial y}\right) \tag{3.44}$$

$$0 = -\frac{\partial p}{\partial y} \tag{3.45}$$

$$\rho u\frac{\partial h}{\partial x} + \rho v\frac{\partial h}{\partial y} = \mu\left(\frac{\partial u}{\partial y}\right)^2 + u\frac{\partial p}{\partial x} + \frac{\partial}{\partial y}(\kappa\frac{\partial T}{\partial y} + \kappa_v\frac{\partial T_v}{\partial y}) \tag{3.46}$$

Boundary conditions for these equations are such that the flow comes to rest at the surface and at $y \to \infty$, the edge of the boundary layer, return to freestream values. The x-direction is assumed to be parallel with the surface and the y-direction is normal to the surface. At lower Mach numbers, the flow structure does not support a static pressure gradient in the body-normal direction as there is no momentum available to maintain the pressure difference. The y-momentum equation will not hold true at very large hypersonic Mach numbers, for as the Mach grows large, the assumption that pressure is constant in the normal direction through the boundary layer is no longer valid. Phenomenologically, if the freestream Mach number is large enough so that $\frac{1}{\gamma M^2}$ is on the order of the displacement thickness, than the assumption that $\frac{\partial p}{\partial y}$ must also be on the same order as the displacement thickness is not true and can thus be large which would allow for such a pressure differential [52].

3.2 Linear Stability Theory

Linear Stability Theory (LST) owes its initial development to the combined efforts of work of hydrodynamic stability theorists such as Rayleigh, Orr, Sommerfeld, Tollmien, Schlichting and Lin for the theoretical development of the incompressible theory [84] . This theory was supported with careful experimentation including those by Liepmann [85] and Schubauer and Skramstad [86]. The over-arching conclusion established from these works was that in an incompressible fluid, the flow will become unstable above a specific critical Reynolds number and cause the flow to transition from laminar to turbulent. It was the development of the Tollmien-Schlichting waves, a self-excited inviscid disturbance in the flow, that grow large enough to cause transition from laminar to turbulent flow. Building upon the incompressible theory, Lees and Lin [87] developed the compressible theory, which was later expanded by Lees [87], Dunn and Lin [88] and Lees and Reshotko [89]. In compressible stability the-

ory, the basic stability mechanisms found in incompressible theory still exist, but the relative importance of each mechanism changes due to the appreciable interchange of mechanical and heat energy [87]. Specifically, the compressibility of the fluid and the conductivity can no longer be neglected [87] and the viscous dissipation becomes the dominant factor for stability and so terms with gradients of viscosity, conductivity and dissipation become important. The changes in pressure fluctuations and the production of disturbance energy and viscous dissipation near the surface due to an increased Mach number make terms previously neglected in incompressible theory important [89]. Lees and Reshotko showed that the inviscid pressure fluctuations decrease farther from the surface in compressible flow at higher Mach numbers [89].

The basic concept of linear stability theory is derived from the Navier-Stokes equations of motion, either in the incompressible or compressible forms depending on the flow. Into these equations the values for the flow quantities are then expressed as a steady mean flow value and a fluctuation term shown in Equation 3.48. A critical assumption of parallel, or locally-parallel, flow is made in which the mean-flow quantities are a function only of the normal direction [27].

$$q(x, y, z, t) = Q(x, y, z) + q\prime(x, y, z, t) \tag{3.47}$$

$$q' = \phi e^{[i(\alpha x + \beta z - \omega t)]} \tag{3.48}$$

where $U = U(y)$, $W = W(y)$ and $V = 0$ and ϕ represents the disturbance amplitude.

These values are substituted into the Navier-Stokes equations and the mean flow is subtracted out resulting in expressions for the fluctuating values. The resulting equations are then further simplified by linearization, based on the assumption of small fluctuations, and any term where fluctuations, or derivatives of fluctuations, are multiplied can be neglected. The disturbance equations for dimensionless, linear

compressible flow as developed by Mack without chemical reactions [19] are shown in Equations 3.50 through 3.54, with conservation of mass, momentum and energy, respectively.

$$\frac{\partial r}{\partial t} + \rho\left(\frac{\partial u}{\partial x} + \frac{\partial v}{\partial y} + \frac{\partial w}{\partial z}\right) + v\frac{\partial p}{\partial y} + U\frac{\partial r}{\partial x} + W\frac{\partial r}{\partial z} = 0 \tag{3.49}$$

$$\begin{aligned}
\rho\left(\frac{\partial u}{\partial t} + U\frac{\partial u}{\partial x} + v\frac{\partial U}{\partial y} + W\frac{\partial u}{\partial z}\right) &= -\frac{1}{\gamma M_e^2}\frac{\partial p}{\partial x} \\
+\frac{1}{R}\left[2\mu\frac{\partial^2 u}{\partial x^2} + \mu\left(\frac{\partial^2 u}{\partial y^2} + \frac{\partial^2 u}{\partial z^2} + \frac{\partial^2 v}{\partial x \partial y} + \frac{\partial^2 w}{\partial x \partial z}\right)\right] & \\
+\frac{1}{R}\left[\frac{2}{3}(\lambda-\mu)\left(\frac{\partial^2 u}{\partial y^2} + \frac{\partial^2 v}{\partial x \partial y} + \frac{\partial^2 w}{\partial x \partial z}\right) + \frac{\partial \mu}{\partial T}\frac{\partial T}{\partial y}\left(\frac{\partial u}{\partial y} + \frac{\partial v}{\partial x}\right)\right] & \\
+\frac{1}{R}\left[\frac{\partial \mu}{\partial T}\left(\frac{\partial^2 U}{\partial y^2}\theta + \frac{\partial U}{\partial y}\frac{\partial \theta}{\partial y}\right) + \frac{\partial^2 \mu}{\partial T^2}\frac{\partial T}{\partial y}\frac{\partial U}{\partial y}\theta\right] &
\end{aligned} \tag{3.50}$$

$$\begin{aligned}
\rho\left(\frac{\partial v}{\partial t} + U\frac{\partial v}{\partial x} + W\frac{\partial v}{\partial z}\right) &= -\frac{1}{\gamma M_e^2}\frac{\partial p}{\partial y} \\
+\frac{1}{R}\left[2\mu\frac{\partial^2 v}{\partial y^2} + \mu\left(\frac{\partial^2 v}{\partial x^2} + \frac{\partial^2 v}{\partial z^2} + \frac{\partial^2 u}{\partial x \partial y} + \frac{\partial^2 w}{\partial y \partial z}\right)\right] & \\
+\frac{1}{R}\left[\frac{2}{3}(\lambda-\mu)\left(\frac{\partial^2 v}{\partial y^2} + \frac{\partial^2 u}{\partial x \partial y} + \frac{\partial^2 w}{\partial y \partial z}\right) + \frac{\partial \mu}{\partial T}\left(2\frac{\partial T}{\partial y}\frac{\partial v}{\partial y} + \frac{\partial U}{\partial y}\frac{\partial \theta}{\partial x} + \frac{\partial W}{\partial y}\frac{\partial \theta}{\partial z}\right)\right] & \\
+\frac{1}{R}\left[\frac{2}{3}\left(\frac{\partial \lambda}{\partial T} - \frac{\partial \mu}{\partial T}\right)\frac{\partial T}{\partial y}\left(\frac{\partial u}{\partial x} + \frac{\partial v}{\partial y} + \frac{\partial w}{\partial z}\right)\right] &
\end{aligned} \tag{3.51}$$

$$\begin{aligned}\rho\left(\frac{\partial w}{\partial t}+U\frac{\partial w}{\partial x}+v\frac{\partial W}{\partial y}+W\frac{\partial w}{\partial z}\right)&=-\frac{1}{\gamma M_e^2}\frac{\partial p}{\partial z}\\ &+\frac{1}{R}\left[2\mu\frac{\partial^2 w}{\partial z^2}+\mu\left(\frac{\partial^2 w}{\partial y^2}+\frac{\partial^2 w}{\partial y^2}+\frac{\partial^2 v}{\partial y\partial z}+\frac{\partial^2 u}{\partial x\partial z}\right)\right]\\ &+\frac{1}{R}\left[\frac{2}{3}(\lambda-\mu)\left(\frac{\partial^2 w}{\partial z^2}+\frac{\partial^2 u}{\partial x\partial z}+\frac{\partial^2 v}{\partial y\partial z}\right)+\frac{\partial\mu}{\partial T}\left(\frac{\partial^2 w}{\partial y^2}\theta+\frac{\partial w}{\partial y}\frac{\partial\theta}{\partial y}\right)\right]\\ &+\frac{1}{R}\left[\frac{\partial^2\mu}{\partial T^2}\frac{\partial T}{\partial y}\frac{\partial w}{\partial y}\theta+\frac{\partial\mu}{\partial T}\frac{\partial T}{\partial y}\left(\frac{\partial w}{\partial y}+\frac{\partial v}{\partial z}\right)\right]\end{aligned}\tag{3.52}$$

$$\begin{aligned}\rho\left(\frac{\partial\theta}{\partial t}+U\frac{\partial\theta}{\partial x}+v\frac{\partial\theta}{\partial y}+W\frac{\partial\theta}{\partial z}\right)&=-(\gamma-1)\left(\frac{\partial u}{\partial x}+\frac{\partial v}{\partial y}+\frac{\partial w}{\partial z}\right)\\ &+\frac{\gamma\mu}{PrR}\left[\frac{\partial^2\theta}{\partial x^2}+\frac{\partial^2\theta}{\partial y^2}+\frac{\partial^2\theta}{\partial z^2}+\frac{1}{\kappa}\frac{\partial\kappa}{\partial T}\frac{\partial^2 T}{\partial y^2}\theta+\frac{2}{\kappa}\frac{\partial\kappa}{\partial T}\frac{\partial T}{\partial y}\frac{\partial\theta}{\partial y}+\frac{1}{\kappa}\frac{\partial^2\kappa}{\partial T^2}\left(\frac{\partial T}{\partial y}\right)^2\theta\right]\\ &+\gamma(\gamma-1)M_e^2\frac{1}{R}\left[2\mu\frac{\partial U}{\partial y}\left(\frac{\partial u}{\partial y}+\frac{\partial v}{\partial x}\right)+2\mu\frac{\partial W}{\partial y}\left(\frac{\partial v}{\partial z}+\frac{\partial w}{\partial y}\right)+\frac{\partial\mu}{\partial T}\left(\frac{\partial U}{\partial y}\right)^2\theta\right]\\ &+\gamma(\gamma-1)M_e^2\frac{1}{R}\left[\frac{\partial\mu}{\partial T}\left(\frac{\partial W}{\partial y}\right)^2\theta\right]\end{aligned}\tag{3.53}$$

where R is the reference Reynolds number, $R=\sqrt{Re}=\frac{U_e L}{\nu_e}=\left(\frac{U_e x}{\nu_e}\right)^{\frac{1}{2}}$, Pr is the Prandtl number, given by $\frac{\kappa}{c_p\mu}$, γ is the ratio of specific heats, and θ and r are the temperature and density disturbances, respectively.

These can be also be expressed with terms for chemical reaction by including species density and forcing terms, F_n [90] where ϕ is a vector of the disturbance quantities and the coefficients are Jacobian matrices depending only on the mean flow quantities or their derivatives.

$$\begin{aligned} \Gamma\frac{\partial\phi}{\partial t} + A\frac{\partial\phi}{\partial x} + B\frac{\partial\phi}{\partial y} + C\frac{\partial\phi}{\partial z} + D\phi \\ +V_{xx}\frac{\partial^2\phi}{\partial x^2} + V_{yy}\frac{\partial^2\phi}{\partial y^2} + V_{zz}\frac{\partial^2\phi}{\partial z^2} \\ +V_{xy}\frac{\partial^2\phi}{\partial x\partial y} + V_{xz}\frac{\partial^2\phi}{\partial x\partial z} + V_{zy}\frac{\partial^2\phi}{\partial y\partial z} + F^n = 0 \end{aligned} \tag{3.54}$$

$$\phi = (\rho'_1, \cdots \rho'_{ns}, u', v', w', p', T', T'_v) \tag{3.55}$$

3.2.1 Linear Stability Equations.

Based on the parallel flow assumption, the coefficients of the disturbance equations are functions only of the normal direction and therefore the actual solution to these equations can be introduced as [19]

$$[u, v, w, p, r, \theta]^T = [\hat{u}(y), \hat{v}(y), \hat{w}(y), \hat{p}(y), \hat{r}(y), \hat{\theta}(y)]^T \exp\left[i\left(\int \alpha x + \beta z - \omega t\right)\right] \tag{3.56}$$

This type of disturbance is known as a modal disturbance and assumed to be sinusoidal in nature and the values of α, β and ω may be either real or complex depending on whether a temporal or spatial stability is being analyzed [19]. When substituted into the LST equations, a system of ordinary differential equations are obtained to solve for α, β and ω. For axi-symmetric flow, the values of β are set to zero. For temporal amplification, α and β are assumed to be real, while ω is complex, $\omega = \omega_r + \omega_i$. For spatial amplification, ω is real while α and β are complex. Therefore, the sign of the imaginary quantity determines whether the disturbance will be damped or amplified. For two dimensional, spatial amplification to determine

the location of transition, the solutions for α_i are used to build the stability diagram (see Figure 3.1).

A relation between temporal and spatial amplification is given by Gaster's relations [91]

$$\alpha_i(s) = \frac{\alpha c_i(T)}{c_g} \tag{3.57}$$

$$c_g = \frac{\partial(\alpha c_r)}{\partial \alpha} = c_r + \alpha \frac{\partial c_r}{\partial \alpha} \tag{3.58}$$

where c_g is the group velocity.

When Equation 3.56 is substituted into the disturbance equations, the results are the stability equations. For incompressible flow, and assuming Squires theorem, these equations can be reduced to the Orr-Sommerfield equation, a fourth order system to solve for a two-dimensional boundary layer. For compressible flow, the equations form an eighth-order system of equations, which can be reduced to a sixth-order system with the assumption that one of the four dissipation terms in the energy solution is negligible [19]. The eigenvalues of the stability equations are calculated to find the stability of the flow, with the specification of both the Reynolds number and frequency, as well as with the satisfaction of the boundary conditions. The results are most often displayed in a stability diagram. An example of the stability diagram for a Blasius boundary layer shown in the Figure 3.1. These curves are often referred to as thumbprint curves and represent the regions of instability where disturbances are amplified. The neutral curve is that line where the amplification, $-\alpha_i = 0$. This curve is the boundary between areas of amplification and damping. The curves where $-\alpha_i$ is positive show areas of instability.

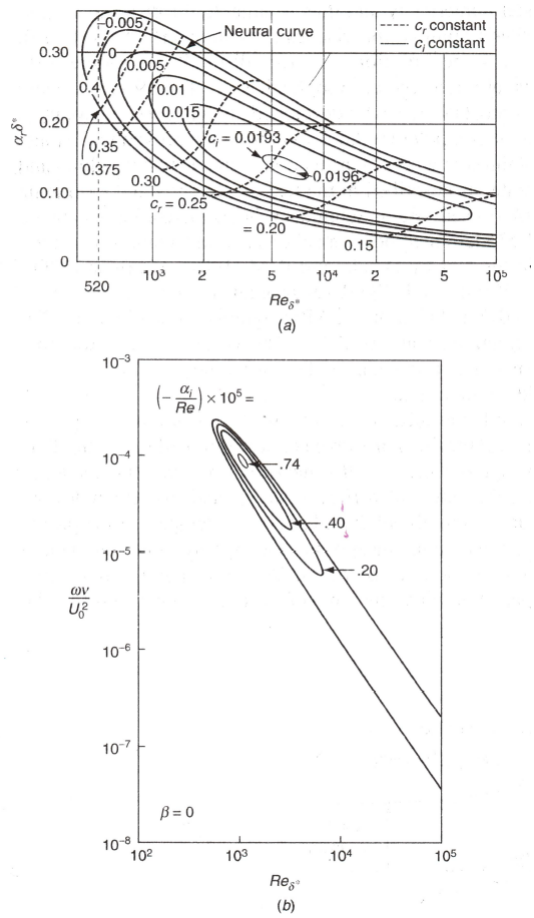

Figure 3.1. Stability Diagram for Blasius Boundary Layer for (a) Spatial and (b)Temporal Analysis [3] (with permission)

3.3 Numerical Models

The numerical methods used in this research to solve the flow used the compressible, reacting Navier-Stokes equation using a finite volume method. The finite volume approach solves the Navier-Stokes conservation laws in Cartesian coordinates and can be expressed by Equation 3.59, where U is defined as the vector of conserved variables, $\vec{F}$ is the sum of inviscid and viscous fluxes and the source term, W, is a matrix with the species production terms and the change in vibrational energy.

$$\frac{\partial U}{\partial t} + \bigtriangledown \cdot \vec{F} = W \tag{3.59}$$

$$U = [\rho_s, \rho u_i, E_v, E]^T \tag{3.60}$$

$$W = [\omega_s, 0, Q_{t-v} + \sum e_{vs}\omega_s, 0]^T \tag{3.61}$$

Integrating Equation 3.59 over an arbitrary volume results in Equation 3.62 where $\bar{U}$ and $\bar{W}$ equal the averaged quantities of the finite volume element, V is the volume and $\partial\Omega$ represents the surface of the volume.

$$\frac{\partial \bar{U}}{\partial t} + \frac{1}{V}\int_{\partial\Omega} (\vec{F} \cdot \vec{n}) dS = \bar{W} \tag{3.62}$$

If the volume is assumed to be a polygon, then Equation 3.62 can be re-written to

$$\frac{\partial \bar{U}}{\partial t} + \frac{1}{V}\sum_{sides} (\vec{F} \cdot \vec{n}) S = \bar{W} \tag{3.63}$$

where S is the face surface area. This equation is discretized over the flow domain to solve for the average value in each polygon or grid cell. The conserved variables represent the values of the cell center and the fluxes at the face will be reconstructed from those values.

3.3.1 Fluxes.

The inviscid flux vector in X-Cartesian coordinate direction is

$$F_I = [\rho_s u, \cdots, \rho uu + P, \rho uv, \rho uw, E_v u, (E + P)u]^T \tag{3.64}$$

This equation can be written for both y- and z- directions substituting the velocity component in that direction in for u. Due to the hyperbolic nature of the inviscid

fluxes when Mach is greater than 1, the flow variables travel along characteristics. US3D uses a Steger-Warming flux-vector splitting method to solve the inviscid fluxes [30, 92]. In the original upwind Steger-Warming method, the fluxes are split according to the signs of the characteristic speeds of the flow [92].

$$\vec{F_I}(U) = AU = \frac{\partial \vec{F}}{\partial U} U \tag{3.65}$$

This flux can then be split into left and right moving components based on the characteristic velocity, which are defined by the eigenvalues of A, the flux Jacobian. Since A is difficult to diagonalize, the introduction of V, a matrix of primitive variables is used such that

$$V = [\rho_s, u_i, e_v, p]^T A = \frac{\partial U}{\partial V}\frac{\partial V}{\partial U}\frac{\partial \vec{F_I}}{\partial V}\frac{\partial V}{\partial U} \tag{3.66}$$

$$\frac{\partial V}{\partial U}\frac{\partial \vec{F_I}}{\partial V} = C^{-1}\Lambda C \tag{3.67}$$

$$S = \frac{\partial U}{\partial V} \tag{3.68}$$

Λ is a diagonal matrix of the eigenvalues ($\lambda = u, u+a, u-a$) and C is a matrix of the associated eigenvectors. Λ can then be split into positive and negative moving characteristics by making Λ_+ all the positive eigenvalues and Λ_- the negative eignevalues. Thus the total flux then becomes the sum of the fluxes

$$\vec{F_+} = S^{-1}C^{-1}\Lambda_+ CSU \tag{3.69}$$

$$\vec{F_-} = S^{-1}C^{-1}\Lambda_- CSU \tag{3.70}$$

$$\vec{F_I} = \vec{F_+} + \vec{F_-} \tag{3.71}$$

Often, the flux must be evaluated at the local coordinate system based on the face normal direction, in which case the contravariant velocity shown in Equation 3.74 is used in place of u and $\vec{F_I}$ becomes

$$\vec{F_I} \cdot \vec{n} = F_I' \tag{3.72}$$

$$\vec{n} = [s_x, s_y, s_z] \tag{3.73}$$

$$u' = us_x + vs_y + ws_z \tag{3.74}$$

The original implementation of the Steger-Warming method is fairly dissipative in nature [92] and is usually modified [30, 93]. The modification includes calculating the Jacobians from an arithmetic average of the neighboring cells and is known as the Modified Steger-Warming Method [93]. This central-difference method reduces the numerical dissipation, but is not used in the area of shocks due to the high gradients [92]. In this research, a pressure switch is used to transition between the original and modified methods when large pressure gradients exist [30].

To obtain second-order spatial accuracy, a MUSCL (Monotonic Upwind Scheme for Conservation Laws) [94] approach is chosen in the simulations. In this method, the fluxes are evaluated in estimates of the left and right data, which are calculated by extrapolating the face value from neighboring data, such as [95]

$$U^L = \frac{3}{2}U_i - \frac{1}{2}U_{i-1} \tag{3.75}$$

$$U^R = \frac{3}{2}U_{i+1} - \frac{1}{2}U_{i+1} \tag{3.76}$$

In the presence of strong gradients, this averaging will produce an aphysical result and is limited so that new extrema aren't produced. A limiter is often used to eliminate the new extrema, such as the minmod function which takes the smaller of two arguments if they have the same sign else returns a zero if the signs are different [95].

The viscous flux is defined by Equation 3.77.

$$\vec{F_V} = [\rho_s v_{s,x}, \cdots, -\tau_{xx}, -\tau_{xy}, -\tau_{xz}, q_{v,x} + \sum \rho_s e_v v_{s,x}, q_x + q_{v,x} - u_i \tau_{i,x} + \sum \rho_s e_v v_{s,x}]^T \tag{3.77}$$

As the viscous fluxes are elliptic in natures, they are calculated using a central-based scheme [30] where the flow variables are calculated by an average of the neighboring cells and the derivative quantities are calculated using a deferred correction method [30]. The cell-centered gradients needed are calculated using a weighted least-squares reconstruction.

3.3.2 Time Advancement.

US3D uses Data-Parallel Line-Relaxation method for implicit time advancement [30, 96]. Re-writing the finite volume governing equation in temporal form is shown in Equation 3.78

$$\frac{\partial U^n}{\partial t} + \frac{1}{V} \sum_{faces} (F_I^{n+1} + F_V^{n+1}) S = W^{n+1} \tag{3.78}$$

Linearization of the flux and production terms results in

$$F_I^{n+1} \simeq \vec{F^n} + \frac{\partial F_I^n}{\partial U} \partial U^n \tag{3.79}$$

$$W^{n+1} \simeq \vec{W^n} + \frac{\partial W^n}{\partial U} \partial U^n \tag{3.80}$$

$$\partial U^n = U^{n+1} - U^n \tag{3.81}$$

This system of linear equations is then solved using the DPLR method [96] in which off-line terms are updated during a relaxation process. This relaxation process involves a series of relaxation steps for ∂U^n

$$\partial U^0 = 0$$

for k=1,kmax

$$\partial U^k + \frac{\Delta t}{V} \sum_{online} A^+ \partial U^L + A^- \partial U^R)^k S - \frac{\partial W^n}{\partial U} \partial U^k = -\frac{1}{V} \sum F^n S + W^n$$
$$-\frac{1}{V} \sum_{offline} A^+ \partial U^L + A^- \partial U^R)^{k-1} S$$

$$\partial U^n = \partial U^{k_{max}} \tag{3.82}$$

The on-line elements are on the left hand side of the solution while the off like elements are relaxed to the right hand side. For these simulations, k_{max} was set to 4 for optimal convergence [97]. Line relaxation approaches are particularly effective for high Reynolds number flows especially when the grid is highly stretched to resolve the near-wall boundary layer and is much less computationally expensive than solving the full system of equations [97]. Candler et al in [96] and [95] provide greater detail into the DPLR approach.

3.4 Gas-Surface Models for Wall Boundary Conditions

The finite-rate model for surface-gas interactions was developed by Marschall and MacLean [13, 98]. The model is based on the separation of the system into three environments: the gas, surface (s) and bulk (b) environments. The gas environment is a single phase defined by multiple gas species. The surface environment has multiple phases, each containing a fraction of the total surface area, which contain a finite number of active sites where surface reactions can occur. The surface species consist of the adsorbed species as well as available sites. The total number of sites is conserved in the model to limit the surface reactions based on physical material limitations. The bulk environment consists of the solid phase with species that could participate in the ablation process. For a graphite ablator, the total number of bulk species is 1, carbon. The separation of the environments allows for surface reactions with species in different states, i.e. gas vs solid, to specify appropriate rate parameters.

At the surface, the boundary condition for each species is set by a mass balance in the gas phase of mass fluxes entering and leaving each control volume in the CFD simulation. The equation for this is mass balance is

$$\rho_w D_k \delta y_k \rfloor_w + M_k \omega_k = \rho_w v_w y_{k,w} \tag{3.83}$$

where y_k denotes the k species mass fraction and v_w is the normal velocity at the surface. This balance is shown in Figure 3.2 [11]. Each gas-surface model determines the species production term in this equation based on the reactions allowed and reaction rates used.

The source term used as the boundary condition at the surface is determined by the specific forward and backward rates specified in the gas-surface interaction model.

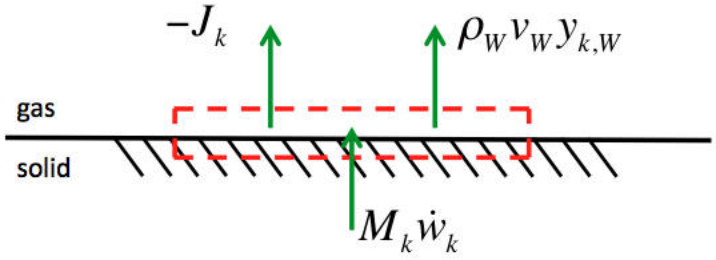

Figure 3.2. Gas-Surface Mass Balance Boundary Condition [11] (with permissions)

The forward equilibrium rates are determined by one of the reaction types specified in Table 3.1[13]

Reaction Type	Rate Formula	Specified Parameters
0: Arrhenius	$k_f = AT'^{\beta}\exp\left(-\frac{E}{RT}\right)$	A, β, E
1: Adsorption:	$k_f = \left[\frac{\bar{v}}{4\Phi_s^{v_s}}\right] S_0 T'^{\beta}\exp\left(-\frac{E_{ad}}{RT}\right)$	S_0, β, E_{ad}
2: Eley-Rideal	$k_f = \left[\frac{\bar{v}}{4\Phi_s^{v_s}}\right] \gamma_0 T'^{\beta}\exp\left(-\frac{E_{er}}{RT}\right)$	γ_0, β, E_{er}
3. Langmuir-Hinshelwood	$k_f = \left[\bar{v}_{2D}\Phi_s^{(1.5-v_s)}\sqrt{A_v}\right] C_{lh} T'^{\beta}\exp\left(-\frac{E_{lh}}{RT}\right)$	C_{lh}, β, E_{lh}
4. Sublimation	$k_f = \left[\frac{\bar{v}}{4\Phi_s^{v_s} RT}\right] \gamma_{sub} T'^{\beta}\exp\left(-\frac{E_{sub}}{RT}\right)$	$\gamma_{sub}, \beta, E_{sub}$

Table 3.1. Forward Reaction Rates [13] (with permissions)

The Arrhenius formulation, the most simple to implement as a surface reaction, is difficult to relate the coefficients to physical processes and so are often replaced by the Eley-Rideal (ER), adsorption, Langmuir-Hinshelwood (LH) or sublimation formulation [11]. These kinetic-based formulas require a total active site density, Φ to be specified. Also, a sticking coefficient, S_0 or an ER reaction efficiency, γ_{ER}, dimensionless quantities are used and have values between zero and one. For the ER mechanism, only one of the molecules is adsorbed onto the surface while the other reacts directly from the gas phase. However, for the LH mechanism, both molecules adsorb to neighboring sites and then undergo molecular reactions.

The backward rate coefficient is found by dividing the equilibrium constant (found by Equation 3.30) by the forward rate. For adsorption and desorption, the equilibrium constants are defined directly using [13]

$$K_{eq} = A_{eq} T' K_0 exp\left(\frac{E_{des} - E_{ad}}{RT}\right) \tag{3.84}$$

where E_{ad} or E_{des} are activation energies and $T' = \frac{T}{1K}$. A_{eq} can be found using either a mobile or immobile formulation based on the assumption of whether an adsorbed molecule can move on the surface or whether it is fixed.

$$A_{eq} = \frac{A_v}{B}(mobile) \tag{3.85}$$

$$A_{eq} = A_v(immobile) \tag{3.86}$$

and K_0 is

$$K_0 = \left(\frac{2\pi M_i RT}{A_v^2 h^2}\right)^{-\frac{1}{2}}(mobile) \tag{3.87}$$

$$K_0 = \left(\frac{2\pi M_i RT}{A_v^2 h^2}\right)^{-\frac{3}{2}}(immobile) \tag{3.88}$$

3.4.1 Park Models.

The Park models, called Park76 and Park in this research, are derived from the works of Park [32, 31, 99, 100] and Chen and Milos [101] and are emperical in nature. The surface reactions used in this model are shown in Tables 3.2 and 3.3. The earlier Park76 model does not contain any surface reactions with nitrogen and no sublimation/condensation of C_3 which is an obvious weakness to the model. Both models are fairly low fidelity models only accounting for oxidation reactions, though the Park model does allow for a sublimation/condensation reaction with C_3 and a

nitridation reaction. Further criticism of the model is the lack of backwards reaction rates, except for the condensation of C_3 in the Park model, and adherence to the linear Arrhenius reaction form despite non-linearity shown in experimentation [102, 60]. The Arrhenius expression can be valid over a limited range of temperatures and pressures, but cannot be applied reliably outside that range [102]. While these models do not consider a large number of reactions, they are computationally inexpensive and produce adequate agreement with experimental data at moderate temperatures.

3.4.2 Zhluktov and Abe (ZA) Model.

Zhluktov and Abe [14] later created a different kinetic finite-rate gas-surface model with 12 separate reactions shown in the Table 3.4 [14]. The rates derived for this model were empirical in nature and were determined to provide general fit to the data rather than match a specific data set due to the wide variations in experimental results [14]. In this model the surface reactions take place in both directions, as opposed to the Park model. This model does still include the simple Arrhenius form for some reactions, but also include adorption, desorption and Eley-Rideal reactions to better match wider temperature and pressure conditions [14]. One of main criticisms of the model is the lack of nitridation reactions creating CN in the flow, which has been seen in experimental results and also adds competition to the oxidation reactions [102]. The original implementation of this model into the US3D code, as given by Candler [103], did not define the desorption rates of O and N as was provided in the original ZA model nor did it allow for the mobile site parameter which was originally included in the ZA model [15].

3.4.3 Modified Zhluktov and Abe (MZA) Model.

The ZA model above was modified in the US3D code by Alba to include the calculate of the mobile site coefficient and the desorption rates for O and N [15]. The modification involved first computing the surface coverage for adsorbed N and O atoms and then computing the formation of gas phase species through a kinetics-based process [103]. The desorption rates for the modified model are given in Table 3.4 in reaction 1b and 2b [15]. While addressing some of the limitations of the original implementation of the ZA code, the nitridation reactions were still not included.

3.4.4 Modified Zhluktov and Abe Model with Nitridation.

In addition to modifying the ZA model with the adsorption/desorption of O and N atoms, Alba also expanded the model to include carbon nitridation reactions, both by direct nitridation and adsorbed nitrogen on the surface addressing one of the limitations found in the ZA model [15, 102]. Alba also updated oxidation reaction rates based on his experimentation and includes the mobile site parameter [15]. Table 3.5 gives the forward rate model used for the nitridation reactions [15].

3.4.5 MURI Model.

A Multi-University Research Initiative (MURI) executed by University of Minnesota and University of Montana produced new oxidation reaction rates based off electron beam experiments conducted in 2017 [16]. Macroscopic finite rates were constructed off the scattered fluxes determined during the experiments. One of the key assumptions made in the development of the model was the flux of O atoms detected in the scattered products was equal to the incident O atom flux and any products where the desorption time was greater than the data collection window were not considered [16]. This model was later examined by Swaminathan-Gopalan et al. in a

Direct Simulation Monte Carlo (DSMC) showed a number of discrepancies when time-of-flight and angular distribution were considered [104]. The DSMC results showed that many of the rates did not include the thermally desorbed components of oxygen, the slow components of CO distributions or the impulsively scattered O atoms [104]. These changes to the MURI model are still being developed and validated. Another limitation of the model was the inclusion of only of the oxidation reaction. The implementation of this model for this study included the updated oxidation rates shown in Table 3.6 with the inclusion of the ZA model reactions for nitrogen adsorption and desorption and carbon sublimation (reactions 2, 2b, 5, 9, 10, 11, and 12 from Table 3.4). The implementation did not include carbon nitridation as this was shown by Alba to impact the oxidation rates [15].

Table 3.2. Park 76 model[13]

	reaction	γ	E $(\frac{kJ}{gmol})$
1	$O_2 + (s1) + C(b) \rightarrow CO + O + (s1)$	0.01	0
2	$O + (s1) + C(b) \rightarrow CO + (s1)$	0.63	9.6444
3	$O + (s2) \rightarrow O + (s2)$	0.63	9.6444
4	$O + O(s2) \rightarrow O_2 + (s2)$	0.63	9.6444

Table 3.3. Park model[13]

	reaction	γ	E $(\frac{kJ}{gmol})$
1	$O + (s) + C(b) \rightarrow CO + (s)$	0.63	9.644
2	$O_2 + (s) + 2C(b) \rightarrow 2CO + 2(s)$	0.50	0
3	$N + (s) + C(b) \rightarrow CN + (s)$	0.30	0
4	$3(s) + 3C(b) \rightarrow C_3 + 3(s)$	$5.19x10^{13}$	775.81
5	$C_3 + 3(s) \rightarrow 3(s) + 3C(b)$	0.610	0

Table 3.4. Zhluktov and Abe (ZA) model[14]

	reaction	type	$S_0/\gamma_{ER}/A/\nu$	$\acute{T}^{\beta}$	E ($\frac{kJ}{gmol}$)
1	$O+(s) \leftrightarrow O(s)$	Ads	1	0	0
2	$N+(s) \leftrightarrow N(s)$	Ads	1	0	0
3	$2O(s) \leftrightarrow O_2+2(s)$	Arrh	$3.58x10^{10}$	1	256.07
4	$O_2+(s) \leftrightarrow O+O(s)$	E-R	1	0	118.06
5	$CO_2+(s) \leftrightarrow CO+O(s)$	E-R	0.9	0	0
6	$O(s)+C(b) \leftrightarrow CO+(s)$	Arrh	$2.08X10^{9}$	1	332.56
7	$O+O(s)+C(b) \leftrightarrow CO_2+(s)$	E-R	0.8	0	16.63
8	$2O(s)+C(b) \leftrightarrow CO_2+(s)$	Arrh	$3.58x10^{14}$	1	332.56
9	$C+(s) \leftrightarrow (s)+C(b)$	E-R	0.24	0	0
10	$C_2+2(s) \leftrightarrow 2(s)+2C(b)$	E-R	0.5	0	0
11	$C_3+3(s) \leftrightarrow 3(s)+3C(b)$	E-R	0.023	0	0
12	$N_2+(s) \leftrightarrow N+N(s)$	E-R	1	0	636.85
1b	$O+(s) \leftrightarrow O(s)$	des	$1.72x10^{4}$	0	374.13
2b	$N+(s) \leftrightarrow N(s)$	des	$1.72x10^{4}$	0	304.29

Table 3.5. ZA model with nitridation (Alba) [15]

	reaction	*type*	$\gamma or A$	β	E ($\frac{kJ}{gmol}$)
1	$N+(s)+C(b) \leftrightarrow CN+(s)$	ER	0.36	0	36.86
2	$N(s)+C(b) \leftrightarrow CN+(s)$	Arrh	0.57	1	69.46

Table 3.6. MURI model [16]

	reaction	rate	rate constant (k)	units
1	$O+(s) \rightarrow O(s)$	$k_1[O][s]$	$\frac{1}{4B}\sqrt{\frac{8k_bT}{\pi m_o}}$	$m^3mol^{-1}s{-}1$
2	$O(s) \rightarrow O+(s)$	$k_2[O(s)]$	$\frac{2\pi m_o k_b^2 T^2}{Bh^3}\exp\frac{-44.277}{T}$	s^{-1}
3	$O+O(s)+C(b) \rightarrow CO+O(s)$	$k_3[O][O(s)]$	$\frac{1}{4B}\sqrt{\frac{8k_bT}{\pi m_o}}57.37\exp\frac{-46.67}{T}$	$m^3mol^{-1}s^{-1}$
4	$O+O(s)+C(b) \rightarrow CO_2+(s)$	$k_4[O][O(s)]$	$\frac{1}{4B}\sqrt{\frac{8k_bT}{\pi m_o}}8.529x10^{-6}\exp\frac{6958}{T}$	$m^3mol^{-1}s^{-1}$
5	$O+C(b)+(s) \rightarrow CO+(s)$	$k_5[O][(s)]$	$\frac{1}{4B}\sqrt{\frac{8k_bT}{\pi m_o}}0.1203\exp\frac{2287}{T}$	$m^3mol^{-1}s^{-1}$

4. Methodology

The general method used for this study was to produce a high fidelity hypersonic flow over a simple sharp and a 12.7mm nose-radius, 10 degree half-angle cone with a length of 3 meters. The grids were designed to capture the high gradients within the boundary layer. An 11-species finite-rate gas chemistry model was used for the mean flow, which included N_2, O_2, NO, CO, CO_2, C_2, C_3, C, N and O where the gas reactions rates were determined by Park [31, 77, 78]. This gas model allowed for the gas phase reactions with air species as well as gas phase interactions with the ablative species as diffusion occurred. The chemical reactions considered in the model for the gas phase include dissociation and exchange reactions. The boundary conditions at the surface were determined by the choice of gas-surface reaction model at a defined wall temperature. A data file defining surface temperature values at defined x-locations along the body was used as the surface temperature boundary conditions. Between the defined locations, the temperature was extrapolated in a decreasing linear function, creating a step-wise defined function with no discontinuities. These flow results were then used as input to an LST analysis. The frequencies for the LST input were chosen based on Equation 2.7. The body location values for the LST were designed to match the stability grid to the computational grid to limit interpolation errors.

4.1 Grids

The grids used were structured, axi-symmetric grids of a simple 10 degree half-angle cone, with cells clustered at the surface and rotated through 10 degrees. The nosetip consisted of either a sharp nose or 12.7 mm nose radius and the total cone length was 3 meters. Figures 4.1 and 4.2 show the grid outline with Figure 4.3

highlighting the clustering at the nose tip of the blunt cone. Over 100 cells were clustered in the boundary layer to ensure a y+ value of 1 or less along the entire length of the cone. Initially, the grid was modeled with and without a wake to ensure that modeling the flow without the expansion at the end of the vehicle did not significantly affect the flow properties or the stability characteristics. The deletion of the wake from the grid saved approximately 25% in total cell count. Figure 4.4 shows the results for pressure at the end of the cone and Figure 4.5 shows the pressure in the boundary layer. The maximum percent difference in the pressure for the flow with and without a wake is 5.2%, highlighted in the circled areas in Figure 4.4. Within the boundary layer, the maximum percent difference is 0.5%. Given the small error in the results with a significant saving in computation, the no-wake grid was used for the study. Similar simplifications to the computational domain by not modeling the wake were employed by Jewell and Wagnild in their computational studies of the CO_2 wind tunnel results [105, 51].

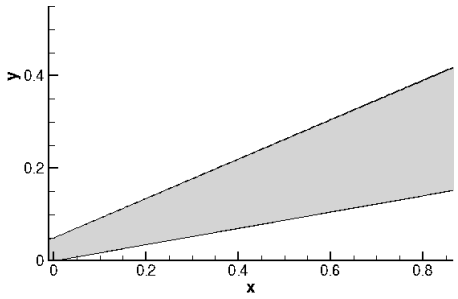

Figure 4.1. Wire diagram of the sharp cone grid used

A convergence study was completed to ensure accurate, grid-independent solutions while minimizing computational effort. High resolution of the flow was desired in the boundary layer of the solution and points were distributed to cluster within this layer. The flow for the convergence study was run with an adiabatic, non-reacting wall with a 7-species gas phase model. Figure 4.6 shows the results from the convergence study. Due to the similar results shown in the three finest grids, grid 3 was originally

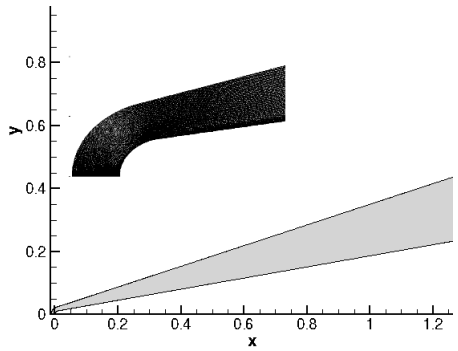

Figure 4.2. Wire diagram of the blunted cone grid

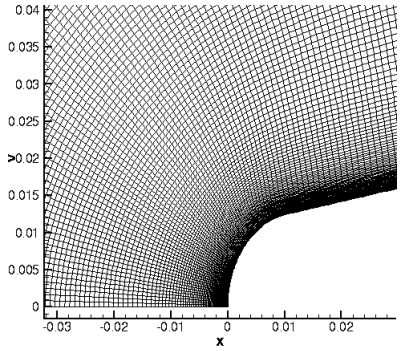

Figure 4.3. Grid detail at the blunted nosetip showing surface clustering

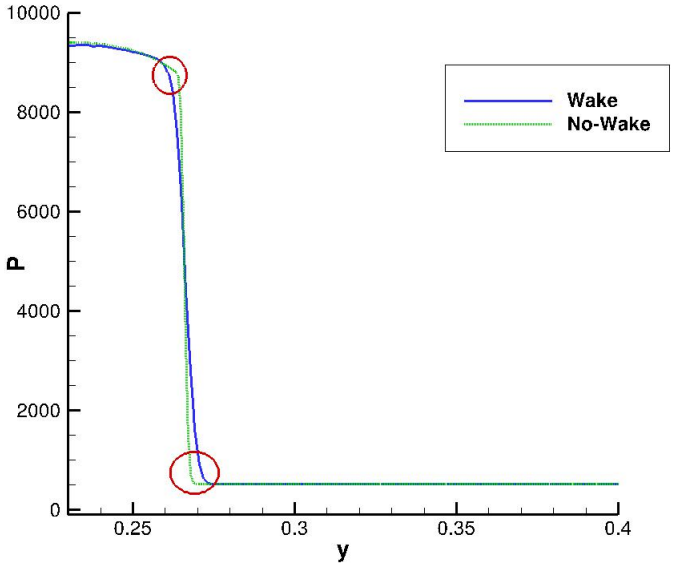

Figure 4.4. Pressure at x=1.24m highlighting variations cause by including the wake

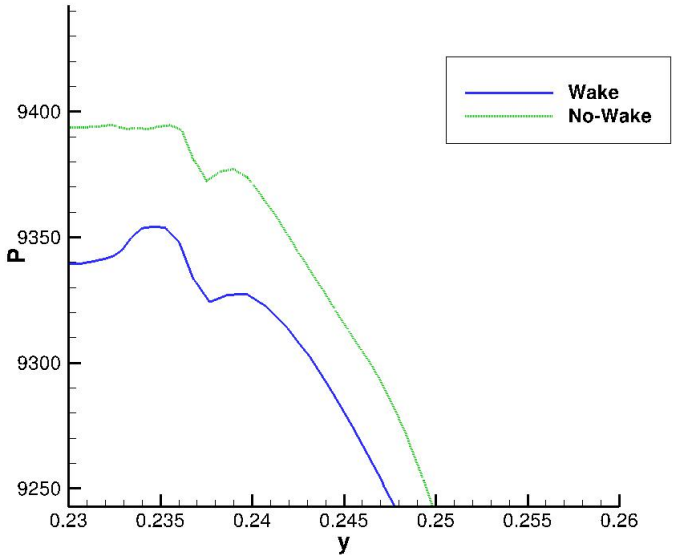

Figure 4.5. Pressure within the boundary layer at x=1.25m with and without a wake

selected and being grid independent, for a total grid size of nearly 240,000 cells. However, the grid was later expanded to use 360 cells in the body normal direction (with 110 cells remaining cluster in the boundary layer) and 300 cells per meter in the streamwise direction, for a total grid size of 324,000 cells. These dimensions allowed for greater agreement between the sharp and the blunt cone grids from the tangent point back along the body. Also, this additional refinement allowed for greater agreement between the computational and stability grids from the tangent point back and the higher number of cells in the nosetip region reduced the stability error caused by the higher gradients in this region on the blunt cone. Matching the stability and computational grids reduced errors in the stability analysis that arose from the polynomial interpolation of the computational grid onto the stability grid.

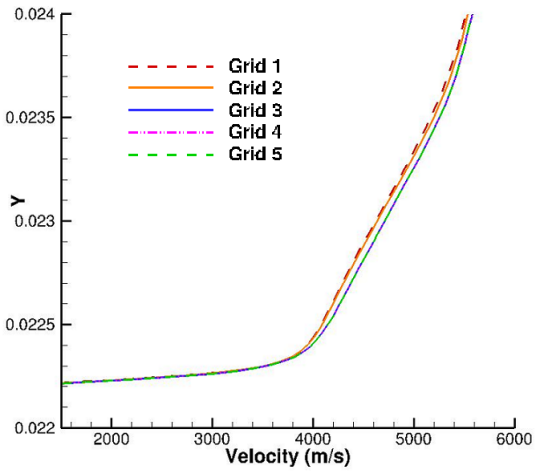

Figure 4.6. Convergence study results

4.2 US3D

The US3D code was used to solve the flow field for all the simulations. US3D[30] was originally developed as an unstructured follow-on to the NASA Data Parallel Line Relaxation (DPLR)[30] code and has been validated on a wide-range of high-speed test cases and experimental data. The solver uses a finite-volume formulation of the compressible Navier-Stokes equations with selectable switches to include finite-rate internal energy excitation and chemical kinetics [106]. The modified Steger-Warming flux vector splitting method was used to calculate the convective fluxes, with a Monotonic Upwind Scheme for Conservation Laws (MUSCL) scheme for second order accuracy. A weighted least-squares reconstruction of the primitive variables is used to calculate cell-centered gradients. The DPLR time integration method was used to speed up simulation convergence [30]. The US3D code has the ability to include user programmed subroutines to allow for modification to the base code. To conduct an analysis using the different ablation models discussed in Chapter 3, a user-defined set of subroutines was used. These routines read in an user-defined surface temperature model (described above) which were held constant for each flow

condition. The user-defined gas-surface interaction subroutine used this temperature profile as the input value for the chosen model. This routine determined the surface boundary conditions for the species production.

An input file was used to specify the choices for specific parameters, such as the number of relaxation iterations or whether the flow is laminar or turbulent. For chemically reacting and activation of vibrational energy the user has a choice of energy modeling, viscosity models, and molecular diffusion models. The flow was assumed viscous and laminar with both chemical reactions and vibrational energy relaxation activated. The vibrational-electronic energy modeling used the NASA Lewis data with a Blottner viscosity model [107] using Wilke's mixing rule [108] and diffusion coefficient derived from a constant Lewis number. The relaxation constants were from Park and Millikan [77, 31, 82] except for the CO_2 constants which came from Camac [26]

4.3 STABL3D

Stability and Transition Analysis for hypersonic Boundary Layers (STABL3D) code was developed to use the flow solution from US3D to calculate the linear stability of the boundary layer [33]. The code takes a streamline solution from a user defined starting point from the US3D mean flow solution and calculates the boundary layer characteristics along that streamline. The flow characteristics are then used to solve the linear stability equations at user specified frequencies and locations along the body. The streamline starting position for the analyses was chosen past the tangent point and expanded in both directions. The flow solutions were all run assuming 2-dimensional flow with no crossflow instabilities, a valid assumption based on the geometry used. These results are then used to produce a stability diagram and a

maximum N factor envelope plot along the body to show the maximum amount of amplification in the boundary layer and the frequencies where there is amplification.

4.4 CO_2 Concentration Study

The concentration study was conducted using a freestream gas composition of the specified CO_2 concentration (between 50% and 2.5%) and the N_2 and O_2 concentrations as found in air. To ensure a constant CO_2 concentration in the boundary layer, dissociation of CO_2 across the shock and in the high temperature gas regions was not modeled in the gas file. There were no gas-surface interactions used during this phase of the research and the wall temperature was set to isothermal wall (to match experimental conditions) at 298.3K. First, the model was validated using two experimental test runs, one with high enthalpy flow and one with lower enthalpy flow, taken from Jewell [17] and the stability results were compared. These results were run on a sharp 5 degree half-angle cone to match experimental models and were used only to validate the methodology. Using the experimental freestream parameters for both the high and low enthalpy cases, a sharp 10 degree half-angle cone model was used and the concentration of CO_2 in the freestream was reduced from 50% in 10% increments until the change in transition location due to CO_2 damping was considered marginal. The same flow conditions were then run on the blunt cone from 50% to 2.5% to examine the effects of nose bluntness on the CO_2 damping effects. The freestream flow parameters were then changed to model flight-representative quantities while matching the experimental enthalpy or boundary layer maximum temperature. An LST analysis was done on each flow result for the vibrational modes active and inactive to determine the amount of damping provided by the chemical composition of the boundary layer.

4.5 Model Comparison and Parameter Study

For the gas-surface interaction model comparison phase of the research, the freestream gas composition was air and the freestream state variables were determined from the 1976 Standard Atmosphere Tables [2]. The surface temperature was determined using an non-ablative flow simulation with an adiabatic wall boundary condition. In conditions where the wall temperature from these simulations was too high (i.e. where the wall temperature was significantly higher than sublimation temperature of graphite, approximately 3800-4200K [109]) the wall temperature was reduced to 4000K. The flight conditions chosen for the study were a re-entry type altitude and a high density altitude condition, at both relatively low and high enthalpies, with a freestream velocity of 3000 $\frac{m}{s}$ and 6000 $\frac{m}{s}$, respectively.

Simulations were run on both the sharp and blunt cones at each flight condition using each of the six ablation models as well as a control flow that had no ablation. An LST analysis allowing full chemical and vibrational modes was conducted on each simulation result comparing the effects of each ablation model and the subsequent chemical species concentrations on the stability of the boundary layer. Those flows which contained significant amounts of CO_2 in the flow, as determined by the CO_2 concentration study, were also analyzed with vibrational modes disabled to investigate the CO_2 damping effects.

Parametric studies to determine the sensitivity of the air-carbon gas-surface ablation model and the boundary layer stability on altitude, wall temperature and site density. An altitude analysis was conducted examining the differences in the CO_2 production through various points of a simulated reentry trajectory. The stability results from the Park, modified ZA and the MURI models were also analyzed to relate the subsequent effects on the boundary layer stability. The altitude was varied in $10,000$ ft altitude increments, with the freestream temperature and pressure

determined from the 1976 Standard Atmosphere Tables [2] at a freestream velocity relevant to a standard reentry trajectory. The effects of increasing density would increase the amount of CO_2 produced, assuming non-saturation of the site density, and decrease the boundary layer thickness changing the receptivity to second mode frequencies. To determine the effect of wall temperature on the production of CO_2 from the ablation models and the subsequent effect on stability, the wall temperature used was increased, or decreased, by a given factor from the original adiabatic temperature distribution, maintaining a maximum temperature of approximately 4000K for the sublimation of graphite. The Park, modified ZA and the MURI models were used for this parameter study. Finally, the effect of site density was examined by varying the site density parameter from the base value of for graphite.

5. CO_2 Concentration Results

5.1 Model Validation Results

To validate the methodology for the concentration study, the simulation and stability results were compared to experiments conducted in GALCIT T5 wind tunnel by Jewell [17]. His work consisted of multiple wind tunnel experiments measuring transition using a sharp, 5 degree half-angle cone in air, N_2 , 100% CO_2 or 50% CO_2/air mixtures. Two specific test runs were chosen with a 50% CO_2/air mixture at a high and low enthalpy as the validation cases. Tables 5.1 through 5.3 show the freestream wind tunnel conditions, air composition and transition characteristics computed [17].

Table 5.1. Test case freestream conditions [17]

shot	T_w K	h_{res} $\frac{MJ}{kg}$	ρ_∞ $\frac{kg}{m^3}$	T K	T_v K	V_∞ $\frac{m}{s}$
2729	298.0	8.45	0.12	1572.3	1573.1	3426
2813	298.0	5.12	0.06	862.1	965.8	2783

Table 5.2. Test case freestream air composition by mole fraction [17]

shot	N_2	O_2	CO_2	NO	CO	N	O
2729	0.361	0.139	0.362	0.0474	0.0881	0	$2.1x10^{-3}$
2813	0.365	0.118	0.440	0.038	0.0377	0	$2.58x10^{-4}$

Table 5.3. Test case transition characteristics [17]

shot	x_{tr}	N_{tr}	$N_{trNoVib}$
2729	0.758	10.32	19.94
2813	0.605	9.06	11.34

The freestream conditions were used in US3D as the input conditions and a linear stability analysis was done with and without vibration enabled. The high enthalpy

validation results are shown in Figures 5.1a and 5.1b and the maximum N factors for the high enthalpy flow shown in Figure 5.2. The results show N factor values at $x = 0.758$, the location of transition in the experiments, of 10.18 and 19.64, for vibrational modes enabled and disabled, respectively. These results are within 1% of those originally calculated by Jewell for the high enthalpy cases [17]. Similar results were seen in the lower enthalpy case, shot 2813 (Figures 5.3a through 5.4). At a experimental transition location of $x = 0.605$, the vibrational and non-vibrational N factors were 8.89 and 11.29, respectively, within 2% of the results calculated by Jewell [17].

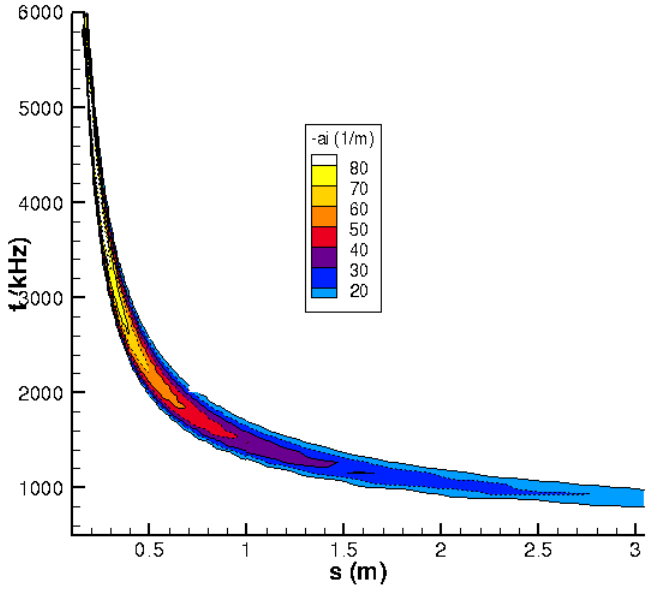

(a) Stability diagram with vibration enabled

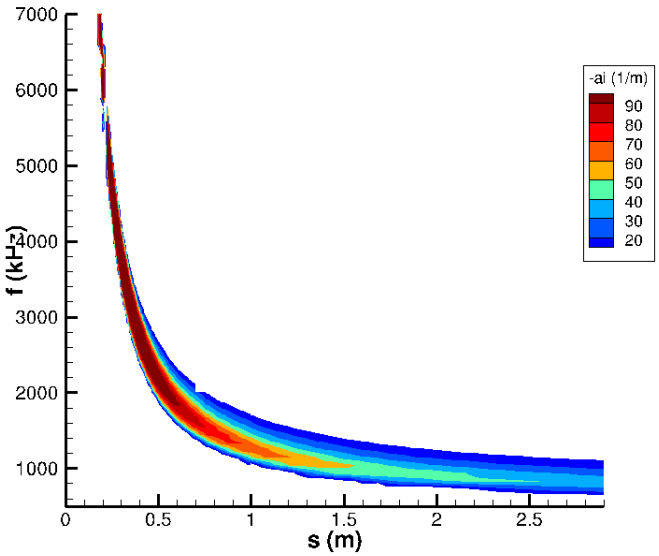

(b) Stability diagram with vibration disabled

Figure 5.1. Stability diagram for for high enthalpy test case, $8.45\frac{MJ}{kg}$, with vibration enabled and disabled

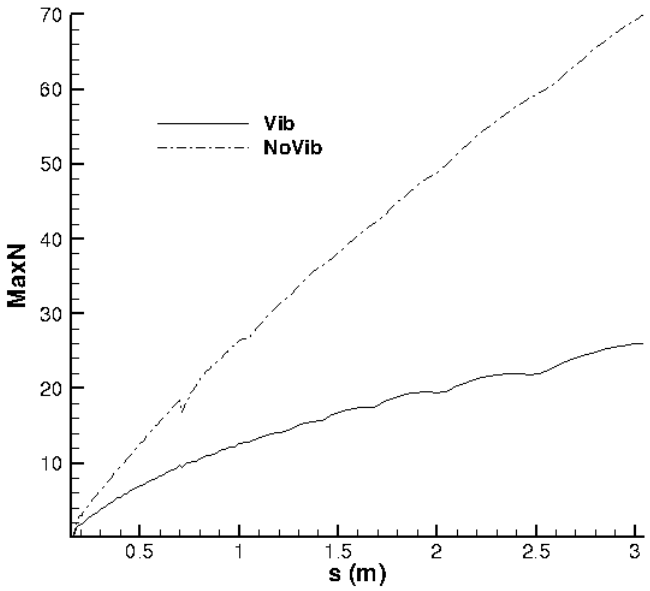

Figure 5.2. Maximum N factors for high enthalpy test case, $8.45\frac{MJ}{kg}$ (non-vibrational results represented with a dashed line)

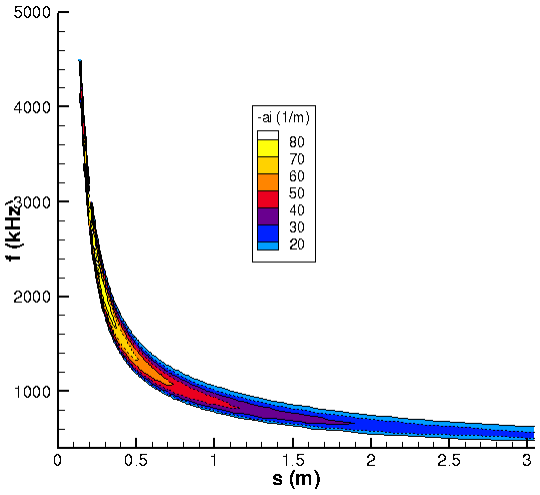

(a) Stability Diagram with vibration enabled

Figure 5.3. Stability Diagram for low enthalpy, $5.12\frac{MJ}{kg}$ with vibration enabled and disabled

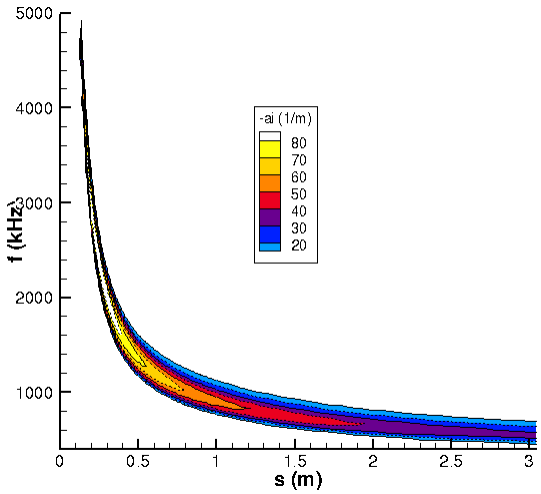

(b) Stability Diagram with vibration disabled

Figure 5.3. Stability Diagram for low enthalpy, $5.12\frac{MJ}{kg}$ with vibration disabled

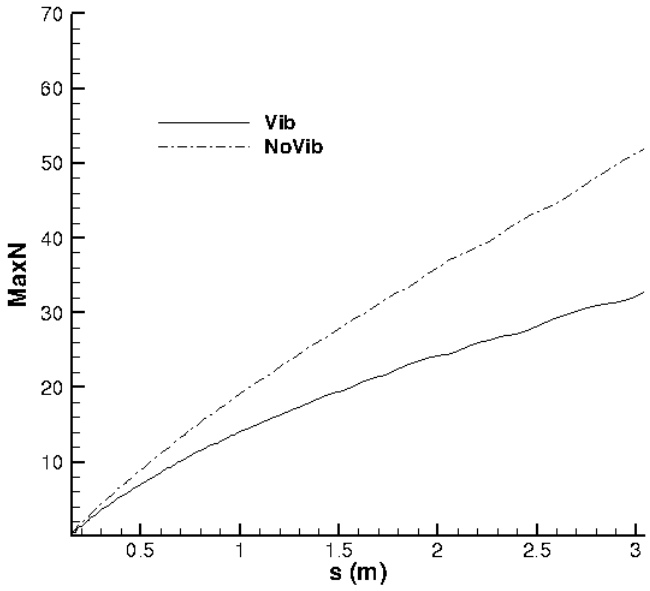

Figure 5.4. Maximum N factors for high enthalpy test case (non-vibrational results represented with a dashed line)

Given the low error between the two studies, the methodology was shown to be valid. A 10 degree half-angle cone with both a sharp and 12.7 mm nose radius blunt cone was used for the remainder of the concentration study. The grid dimensions for the 10 degree half-cone angle grid was equal to those used for the validation study grid.

5.2 High Enthalpy Freestream Conditions

Using the freestream conditions for the high enthalpy test case, a series of flow simulations were conducted using decreasing concentrations of CO_2. CO_2 was not allowed to dissociate across the shock to maintain a constant concentration of CO_2 in the boundary layer and the only gas reaction allowed that would change the concentration of CO_2 in the gas was the exchange between CO and O_2, which did not change the concentration by more then 0.4% in the boundary layer.

5.2.1 Wind Tunnel Conditions.

Figure 5.6 shows the N factor comparisons of the varying CO_2 concentrations over a sharp cone. Higher concentrations of CO_2 produce less total amplification, showing vibrational damping. However, highlighting the graph at x=0.3 and below, there appears to be a slight reversal in the effects of CO_2 concentrations, as it appears that the lower concentrations produce lower N factors. This result is caused by numerical error at the nosetip of the sharp cone due to the grid rather than a physical result. The grid was designed with a small number of cells to allow the simulation start prior to encountering the cone, allowing for a larger initial time step to be taken at the start of the simulation. While the grid is highly resolved in the body normal direction, the streamwise resolution is low in this area and these cells are very narrow, long cells. As the concentration of CO_2 changes, the c_p value of the

freestream also varies and at the inflow region of the grid, the flow become very sensitive to these variations due to the high gradients, especially near the shock. Examining this numerical error closely, as the concentration of CO_2 decreases, the shock actually becomes "detached", effectively producing a small blunted nose-type effect and introducing an entropy layer. For the CO_2 values used in these simulations, the "equivalent nose radius", determined using Rotta's method, was determined to be approximately 5 mm at 10% concentration and decreased with increasing CO_2 concentrations. Figure 5.5 shows the shock contour at each CO_2 concentration. At 50% CO_2 the shock contour is sharp and resembles an oblique shock. However, at 10% CO_2, there is a clear curvature to the shock caused by the lower streamwise resolution which, for the flow, resembles a nose bluntness. This effect is evident in the increasing x location where the instabilities start amplifying as the concentration decreases. For the 50% flow, amplification begins right at the nose of the cone, while the 10% doesn't show any amplification until x=0.05 m, giving the appearance lower amplification despite the higher rate of amplification indicated by the slope of the line. This numerical error, however, does not impact the conclusions of this study as the comparisons are only made between the vibrational and non-vibrational results at each concentration, rather than between concentrations. The total change in the amplification start point is less than 0.05 m at the high enthalpy conditions (see Figure 5.6) between all concentration levels. The starting streamwise location of amplification is the same when the concentration is constant whether vibration is enabled or disabled and so has no impact when comparing these two stability results.

Comparing the stability results with and without vibration, the effects of CO_2 damping becomes evident at the high enthalpy flow conditions. Figure 5.7 shows the resulting N factors with and without vibration enabled, where the dashed line represent the stability results without vibration. Based on empirical data, flight

transition occurs between N factors of 8.5 and 14 [51], so for this study transition is assumed to occur at an N factor of 10 and Table 5.4 shows the changes in the transition location for the various concentrations. For the high enthalpy flow, a minimum concentration of just greater than 10% CO_2 is necessary to change the transition location by at least 10 cm on a sharp cone. These results are similar to what was seen in the T5 wind tunnel experiments [7, 25, 17].

Table 5.4. High enthalpy transition location changes on the sharp cone

Concentration	x_{tr}	$x_{trNoVib}$	δx_{tr}
50%	0.8323	0.3782	0.4541
40%	0.7630	0.4039	0.3591
30%	0.6959	0.4291	0.2668
20%	0.6348	0.4596	0.1752
10%	0.5750	0.4902	0.0848

Figure 5.8 shows the N factors results of the blunt cone at varying concentrations of CO_2, where the dashed lines represent non-vibrational results. Of note, for the sharp cone models, the amplification starts at the same location regardless of vibrational excitation being enable or disabled. This is not the case for the blunt cone model. The differences in the starting location of the amplification without vibration enabled on the blunt cones, are due to the entropy layer [43]. The existence of the entropy layer is the cause of the large increase in the streamwise location first indicating the start of amplification on the blunt cone compared to the sharp cone as the entropy layer has a stabilizing effect on the second mode instability. The small changes in the start of amplification over the blunt cone model are due to the changing value of c_p in each flow due to the differing freestream gas composition which changes the shock standoff distance and the shock shape. The trend shown in the data is increasing CO_2 concentration slightly decreases the detached shock distance, thus decreasing the thickness of the entropy layer and the entropy layer swallowing distance, where

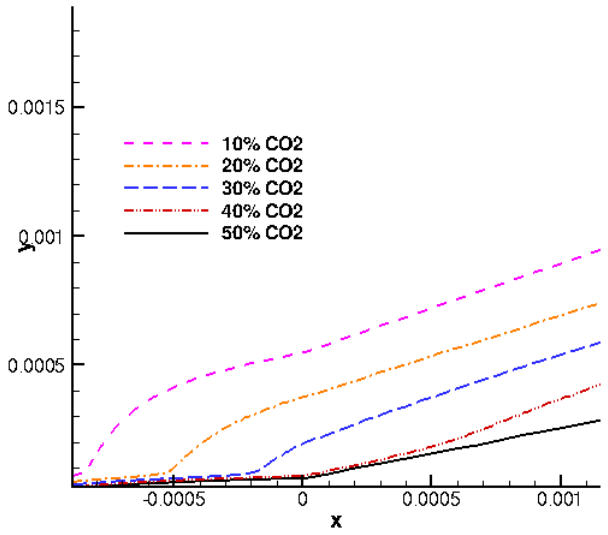

Figure 5.5. Numerical error near the sharp tip due to high cell aspect ratio

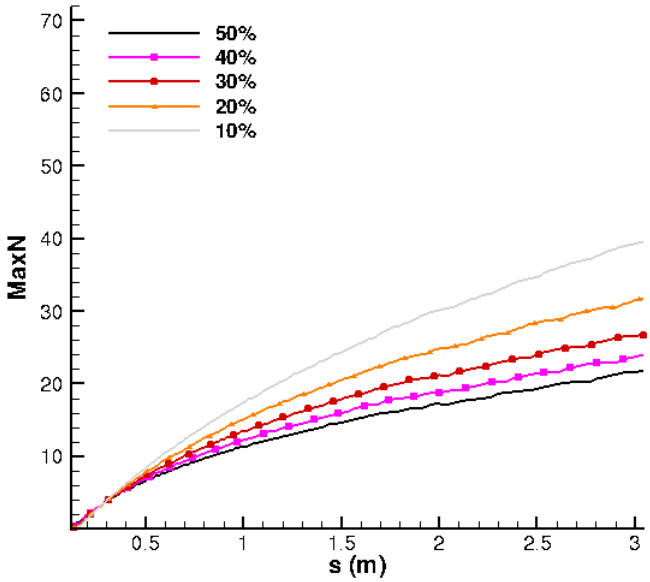

Figure 5.6. N factors for sharp cone with varying CO_2 concentrations at high enthalpy, $8.45\frac{MJ}{kg}$

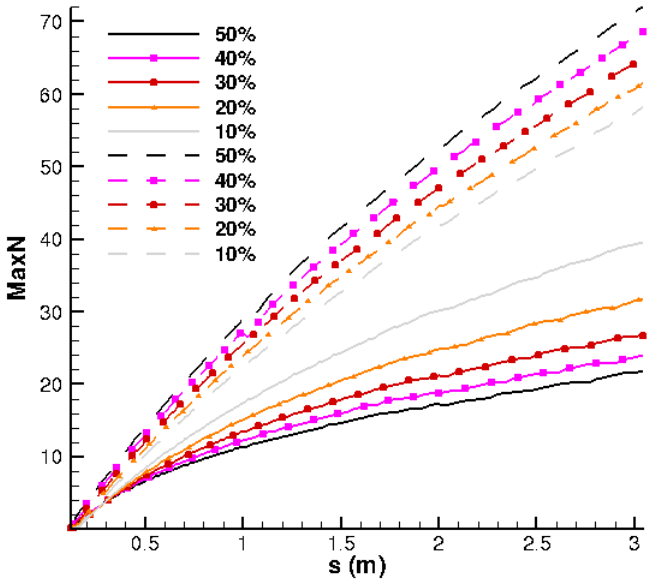

Figure 5.7. N factors for sharp cone with varying CO_2 concentrations with and without vibration at high enthalpy conditions (solid lines: vibrational effects, dashed lines: no vibrational effects)

the entropy layer is entrained into the boundary layer [4]. These small changes move the start of amplification forward in the streamwise direction as is shown when vibration is disabled. However, the results with vibration enabled show a reversal in this trend: increasing CO_2 concentration increases the streamwise location for the start of amplification. This reversal highlights the damping effect of CO_2 on the boundary layer stability. There is a significant difference in the streamwise location of the start of amplification between the 10% and 50% concentration results when vibration enabled.

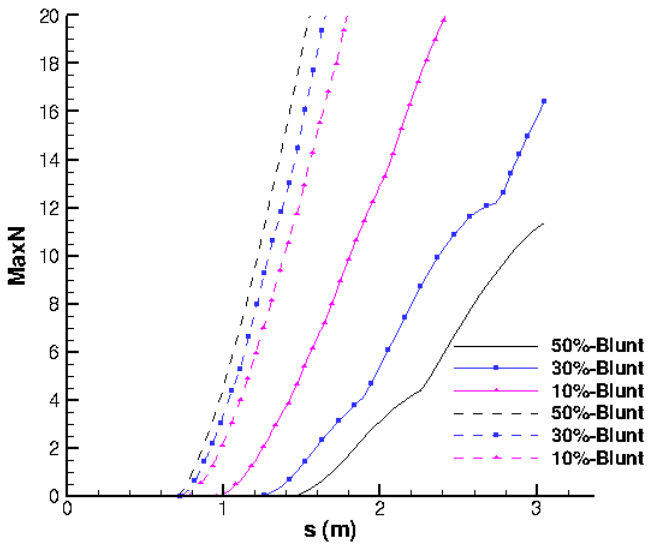

Figure 5.8. N factors for blunt cone with varying CO_2 concentrations at high enthalpy, $8.45\frac{MJ}{kg}$ (solid lines: vibrational effects, dashed lines: no vibrational effects)

Table 5.5 shows the change in streamwise location for transition on the blunt cone model. For the same concentration of CO_2 there is a marked increase in the change in transition location for a blunt cone compared to a sharp cone, indicating a greater damping effect on the blunt cone model than a sharp cone for the same freestream conditions. Examining the boundary flow conditions, the temperature and velocity profiles differ between the two boundary layers. The blunt cone has a thicker velocity and thermal boundary layer and a higher temperature in the boundary layer (see Figures 5.9 and 5.10).

Table 5.5. High enthalpy transition location changes on the blunt cone

Concentration	x_{tr}	$x_{trNoVib}$	δx_{tr}
50%	2.8265	1.2165	1.610
30%	2.3734	1.2906	1.0828
10%	1.8062	1.3464	0.4198
5%	1.659	1.420	0.239
2.5%	1.539	1.437	0.102

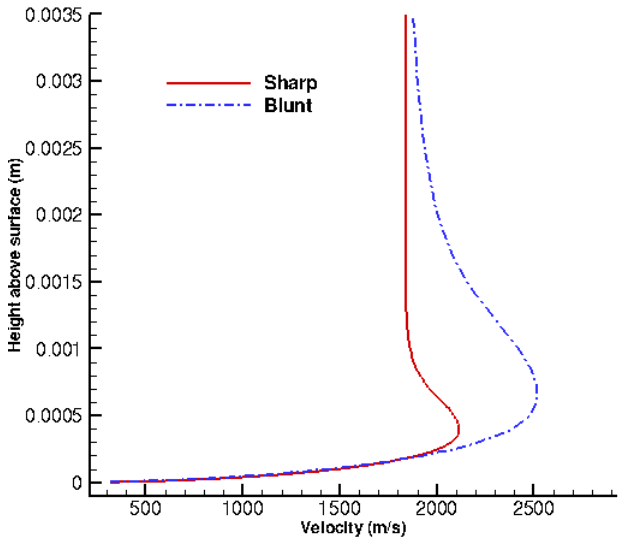

Figure 5.9. Temperature profile in the boundary layer at x=1.0 m for the blunt and sharp cones

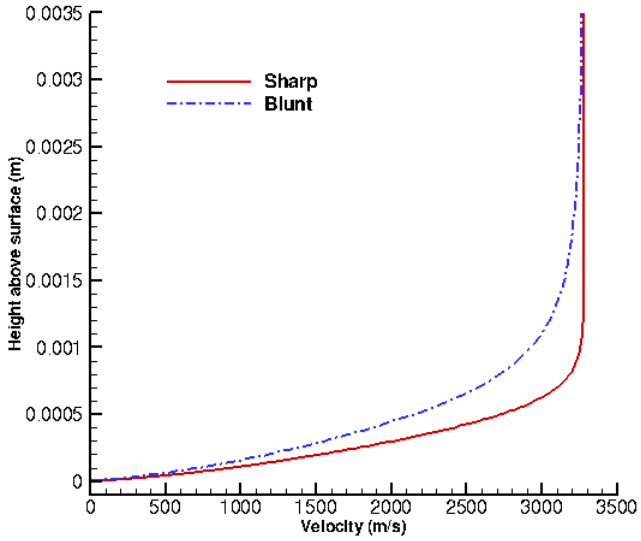

Figure 5.10. Velocity profile in the boundary layer at x=1.0 m for the blunt and sharp cones

Figures 5.11a through 5.11c compare the results of the sharp and blunt cones at 50%, 30% and 10% CO_2 concentrations at the higher enthalpy flow. For the sharp cone, the start of amplification for both the vibrational and non-vibrational simulations are the same, while there is a significant difference for the blunt cone simulations. As the concentration of CO_2 increases, the location of the start of amplification continues to moves downstream in the streamwise direction. At 50% concentration of CO_2, amplification starts at approximately 1.5 m along the body, but this value is decreased to 1.0 m for a 10% concentration. At 50% concentration of CO_2, the change in start of amplification between the vibrational and non-vibrational stability analysis shows as 0.7 m change, which is reduced to only 0.14 m for the flow with 10% concentration. Again, the increased temperature of the boundary layer for the blunt compared to the sharp cone allows for this increased CO_2 damping to occur. Figures 5.12a and 5.12 show the temperature contours in the boundary layer for the sharp and blunt cones. The blunt cone has both a thicker thermal boundary layer and higher temperatures.

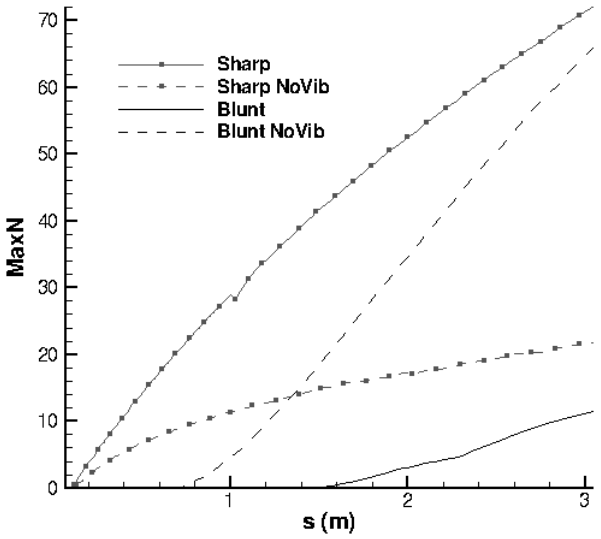

(a) N factors for 50% CO_2 concentration

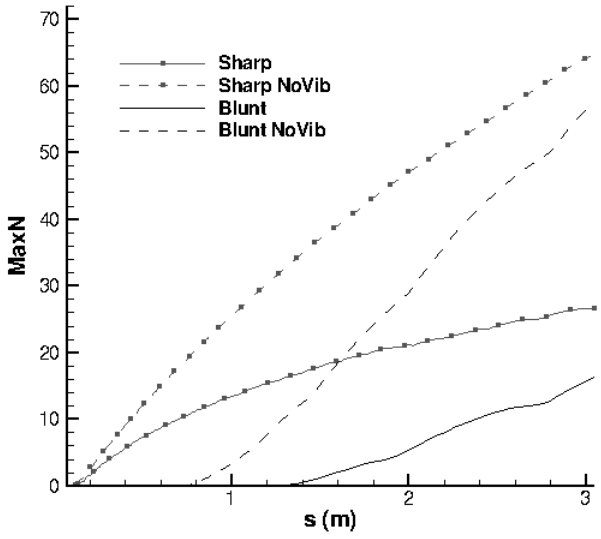

(b) N factors for 30% CO_2 concentration

Figure 5.11. N factors for CO_2 concentrations with and without vibration for the sharp and blunt cone at high enthalpy, $8.45\frac{MJ}{kg}$ (solid lines: vibrational effects, dashed lines: no vibrational effects)

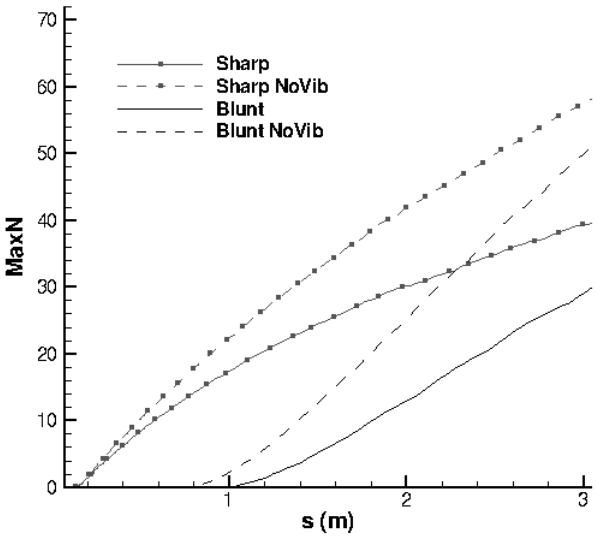

(c) N factors for 10% CO_2 concentration

Figure 5.11. N factors for CO_2 concentrations with and without vibration for the sharp and blunt cone at high enthalpy, $8.45\frac{MJ}{kg}$ (solid lines: vibrational effects, dashed lines: no vibrational effects)

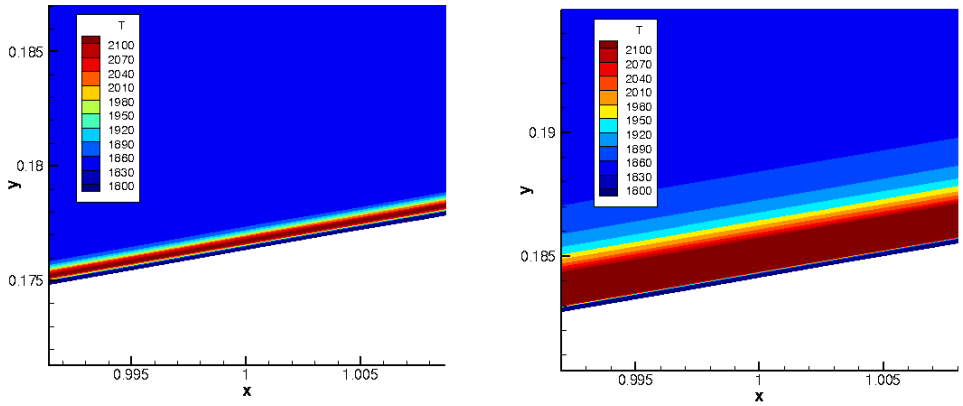

(a) Contour plot of temperature in the boundary layer for sharp cone

(b) Contour plot for temperature in the boundary layer on blunt cone

Figure 5.12. Temperature contours in the boundary layer on blunt and sharp cone at high enthalpy, $8.45\frac{MJ}{kg}$

5.2.2 Equivalent Flight Representative Freestream Conditions.

In order to achieve high enthalpy flow conditions in the T5wind tunnel, the freestream temperature is increased to higher than standard atmospheric values (see Table 5.1). However, this increased temperature is not representative of flight conditions, where the freestream temperature varies only slightly from standard atmospheric conditions and higher enthalpy is achieved through increased velocity [2]. The freestream flow parameters were modified to maintain the freestream total enthalpy but match flight representative parameters (freestream values of density of $2.371x10^{-1}\frac{kg}{m^3}$, T and T_v of 216.2 K, and velocity of 4000 $\frac{m}{s}$). When the wind tunnel condition simulations at 10% CO_2 concentrations were compared with those with the flight representative conditions, a significant change in stability results were seen. Figure 5.14 shows an N factor comparison over the sharp cone, with vibrational enabled and disabled, for matching enthalpy conditions. There is a significant increase in the amplification seen with significantly higher N factors. This increase is due mainly to the increase in the Reynolds number of the flow, with the wind tunnel Reynolds number being $6.1x10^6$ and the flight values being $5.8x10^7$. However, comparing the impact on the transition location, the results are very similar, with the wind tunnel delaying transition approximately 8 cm, while the flight representative cases delayed transition 6.4 cm. Examination of the temperature profiles of the boundary layer between these two flows shows that the maximum temperature in the flight representative boundary layer is significantly less than the wind tunnel (see Figure 5.17).

The flight conditions were changed such that the boundary layer maximum temperature matched ($2.371 \times 10^{-2}\frac{kg}{m^3}$, T and T_v of 216.2 K, and freestream velocity of 4500 $\frac{m}{s}$ with a freestream enthalpy of $9.7\frac{MJ}{kg}$) while maintaining a 10% CO_2 concentration in the boundary layer. Comparing the results at these new conditions shows that even when the maximum temperatures in the boundary layers match, the

flight still produces significantly higher N factors when compared to the wind tunnel simulations, again due to the Reynolds number being $6.5x10^7$, 10 times higher than the wind tunnel flow. Figure 5.14 compares the stability analysis results of these two flow conditions, with and without vibration enabled. For this condition, the total delay in transition location was 8.2 cm, similar to the wind tunnel case. Examining the results of these three simulations (Figure 5.15) shows that, while the flight representative simulations vary only slightly from each other despite the temperature differences they vary greatly from the N factors for the wind tunnel case. Figure 5.17 shows the boundary layer temperature profiles for all three cases. The temperature gradient between the tunnel and flight simulations when the total enthalpy is matched are similar up to the maximum temperature. The flight representative case, however, quickly decreases back to the freestream temperature of 216.2 K at an equally high gradient, while the simulations using the wind tunnel conditions continues to increase in temperature (at the same rate) reaching a 400 K higher temperature before slowly decreasing to 1573 K, the free stream temperature. The higher freestream temperature for the wind tunnel conditions increases the total thermal boundary layer thickness, but also maintains a higher temperature throughout more of the boundary layer. When the maximum boundary layer temperature is matched, while the initial gradients are higher than the wind tunnel case, a similar difference in the thermal boundary layer thickness and higher temperature profile is seen. The higher sustained temperatures with the wind tunnel conditions may allow for the slightly greater CO_2 damping effects despite the lower total amplification. Comparing the results of flight versus wind tunnel results removing that Reynolds number effects show a similar overall damping effect, though the wind tunnel results still shows a slightly higher damping effects (see Figure 5.16).

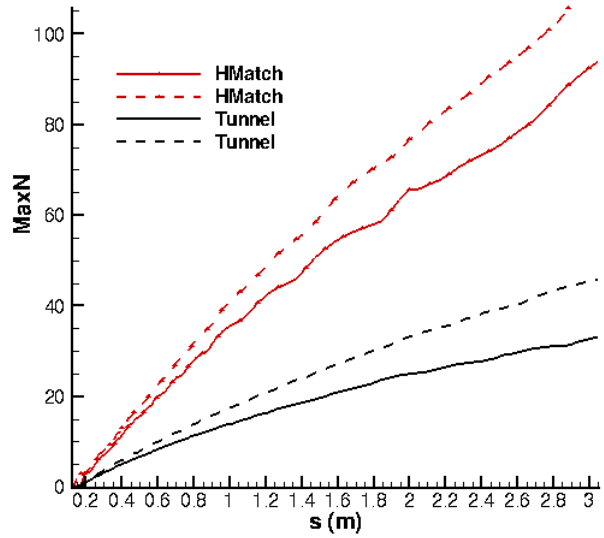

Figure 5.13. N factors for matching enthalpy between wind tunnel and flight representative conditions (solid lines: vibrational effects, dashed lines: no vibrational effects)

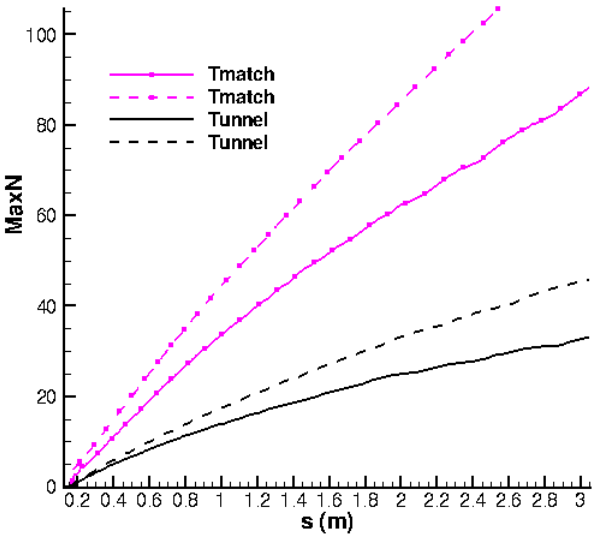

Figure 5.14. N factors for matching maximum boundary layer temperatures between wind tunnel and flight representative conditions (solid lines: vibrational effects, dashed lines: no vibrational effects)

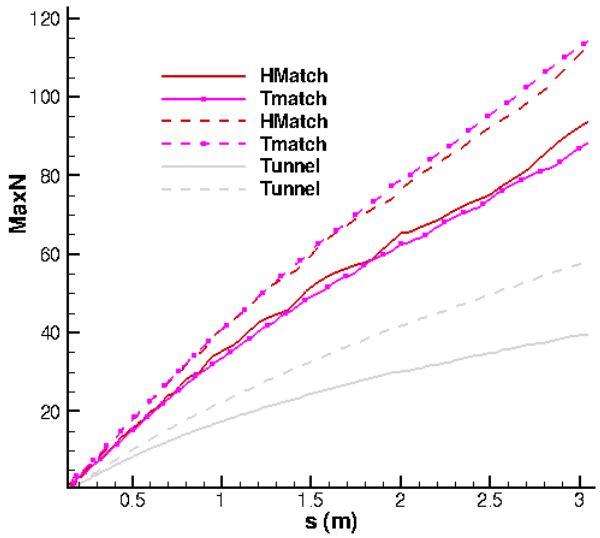

Figure 5.15. N factors for wind tunnel and flight representative conditions (solid lines: vibrational effects, dashed lines: no vibrational effects)

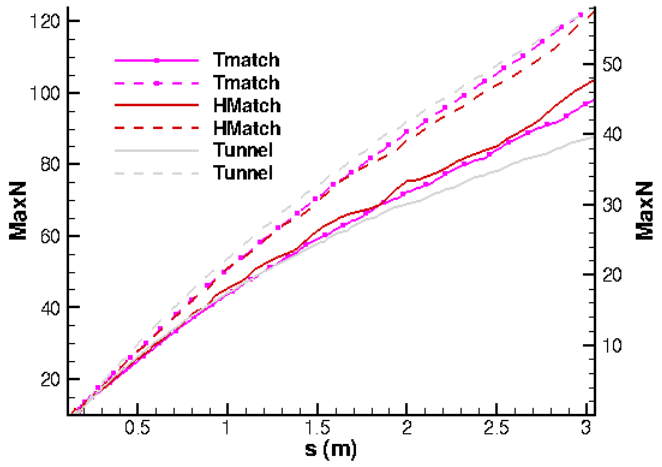

Figure 5.16. N factors for wind tunnel and flight representative conditions compared without Reynolds number effects (solid lines: vibrational effects, dashed lines: no vibrational effects)

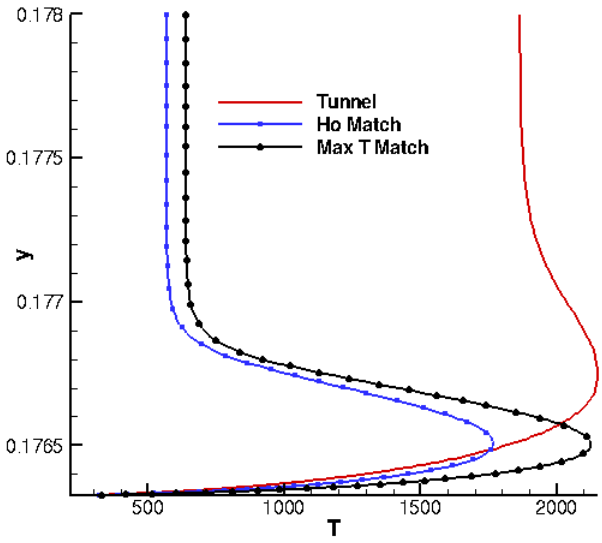

Figure 5.17. Temperature profile for x=1.0 m for T5 wind tunnel and flight representative conditions

5.3 Low Enthalpy Freestream Conditions

Using the freestream conditions for shot 2813, the low enthalpy flow at $5.12\frac{MJ}{kg}$, a series of flow simulations were conducted using the same decreasing concentrations of CO_2 as with the high enthalpy flow. The highest CO_2 used was 50% and decreased 10% per simulation until the resulting change in transition location was considered nominal. Again, CO_2 was not allowed to dissociate across the shock to maintain a constant concentration of CO_2 in the boundary layer. The only gas reaction allowed that would change the concentration of CO_2 in the gas was the exchange between CO and O_2, which did not change the concentration by more then 0.2% in the boundary layer.

5.3.1 Wind Tunnel Conditions.

Figure 5.18 shows the N factor comparisons of the varying CO_2 concentrations. Even at the lower enthalpy condition, it is clearly seen that the higher concentrations of CO_2 produce lower amplification rates though with a lesser impact than seen in the

higher enthalpy flow. Highlighting the graph at x=0.8 and below (see Figure 5.19), the same reversal seen in the high enthalpy flow appears where the lower concentrations of CO_2 produce lower N factors. As the same grids were used as the high enthalpy flow, this result is caused by the same numerical error at the nosetip of the sharp cone where the streamwise resolution is too low. For the 50% flow, amplification begins right at the nose of the cone, while the 10% doesn't show any amplification until x=0.17 m, giving the appearance lower amplification despite the higher rate of amplification indicated by the slope of the line. Again, this numerical error does not impact the conclusions of this study as the comparisons are only made between the vibrational and non-vibrational results at each concentration, rather than between concentrations, and the numerical error is the same between these two simulations. The effects of this numerical error are more pronounced at these conditions than in the higher enthalpy flow.

Comparing the stability results with and without vibration, the effects of CO_2 damping are clearly higher at higher concentrations. Figure 5.20 shows the resulting N factors with and without vibration enabled, where the dashed line represent the stability results without vibration. For each concentration value, amplification starts at the same streamwise location as noted earlier, whether vibration is enable or disabled. If transition is assumed to occur at an N factor of 10, Table 5.6 shows the changes in the transition location for the various concentrations. At 50% concentration, the total change in transition location is almost 4 times higher than that at 10%. If a transition location change of less than 10 cm was considered to be nominal, in a low enthalpy flow, a minimum of approximately 30% CO_2 is necessary to change the transition location by at least 10 cm on a sharp cone.

The same flow conditions are used in simulations conducted on the blunt cone model. Figure 5.21 shows the N factors results of the blunt cone at 50%, 30% and

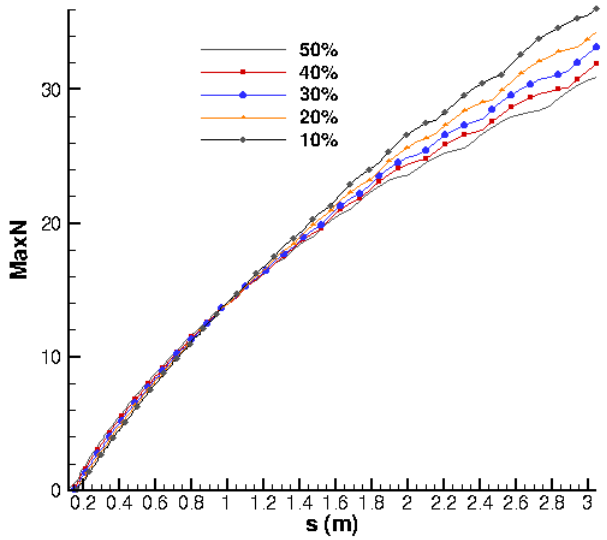

Figure 5.18. N factors for sharp cone with varying CO_2 concentrations at low enthalpy, $5.12\frac{MJ}{kg}$

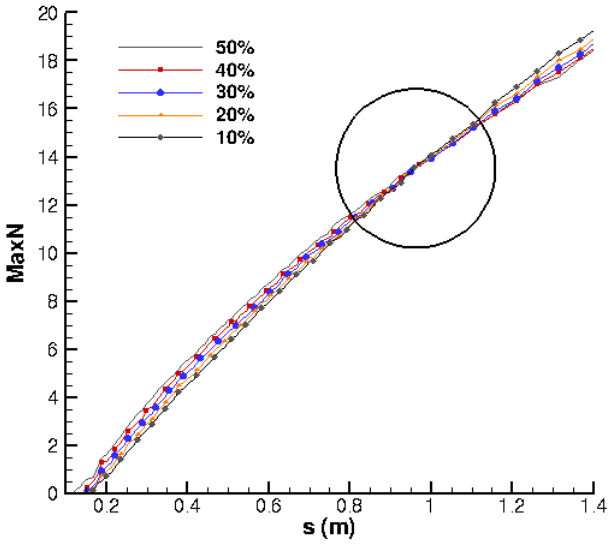

Figure 5.19. N factors near the nosetip for sharp cone with varying CO_2 concentrations at low enthalpy, $5.12\frac{MJ}{kg}$

Table 5.6. Low enthalpy transition location changes on the sharp cone

Concentration	x_{tr}	$x_{trNoVib}$	δx_{tr}
50%	0.6810	0.5279	0.153
40%	0.6941	0.5640	0.130
30%	0.7097	0.5962	0.1135
20%	0.7208	0.6391	0.0817
10%	0.7280	0.6817	0.0463

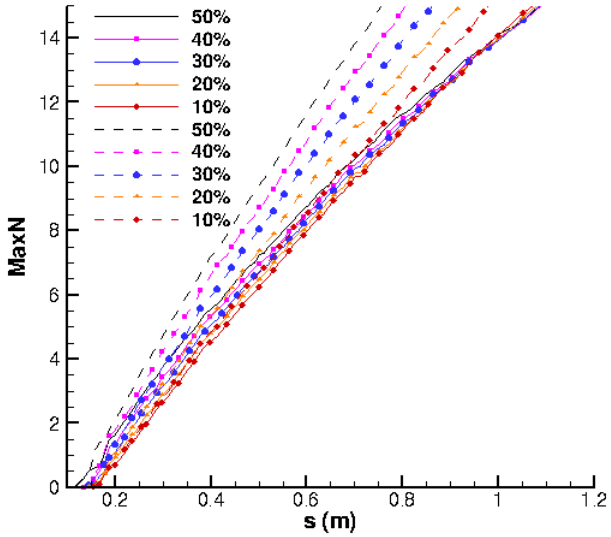

Figure 5.20. N factors for sharp cone with varying CO_2 concentrations with and without vibration at low enthalpy, $5.12\frac{MJ}{kg}$ conditions (solid lines: vibrational effects, dashed lines: no vibrational effects)

10% concentration CO_2, where the dashed lines represent non-vibrational results. Examining the non-vibrational results, the streamwise location of the start of amplification varies significantly with higher concentrations of CO_2 indicating a similar result as explained for the high enthalpy cases due to the changing gas composition. Table 5.7 shows the change in streamwise location for the blunt cone model. For the same concentration of CO_2, there is a marked increase in the change in transition location for a blunt cone compared to a sharp cone, indicating a greater damping effect on the blunt cone model than a sharp cone for the same freestream conditions. Examining the boundary flow conditions, the temperature and velocity profiles differ

between the two boundary layers. The blunt cone has a thicker velocity and thermal boundary layer and a higher temperature in the boundary layer.

Table 5.7. Low enthalpy transition location changes on the blunt cone

Concentration	x_{tr}	$x_{trNoVib}$	δx_{tr}
50%	1.9086	1.3426	0.5626
30%	1.8244	1.4482	0.3762
10%	1.7232	1.5669	0.1563
5%	1.674	1.601	0.073

Figures 5.23a through 5.23c compare the results of the sharp and blunt cones at each concentration. The differences in the starting location of the amplification without vibration enable on the blunt cones, indicates the effect of CO_2 damping on the stability of the boundary layer. The existence of the entropy layer is the cause of the delay in the start of amplification on the blunt cone compared to the sharp cone, as the entropy layer has a stabilizing effect on the second mode instability [43]. However, the results with vibration enabled show the damping effect of CO_2 on the boundary layer stability. As the concentration of CO_2 increases, the start of amplification continues to moves downstream in the streamwise direction for both cases. At 50% concentration of CO_2, amplification starts at 1.0 m, but this is decreased to 0.9 m for a 10% concentration. However, at 50% concentration of CO_2, the difference in the location of the start of amplification between the vibrational and non-vibrational stability analyses shows a 0.3 m change in amplification start. This difference is reduced to only 0.05 m for the flow with 10% concentration.

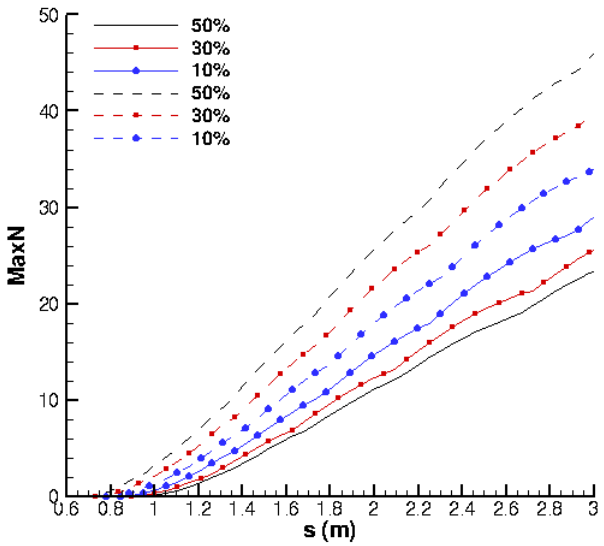

Figure 5.21. N factors for a blunt cone at low enthalpy, $5.12\frac{MJ}{kg}$

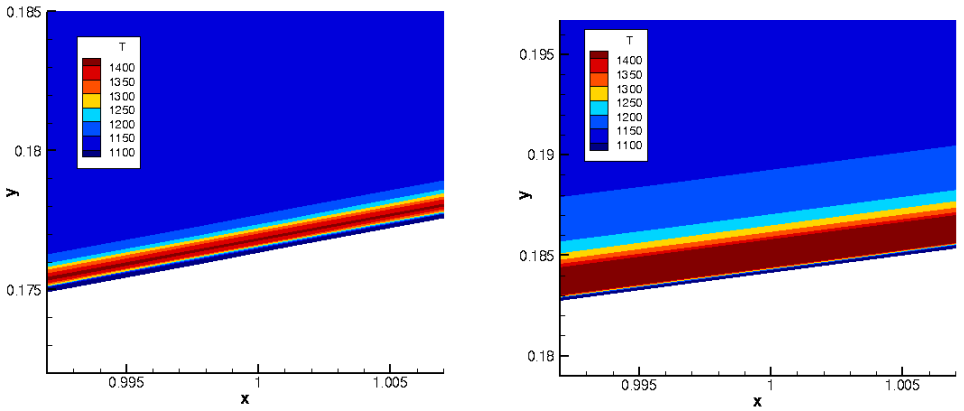

(a) Contour plot of temperature on sharp cone

(b) Contour plot of temperature on blunt cone

Figure 5.22. Temperature contours of boundary layer on a blunt and sharp cone at low enthalpy, $5.12\frac{MJ}{kg}$

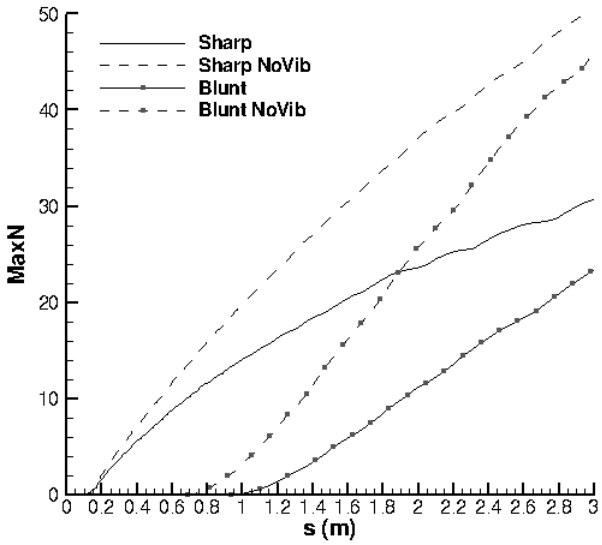

(a) N factors for 50% CO_2 concentration

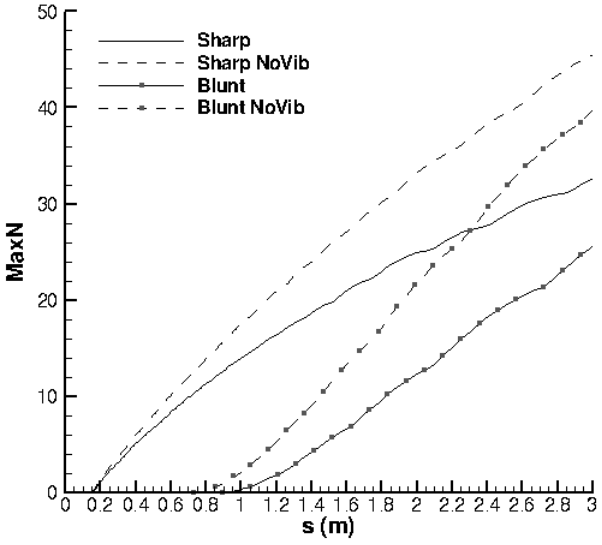

(b) N factors for 30% CO_2 concentration

Figure 5.23. N factors for CO_2 concentrations with and without vibration for the sharp and blunt cone at low enthalpy, $5.12\frac{MJ}{kg}$

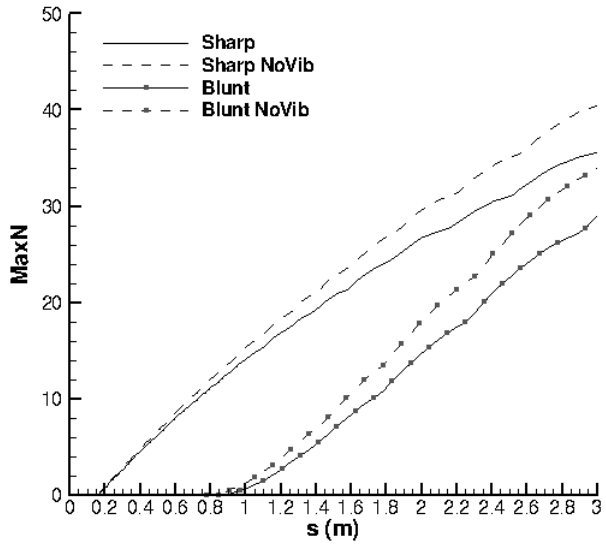

(c) N factors for 10% CO_2 concentration

Figure 5.23. N factors for CO_2 concentrations with and without vibration for the sharp and blunt cone at low enthalpy, $5.12\frac{MJ}{kg}$

Examining the temperature of the flow along the body, the blunt cone has a significantly higher temperature in the boundary layer than does the sharp cone. This increased temperature in the boundary layer allows for more CO_2 vibrational damping to occur as more vibrational modes can be activated at the higher temperatures and thus less amplification of boundary layer instabilities. Figures 5.22a and 5.22b show the temperature contours on the sharp and blunt cones at this streamwise location.

5.3.2 Equivalent Flight Representative Freestream Conditions.

A similar examination of flight representative freestream simulations compared to the lower enthalpy wind tunnel conditions was conducted, using a 30% CO_2 concentration. The freestream flow parameters were modified to maintain the freestream total enthalpy but match flight representative parameters (freestream values of density of $1.864x10^{-1}\frac{kg}{m^3}$, T and T_v of 216.2 K, and velocity of 3000 $\frac{m}{s}$). Figure 5.26 shows an N factor comparison over the sharp cone, with vibrational enabled and disabled, for matching enthalpy conditions. The flight conditions were changed such that the boundary layer maximum temperature matched ($1.864x10^{-2}\frac{kg}{m^3}$, T and T_v of 216.2 K, and velocity of 3500 $\frac{m}{s}$). Comparing the results at these new conditions shows a similar, though less pronounced effect as was seen at the high enthalpy conditions. Figure 5.27 shows the stability analysis results of these two flow conditions, with and without vibration enabled. Examining the results of these three simulations show a similar trend to the high enthalpy results (Figure 5.28). Again, the flight representative flows have Reynolds numbers approximately 10 times higher than the wind tunnel flow, $4.2x10^7$ and $3.6x10^7$ versus $4.1x10^6$. However, the overall impact on the transition location is similar, with the wind tunnel case having an 11 cm delay in transition, with the flight representative cases having an 8.4 cm and 9.9 cm delay for matching enthalpy and temperature, respectively. Figure 5.30 shows the boundary

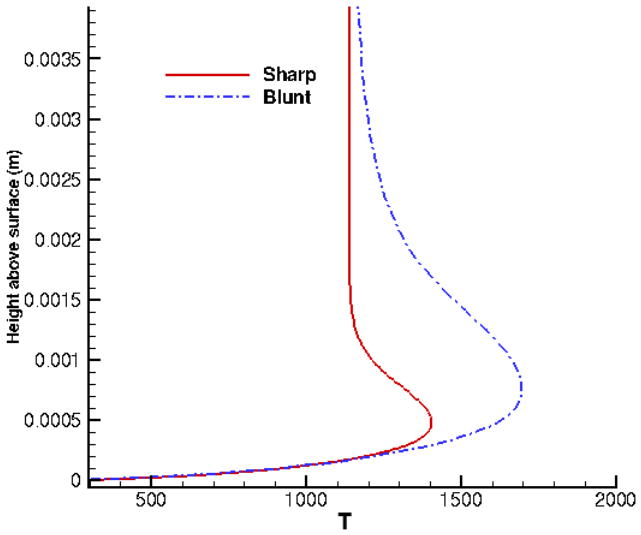

Figure 5.24. Temperature profile in the boundary layer at x=1.0 m for the sharp and blunt cone

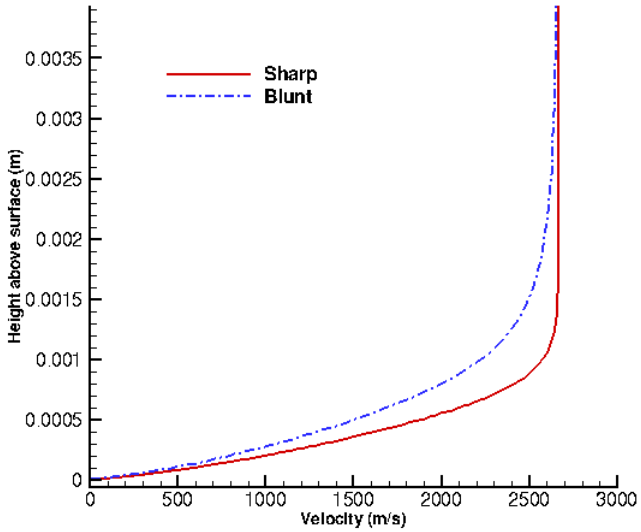

Figure 5.25. Velocity profile in the boundary layer at x=1.0 m for the sharp and blunt cone

layer temperature profiles for all three cases. The same general trends as with the high enthalpy flow are seen in the lower enthalpy flow and, again, the higher sustained temperatures with the wind tunnel conditions may allow for greater CO_2 damping effects. As with the high enthalpy cases, if the N factors for the wind tunnel and flight simulations are compared without the Reynolds number effect, the CO_2 damping on the stability of the flow is very similar (see Figure 5.29).

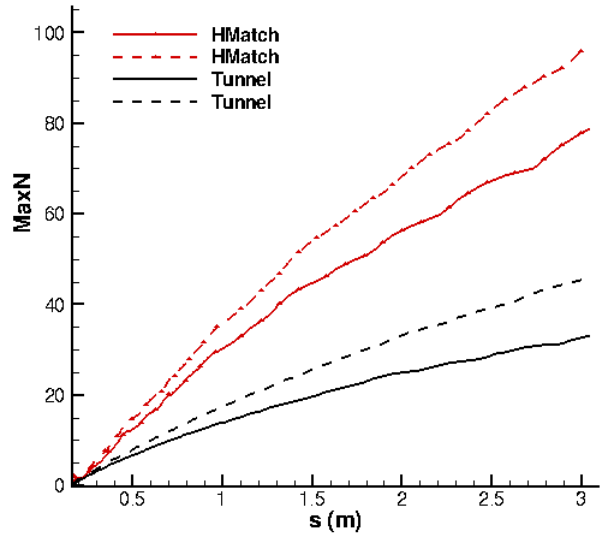

Figure 5.26. N factors for matching enthalpy between wind tunnel and flight representative conditions (solid lines: vibrational effects, dashed lines: no vibrational effects)

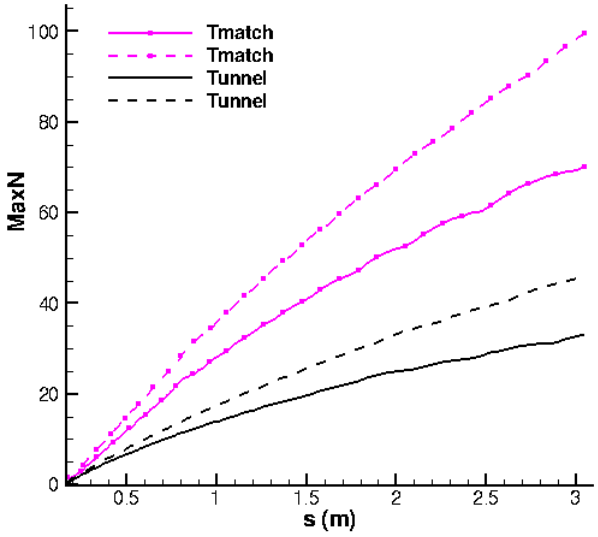

Figure 5.27. N factors for matching maximum boundary layer temperatures between wind tunnel and flight representative conditions (solid lines: vibrational effects, dashed lines: no vibrational effects)

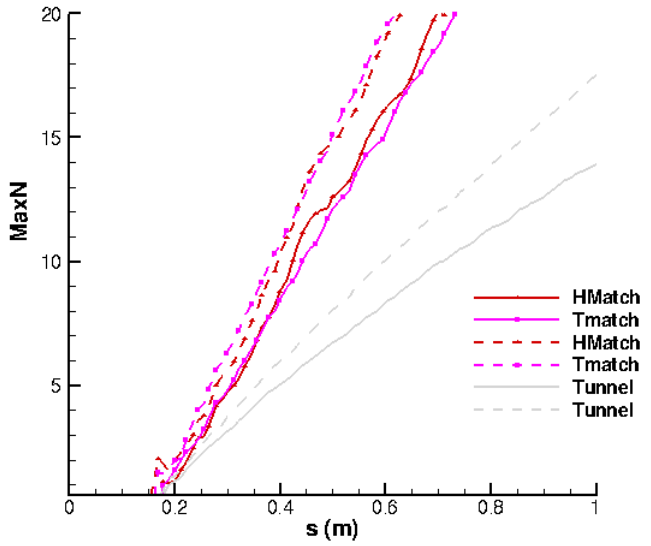

Figure 5.28. N factors for wind tunnel and flight representative conditions (solid lines: vibrational effects, dashed lines: no vibrational effects)

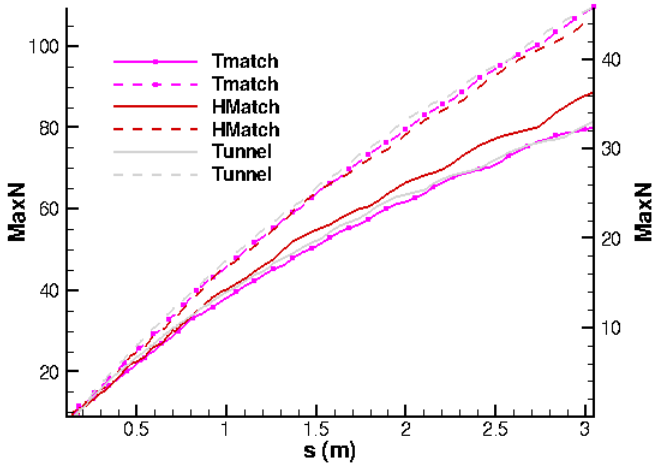

Figure 5.29. N factors for wind tunnel and flight representative conditions without Reynolds number effects (solid lines: vibrational effects, dashed lines: no vibrational effects)

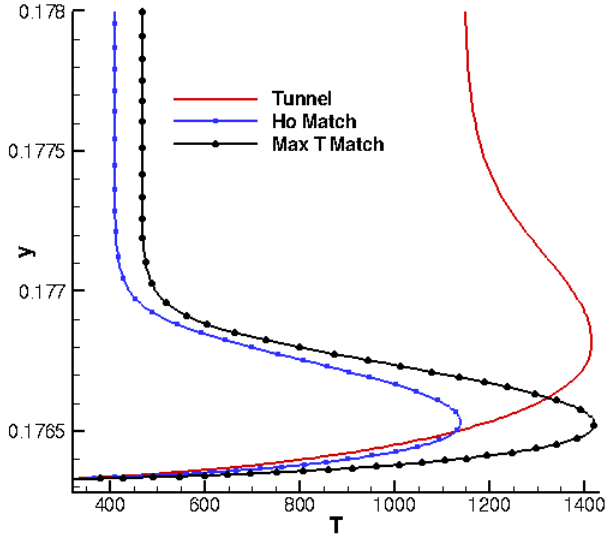

Figure 5.30. Temperature profile for x=1.0 m for wind tunnel and flight representative conditions

6. Ablation Model Results

6.1 Low Density Results

The first freestream conditions considered for a study to compare the different gas-surface ablation models and the subsequent affect on hypersonic boundary layer stability was re-entry type condition at high altitude, resulting in flow conditions with a freestream density of $7.5995 \times 10^{-3} \frac{kg}{m^3}$, T and T_v of 216.2 K with an angle of attack of 0 degrees. Simulations at this condition were conducted on both the blunt and sharp cones. Simulations were conducted at both a high and low enthalpy condition, approximately 18 $\frac{MJ}{kg}$ and 5 $\frac{MJ}{kg}$, respectively. At the high enthalpy flow condition, the minimum edge Mach number for the sharp cone is 9 and for the blunt cone is 4. At these edge Mach numbers, the flow should be dominated by second mode instabilities [42]. For the low enthalpy flow, the edge Mach numbers are 6 and 3 for the sharp and blunt cone, respectively. These flows should also be dominated by second mode instabilities. However, with an edge Mach number of 3, the possibility exists for the blunted cone to have first mode instabilities which may dominate.

6.1.1 High Enthalpy Flow - $V_\infty = 6000 \frac{m}{s}$, total enthalpy = 18.2 $\frac{MJ}{kg}$.

The mass fluxes at the surface along the body for each of the models when simulated on a blunt cone at the above conditions are presented in Figures 6.1a through 6.1e. The positive flux shows species being adsorbed or condensed onto the surface and the negative flux shows are species desorbed or sublimated from the surface. The two Park and MURI models do not produce an appreciable amounts of CO_2, whereas the ZA and MZA models do. Examining the surface fluxes clearly shows the models produce significantly different results for the species and amounts of each species produced. The Park and Park 76 models produce similar fluxes with the exception

of C_3, which is only produced in the Park model. The ZA and MZA models produce similar fluxes from the surface with the exception of a slight decrease in the CO_2 flux from the surface for the MZA model. While the flux from the surface are the direct result from the different models, it is the overall concentration of CO_2 in the boundary layer, as a result from the combination of the gas-surface species reacting in the gas phase with the gas model, which will affect the stability of the boundary layer. The maximum concentration of CO_2 in the boundary layer is shown in Figure 6.2. The highest concentration was almost 20% CO_2 at the nose and then quickly decreasing to less that 5% for the ZA and MZA. The other models produced less than 1%.

Examining the distribution of CO_2 within the boundary layer shows the highest concentration is located near the wall from ablation and decreases with increase wall normal direction. Figure 6.3 shows that for the Park model the thermal boundary layer is much larger than the concentration boundary layer and the concentration of ablation products decreases significantly before the thermal boundary layer reaches its maximum temperature. This result is consistent with the other models used, varying only in the total concentration of CO_2. From boundary layer theory and Mack's work [42], the second mode instabilities will occur near the wall where the relative sonic line which traps the acoustic-type wave. The higher concentration of CO_2 near the wall should promote damping on the second mode instabilities. However, the thermal boundary layer profile shows that the higher temperatures are reached not at the maximum CO_2 concentration, but as the concentration starts to decrease. The resolution of the grids used in the study are not resolved enough to determine where the correlation between the location of the instabilities and the boundary layer temperature or CO_2 concentration at that location.

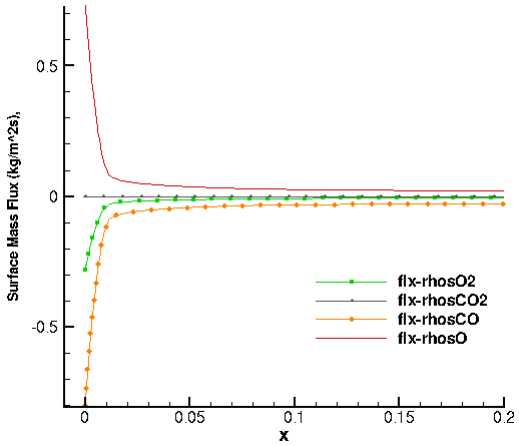

(a) Surface mass flux on Park76 model

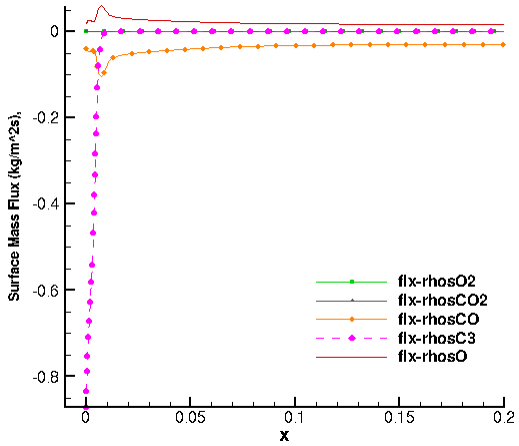

(b) Surface mass flux on Park model

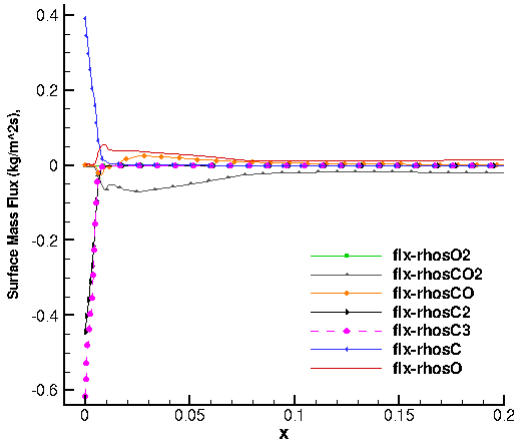

(c) Surface mass flux on ZA model

Figure 6.1. Surface mass flux on blunt cone at V=6000 $\frac{m}{s}$, low density

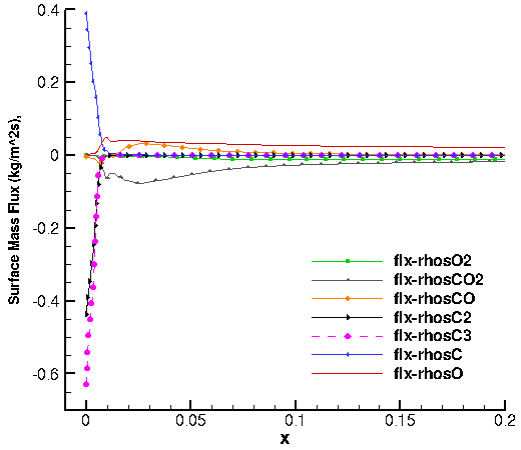

(d) Surface mass flux on MZA model

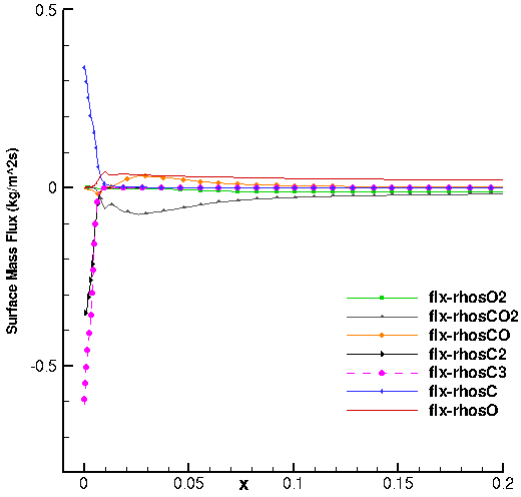

(e) Surface mass flux on ZA with nitridation (Alba) model

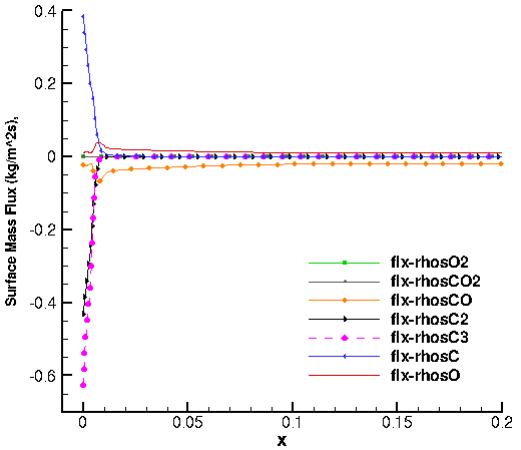

(f) Surface mass flux on MURI model

Figure 6.1. Surface mass flux on blunt cone at V=6000 $\frac{m}{s}$, low density

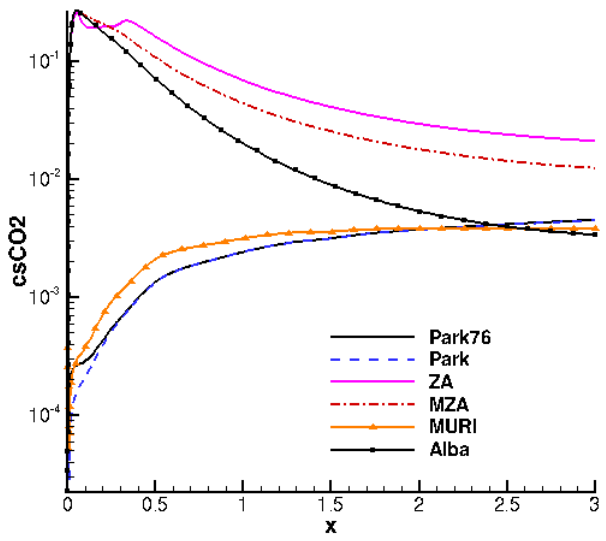

Figure 6.2. Maximum concentration of CO_2 along the blunt cone at V=6000 $\frac{m}{s}$, low density

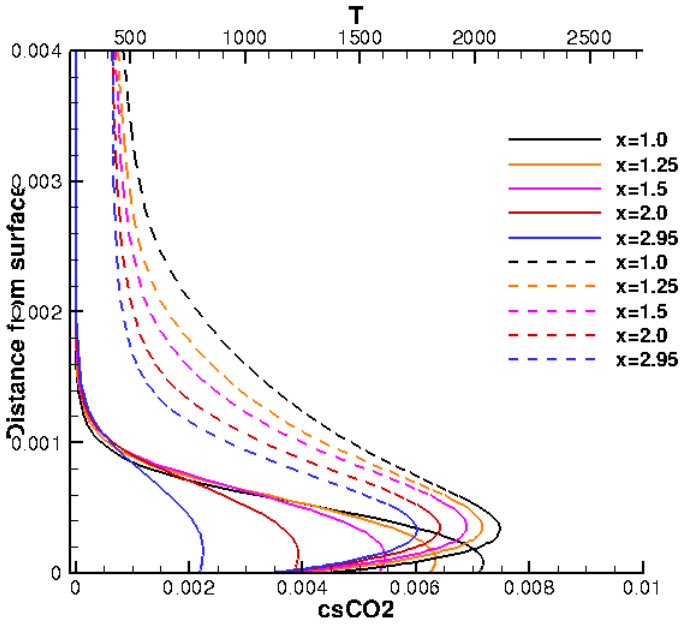

Figure 6.3. Thermal and concentration boundary layer thickness at x= 1.0 m on a blunt cone using the Park model at V=6000 $\frac{m}{s}$, low density

Comparing the results of the stability analysis, the maximum N factor envelopes are shown in Figure 6.4. The ZA and MZA models which produces significantly higher CO_2 concentrations show similar N factor results as the Park models, which also had concentrations of less than 1% CO_2. The concentration of CO_2 does not appear to have a direct correlation on the resulting stability of the boundary layer. The maximum N factor at this flow condition for any model is approximately 4.5, which is not significant amplification and would not be expected to cause transition. The combined effect of the low CO_2 concentration and the low amplification show no impact of CO_2 damping on this flow condition.

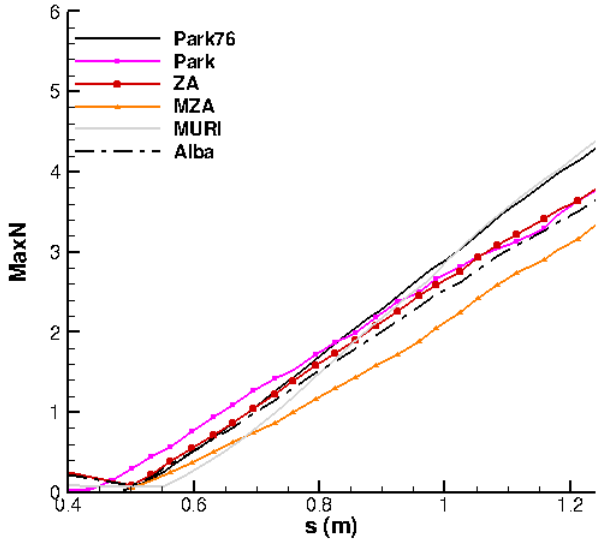

Figure 6.4. Maximum N factor for all ablation models at V=6000 $\frac{m}{s}$, low density

As CO_2 damping is known to affect the higher frequencies more than lower frequencies, if the amplification rate per frequency is examined a clearer determination of the damping effect can be made. Figures 6.5a through 6.5c shows these results. Due to the similar results of Park versus the Park76 model and ZA versus the MZA model only one frequency analysis is shown. In these figures, the no ablation model shows the amplification per frequency without CO_2 in the flow and is represented by the solid line. The amplification per frequency results when ablation is modeled is

shown dashed line with the highest amplification marked by a solid square symbol. The Park model shows almost no difference in the amplification value per frequency as compared to the no ablation model as compared to the ZA and MURI models (see Figure 6.5a). The ZA and MURI models both show no amplification at higher frequencies compared to a simulation with no ablation. This lack of high frequency amplification would be expected to reduce the overall N factor and would indicate CO_2 damping. However, examining Figure 6.11a showing the stability diagram, the high frequency amplification occurs only over a small streamwise range which would not contribute much to the overall maximum N factor, which may explain why the ZA and MZA models do not show reduced N factors as compared to those with lower CO_2 concentrations in conjunction with the low overall amplification. If the ZA model stability analysis is conducted disabling the vibrational modes (see Figure 6.6), the N factor results are nearly identical to the results using vibrational energy relaxation, indicating a negligible impact of CO_2 damping on the stability of the flow at these conditions with this concentration and amplification.

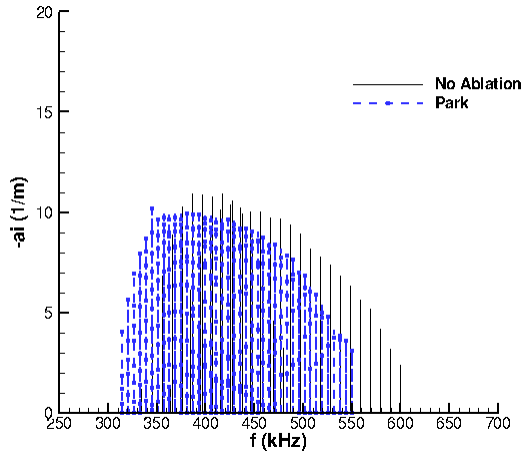

(a) Frequency Comparison with Park Model

Figure 6.5. Frequency Comparison on a blunt cone at V=6000 $\frac{m}{s}$, low density

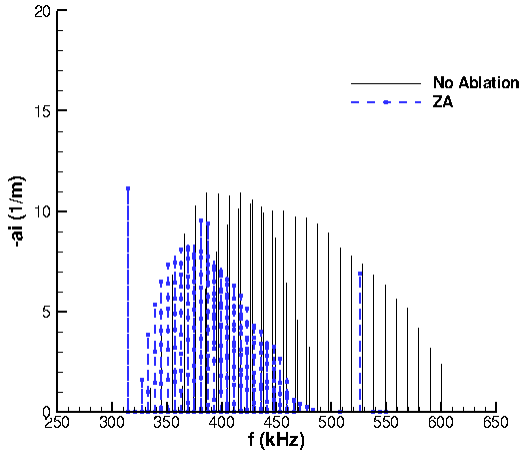

(b) Frequency Comparison with ZA Model

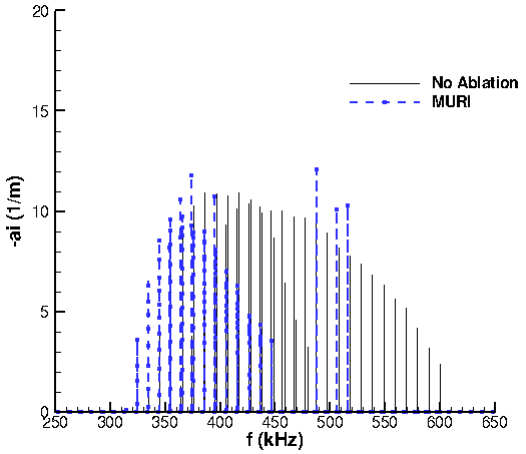

(c) Frequency Comparison with MURI Model

Figure 6.5. Frequency Comparison on a blunt cone at V=6000 $\frac{m}{s}$, low density

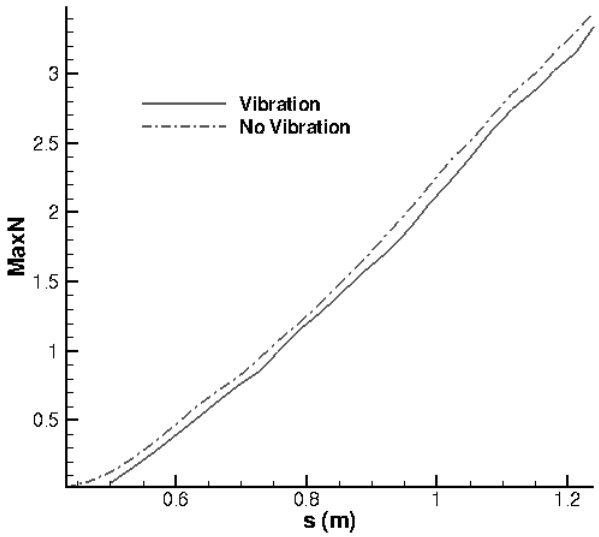

Figure 6.6. Stability results with vibrational relaxation enabled and disabled for the ZA model (solid lines: vibrational effects, dashed lines: no vibrational effects)

For the sharp cone at the same freestream conditions, there is a significant reduction in the CO_2 produced by ablation. Due to the attached shock with the sharp cone and smaller total surface area at high temperatures, there is a significant drop in the production of all ablative species. Figures 6.7a through 6.7f show the flux of species from the surface with a sharp cone.

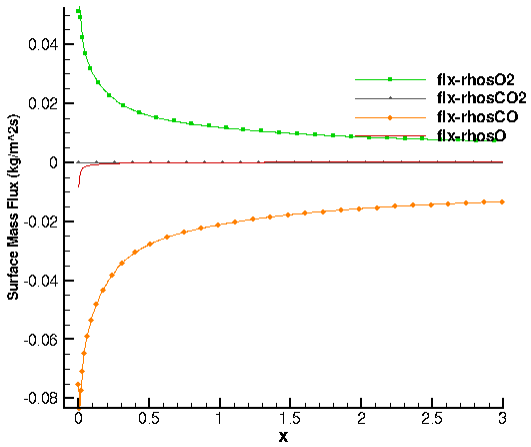

(a) Surface mass flux on Park76 model

Figure 6.7. Surface mass flux on sharp cone at V=6000 $\frac{m}{s}$, low density

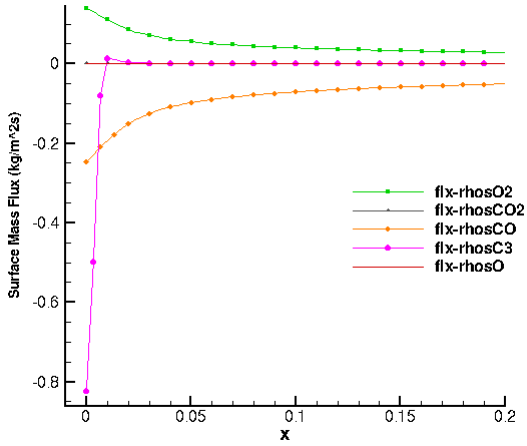

(b) Surface mass flux on Park model

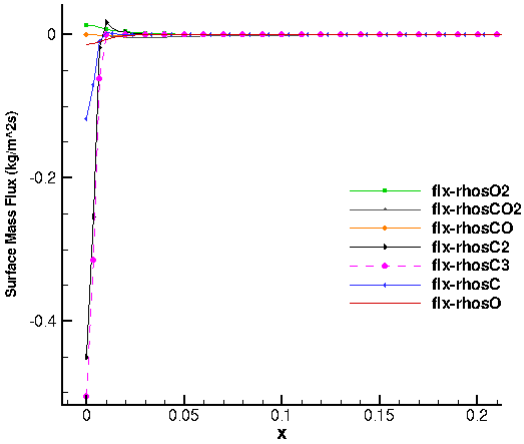

(c) Surface mass flux on ZA model

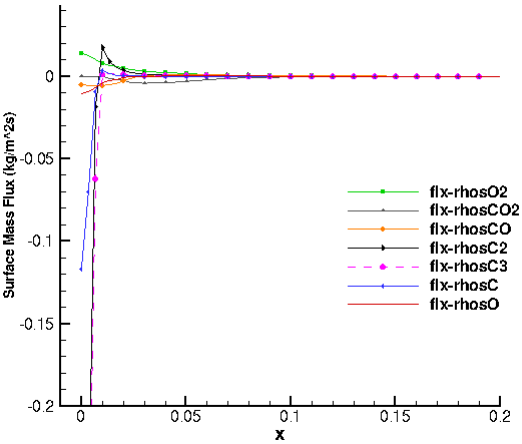

(d) Surface mass flux on MZA model

Figure 6.7. Surface mass flux on sharp cone at V=6000 $\frac{m}{s}$, low density

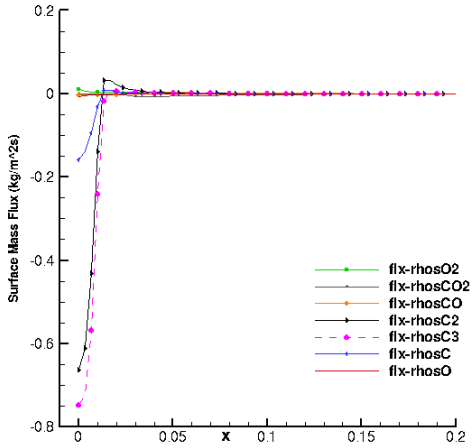

(e) Surface mass flux on ZA with nitridation (Alba) model

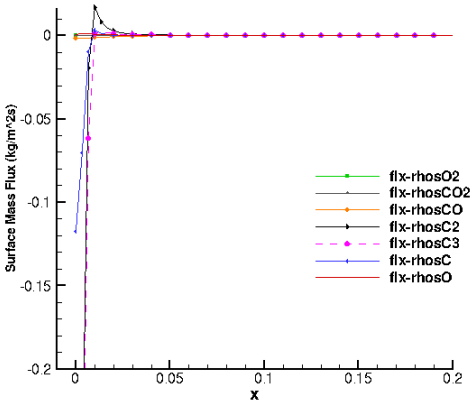

(f) Surface mass flux on MURI model

Figure 6.7. Surface mass flux on sharp cone at V=6000 $\frac{m}{s}$, low density

Of note, the principle adsorbed species for the sharp cone is O_2 instead of atomic oxygen as was seen in the blunt nose cone due to weaker shock which causes less dissociation of oxygen. Examining the total concentration of CO_2 shown in Figure 6.8 along the sharp cone body, the two Park models produce more CO_2 than the other three models, however, the total concentration of CO_2 is less than 0.5% (except for an initial spike at the nose for the ZA and MZA models around 1%, which quickly decreases to 0.1%). At these low concentrations of CO_2 in the flow over a sharp cone there would be no expected effect of CO_2 damping on the stability based on the results of the concentration study conducted.

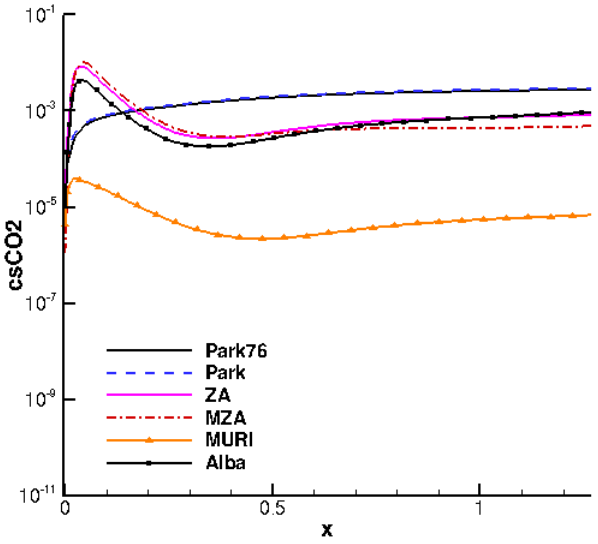

Figure 6.8. Concentration of CO_2 along the body for a sharp cone at V=6000 $\frac{m}{s}$, low density

Examining the N factors produced with the sharp cone, the maximum N factor is 6.1 at s=1.27m as given by Figure 6.9). A similar result is seen with the sharp cone geometry as with the blunt cone in that the total variation in the maximum N factor is around 20% for all the models at x=1.27m and does not correlate to the concentrations of CO_2 in the flow.

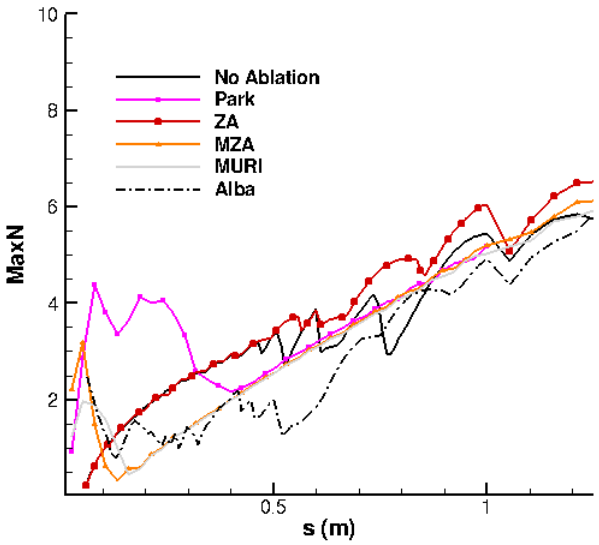

Figure 6.9. Maximum N factor for all ablation models on a sharp cone at V=6000 $\frac{m}{s}$, low density

Inspecting the amplification rates at specific frequencies, shown in Figures 6.10a through 6.10c, leads to more insight into whether CO_2 is having a damping effect as the higher frequencies would show less damping than the lower frequencies. When compared to the no ablation control simulation, none of the models show a decrease in amplification at any frequency indicating that at these conditions and concentrations CO_2 vibrational damping does not affect the instabilities. While there is significant noise in the N factor results, the overall trend of low amplification is apparent.

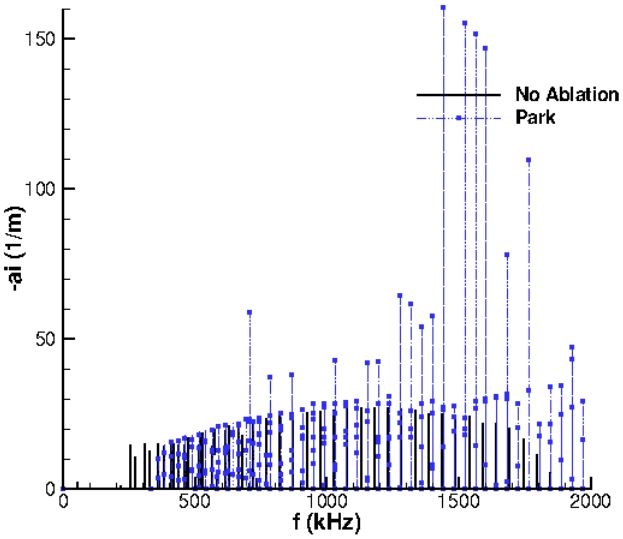

(a) Frequency Comparison with Park Model

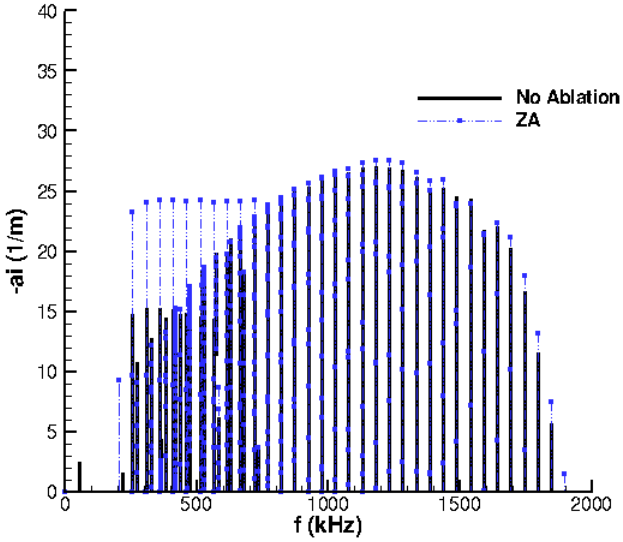

(b) Frequency Comparison with ZA Model

Figure 6.10. Frequency Comparison on a sharp cone at V=6000 $\frac{m}{s}$, low density

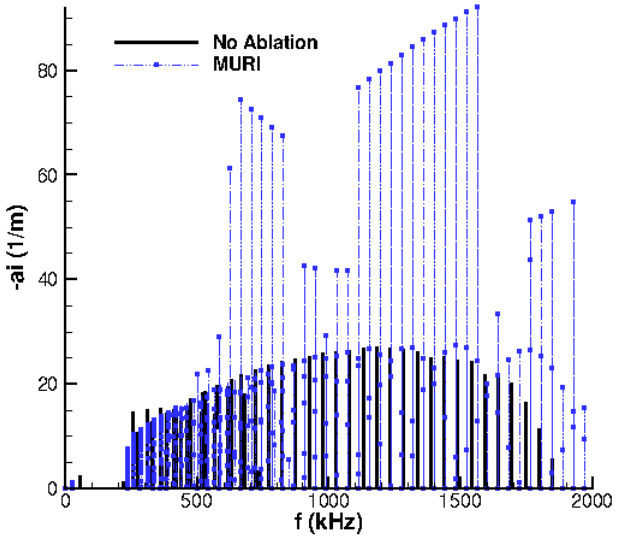

(c) Frequency Comparison with MURI Model

Figure 6.10. Frequency Comparison on a sharp cone at V=6000 $\frac{m}{s}$, low density

While the differences in maximum N factor envelope between the blunted and sharp nose geometries are relatively small, the actual stability diagram shows a marked difference in the frequencies which are amplified. Figures 6.11a and 6.11b show the stability diagrams for the two geometries with no ablation. The blunted cone shows no amplification at frequencies above 600 kHz and this amplification starts at 0.5 m along the body. The sharp cone shows amplification at 2 MHz which start very near the nosetip. Furthermore, the total amplification for the blunted nose geometry is 11 while the sharp cone geometry total amplification was 23. This stability of the blunted cone is caused by the stabilizing effect of the entropy layer on the second mode instabilities [22]. Another significant result is the amplified frequencies. Work by Fujii showed that the maximum damping rate of CO_2 was primarily in the 1-10 MHz range and decreased as frequencies increased further [9]. The decreased amplification of the instabilities is likely a result of the entropy layer and not from the presence of CO_2. Furthermore, the amount of CO_2 in the flow at these conditions is minimal when compared with the concentration study results and would have little effect on the stability of the boundary layer.

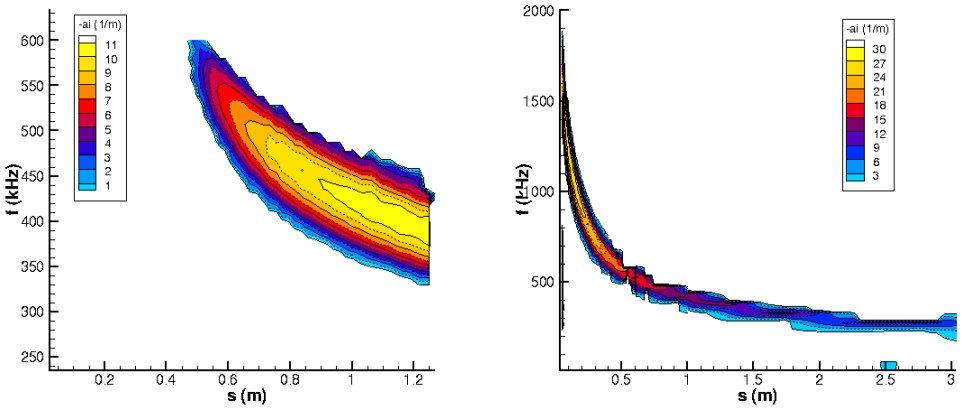

(a) Stability diagram for blunt cone (b) Stability diagram for sharp cone

Figure 6.11. Stability diagrams with no ablation at V=6000 $\frac{m}{s}$, low density

6.1.2 Low Enthalpy Flow - $V_\infty = 3000\ \frac{m}{s}$, total enthalpy $= 4.7\ \frac{MJ}{kg}$.

The sharp and blunt cone geometries were also examined at a lower enthalpy, 5.0 $\frac{MJ}{kg}$, with a freestream velocity of 3000 $\frac{m}{s}$ at the same freestream density and temperatures. Figures 6.12a through 6.12f show the surface fluxes for each model at this slower velocity on the blunt cone. The models show a slight reduction in the flux of the species from the surface mainly due to the lower gas temperatures surrounding the wall boundary condition but the surface temperature being the same as for the earlier flows.

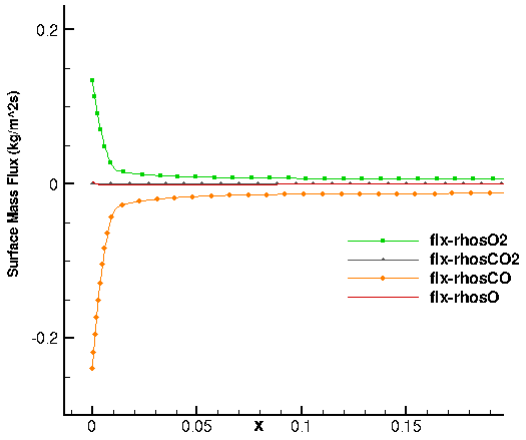

(a) Surface mass flux on Park76 model

Figure 6.12. Surface mass flux at V=3000 $\frac{m}{s}$, low density

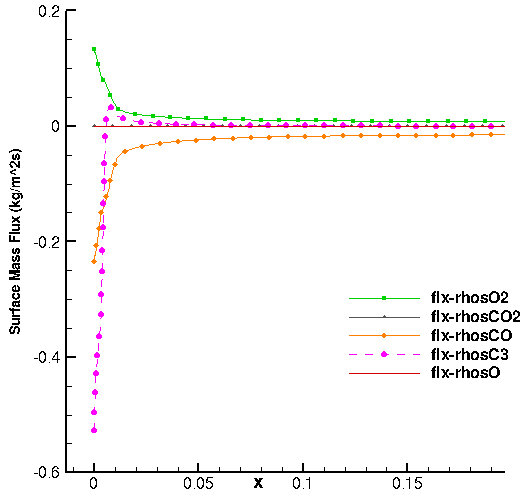

(b) Surface mass flux on Park model

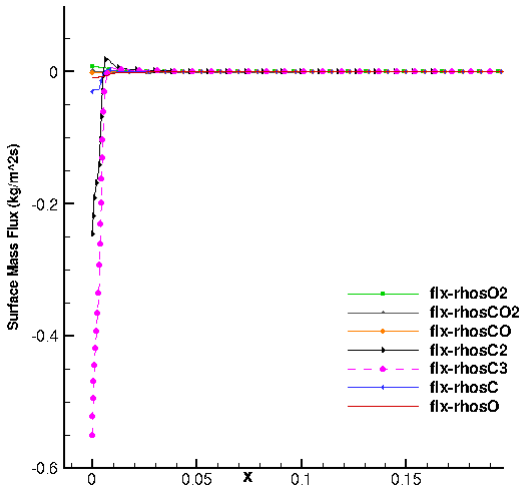

(c) Surface mass flux on ZA model

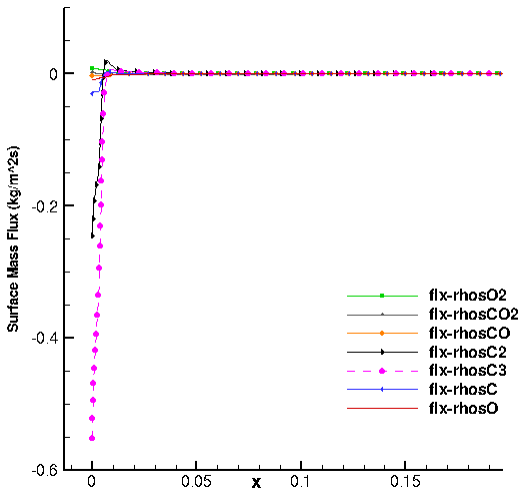

(d) Surface mass flux on MZA model

Figure 6.12. Surface mass flux at V=3000 $\frac{m}{s}$, low density

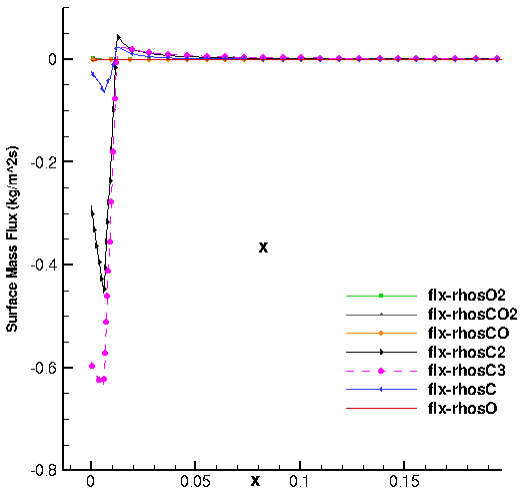

(e) Surface mass flux on ZA with nitridation (Alba) model

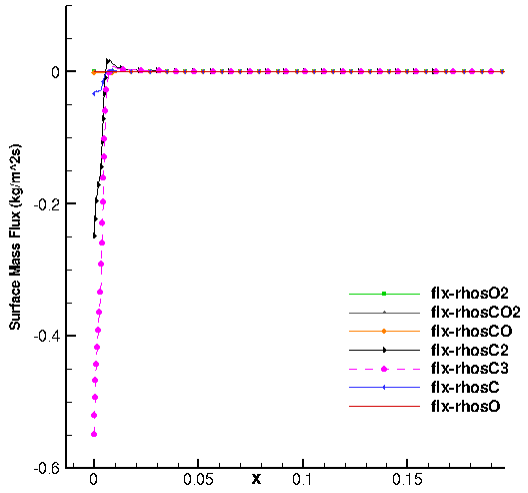

(f) Surface mass flux on MURI model

Figure 6.12. Surface mass flux at V=3000 $\frac{m}{s}$, low density

There is a significant reduction in the total surface mass flux and the CO_2 concentration in the boundary layer on the sharp cone compared to the blunt cone for this case, similar to the higher enthalpy case. Comparing concentrations of CO_2, presented in Figure 6.13 and 6.14, all models show a similarly small quantity, less than 1%. As would be expected from the results of the concentration study and the high enthalpy flow results, the N factors show very little variation, less than 10%, for the blunt cone, and less than 12% for the sharp cone. There is considerable noise in the stability analysis N factor results on the sharp cone most likely caused either by a mismatch between the stability grid which causes interpolation of the flow values used to calculated amplification. Refining to a smaller steps should eliminate some of this noise but is computationally very expensive. The trends seen between the models, as well as the small concentration of CO_2 in the flow at these conditions, make the added computational cost unnecessary. The variations in N factor at these CO_2 concentrations are not caused by CO_2 damping.

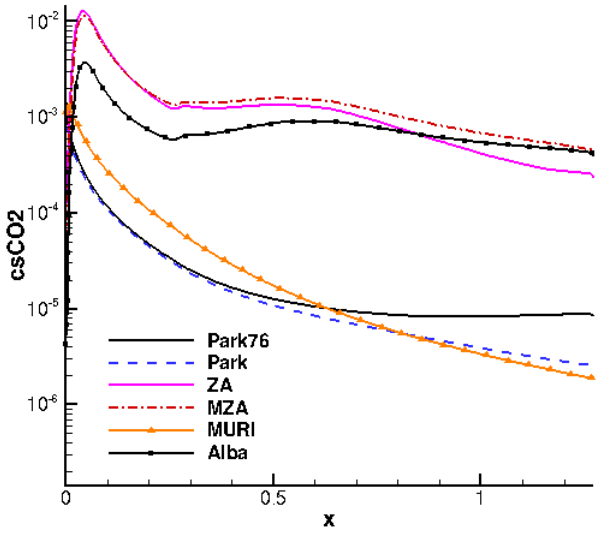

Figure 6.13. Concentration of CO_2 along the body for the blunt cone at V=3000 $\frac{m}{s}$, low density

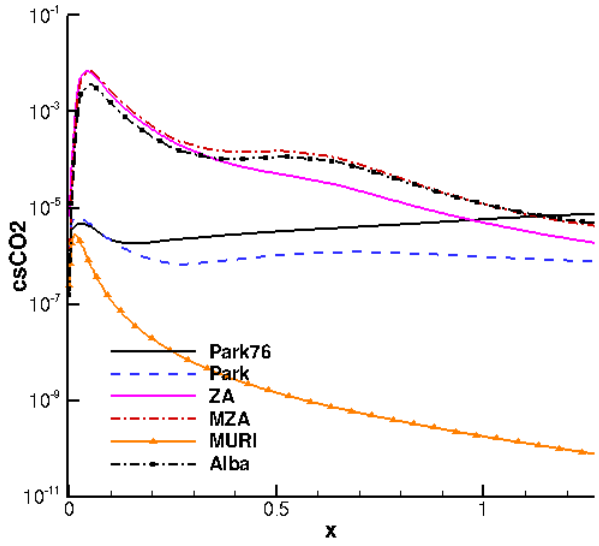

Figure 6.14. Concentration of CO_2 along the body for a sharp cone at V=3000 $\frac{m}{s}$, low density

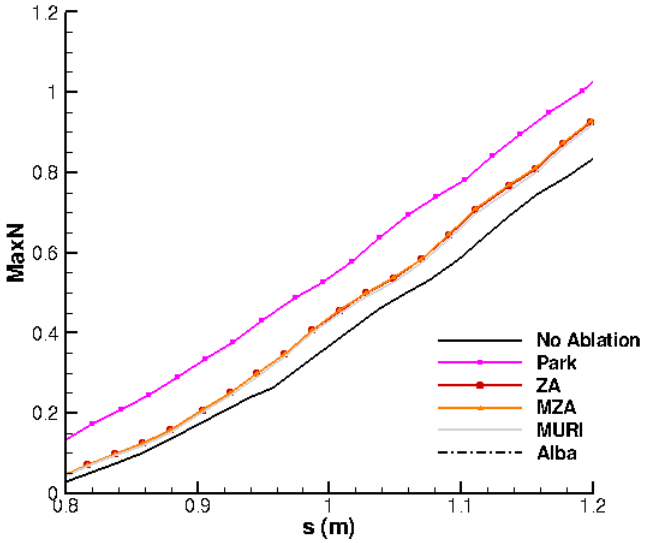

Figure 6.15. Maximum N factor for all ablation models on a blunt cone at V=3000 $\frac{m}{s}$, low density

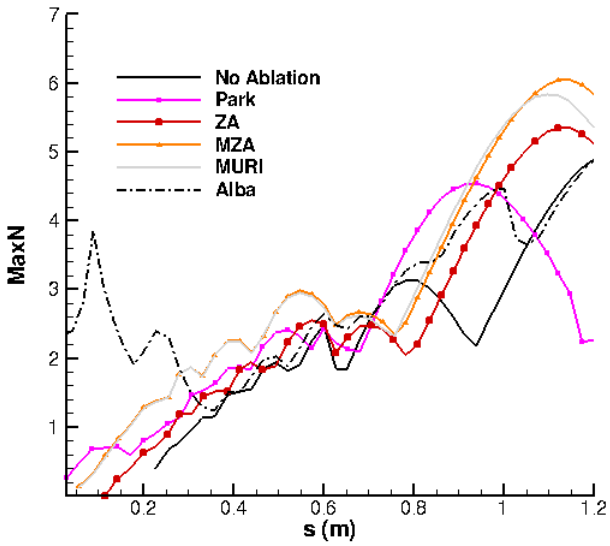

Figure 6.16. Maximum N factor for all ablation models on a sharp cone at V=3000 $\frac{m}{s}$, low density

As with the previous conditions and compared to the results of the CO_2 concentration study, this small concentration of CO_2 does not have an impact on the boundary layer stability. Comparing the maximum N factors at these conditions, neither the sharp or blunted cones show a correlation between these small concentrations of CO_2 in the flow and a reduction in the total N factor (see Figures 6.15 and 6.16). The amplification rate for the sharp cone is nearly 6 times larger than for the blunted cone, suggesting that at these flow conditions, the small changes in the nose radius of the vehicle has a significant impact on boundary layer stability, specifically with the entropy layer stabilization of the dominant second mode instability. Comparing the stability diagrams for the sharp cone to the blunt cone (seen in Figures 6.17a and 6.17), there is no amplification on the blunt cone for frequencies above about 200 kHz and amplification doesn't occur until almost 0.8 m down the body. On the sharp cone, amplification begins at 0.1 m down the body at frequencies starting around 1 MHz.

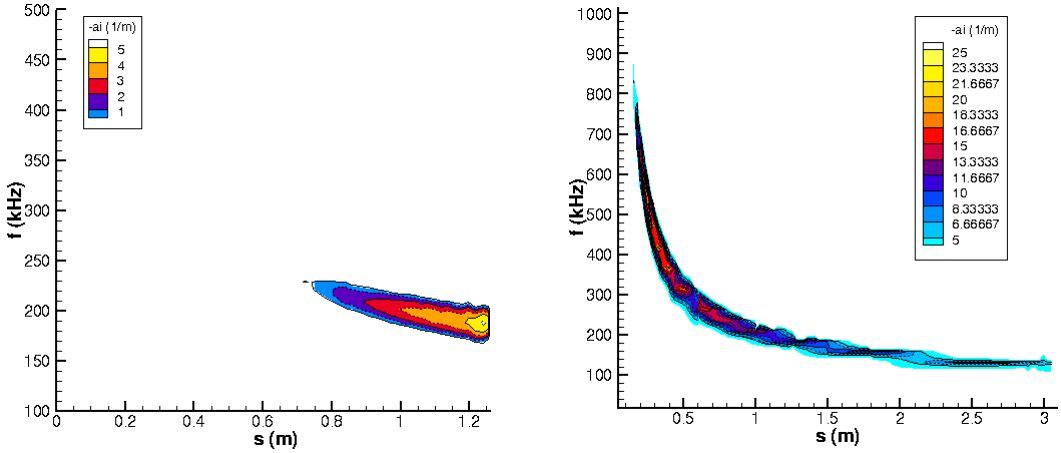

(a) Stability diagram for blunt cone

(b) Stability diagram for sharp cone

Figure 6.17. Stability diagram for sharp cone at V=3000 $\frac{m}{s}$, low density

Isolating the amplification rates per frequency for the slower velocity simulations on the blunt cone, there is little difference between the simulations with ablation and the simulation with no ablation. This frequency analysis further supports the

conclusion that at this small concentration of CO_2 there are little to no damping effects on the high frequency disturbances as the amplification per frequency on the no ablation simulation are the same as those simulations with ablation included. Figures 6.18a through 6.18c show the frequency analysis results for the blunt cone geometry and Figures 6.19a through 6.19c shows the result for the sharp cone geometries. For all figures, the base simulation, without ablation, is represented with solid lines, while the amplification per frequency on the ablation models are shown with the dashed line and the maximum vales are marked with a square symbol.

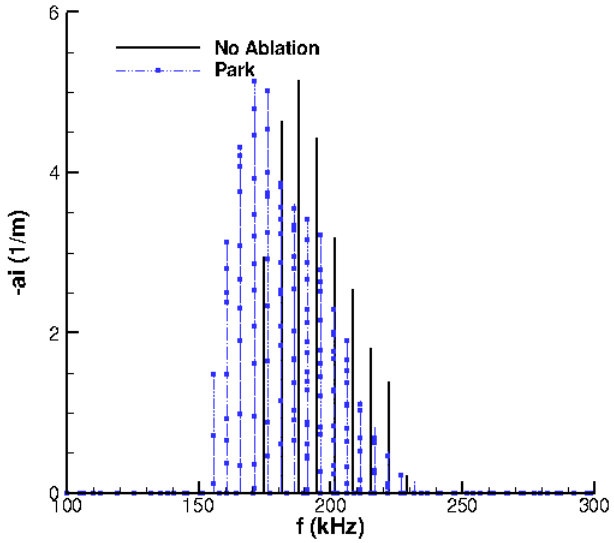

(a) Frequency Comparison with Park model

Figure 6.18. Frequency Comparison on a blunt cone at V=3000 $\frac{m}{s}$, low density

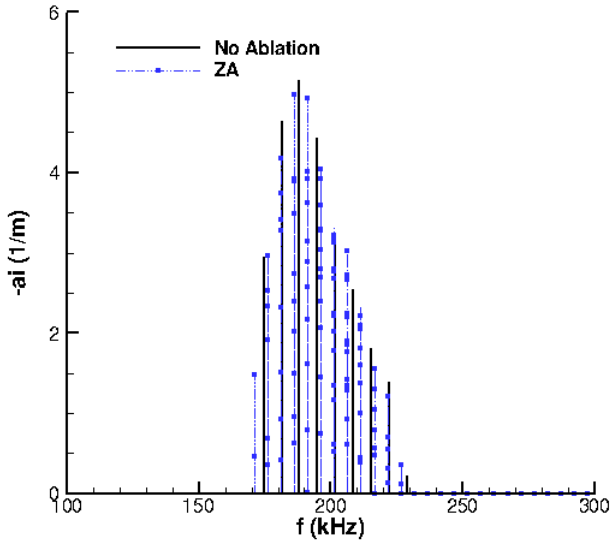

(b) Frequency Comparison with ZA model

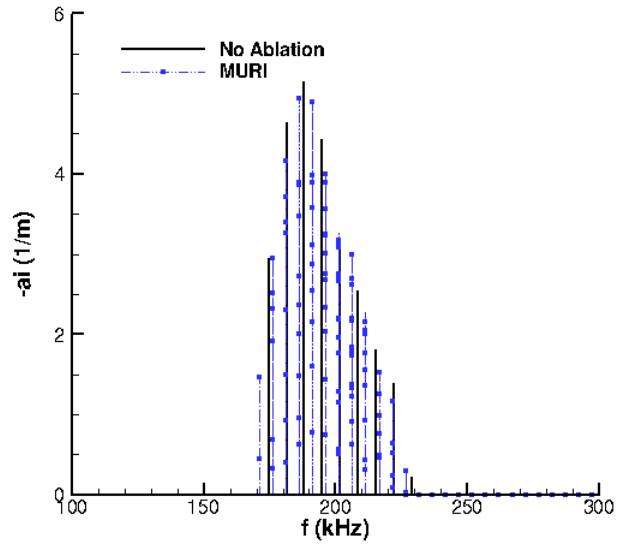

(c) Frequency Comparison with MURI model

Figure 6.18. Frequency Comparison on a blunt cone at V=3000 $\frac{m}{s}$, low density

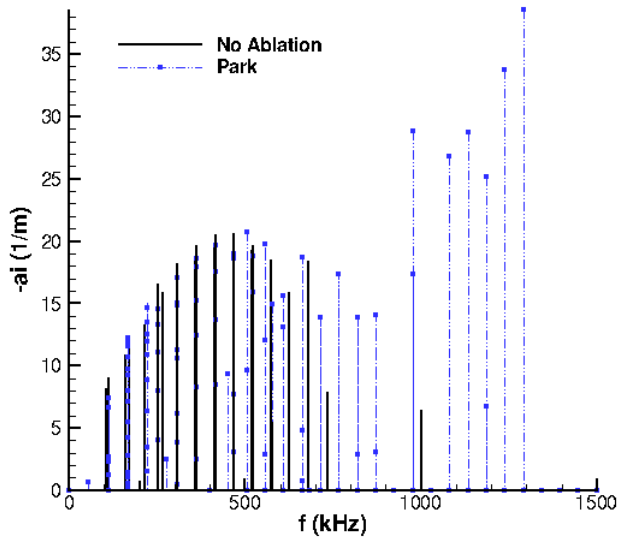

(a) Frequency Comparison with Park model

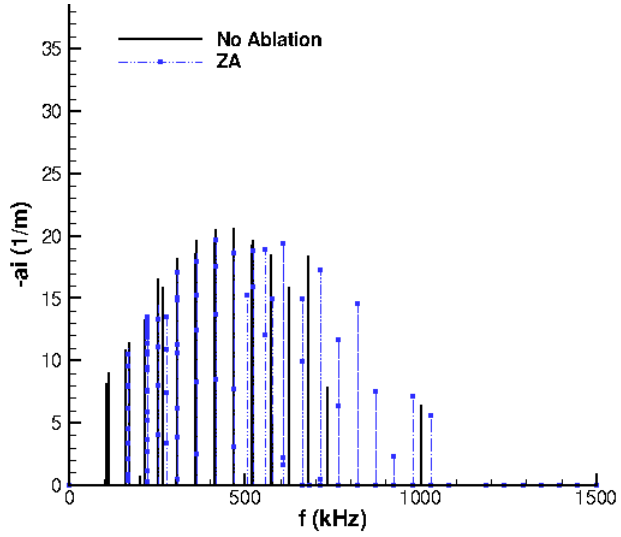

(b) Frequency Comparison with ZA model

Figure 6.19. Frequency Comparison on a sharp cone at V=3000 $\frac{m}{s}$, low density

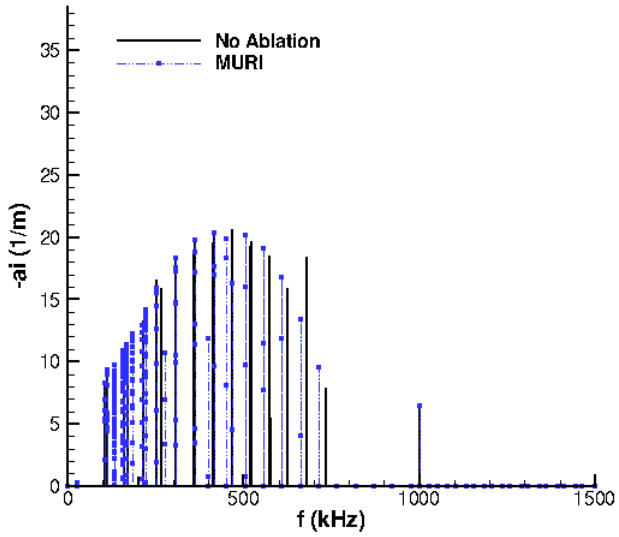

(c) Frequency Comparison with MURI model

Figure 6.19. Frequency Comparison on a sharp cone at V=3000 $\frac{m}{s}$, low density

For all of the low density simulations, whether at high or low enthalpy, the total concentration of CO_2 in the boundary layer produced by any ablation model was minimal and no impact of vibrational damping on overall boundary layer stability was observed. Using the frequency analysis to examine the total amplification per frequency, those simulations with CO_2 in the flow showed nearly identical amplification to the simulations without CO_2, further showing the lack of damping effect on stabilizing the flow. However, the total amplification seen at both enthalpy conditions in the low density simulations was low and did not have sufficient amplification to indicate a transitional boundary layers. This low amplification may have limited the impact vibrational damping would have on stability.

6.2 High Density Results

As none of the simulations at low density showed a clear effect of CO_2 damping of boundary layer stability, increasing the density of the flow (freestream conditions of density of 0.4583 $\frac{kg}{m^3}$ and a T and T_v of 238.6 K) would promote higher amplification, as well as should provide higher concentrations of CO_2 from ablation. At the high enthalpy flow condition (total enthalpy of 18.4 $\frac{MJ}{kg}$), the minimum edge Mach number for the sharp cone is 9.5 and for the blunt cone is 3.2. At these edge Mach numbers, the flow should be dominated by second mode instabilities. For the low enthalpy flow (total enthalpy of 5.0 $\frac{MJ}{kg}$), the edge Mach numbers are 7 and 2.5 for the sharp and blunt cone, respectively. These flows should also be dominated by second mode instabilities. However, the blunt cone at the low enthalpy condition could have significant, if not dominant, first mode instabilities.

6.2.1 High Enthalpy Flow - $V_\infty = 6000\ \frac{m}{s}$, total enthalpy = $18.4\ \frac{MJ}{kg}$.

The total flux of species from the gas-surface interaction models on a blunt cone are shown in Figures 6.20a through 6.20f. Figures 6.21a through 6.21f show the mass flux for all models on a sharp cones. There is a significantly higher mass flux for all species and all models at the higher density, as would be expected as the mass flux at the wall is directly proportional to the density at the wall. As was seen with the lower density results, the mass flux from the surface of the sharp cone was significantly less than the blunt cone due to the lower surface area at high temperatures. The result was a lower total CO_2 concentration in the boundary layer for the sharp cone as compared to the blunt cone, though higher concentrations than were seen at the low density conditions. The maximum CO_2 concentration in the boundary layer for the blunt and sharp cones is shown in Figures 6.22 and 6.23. As with the lower density results, the ZA and MZA models produced significant amounts of CO_2 near the nose for the blunt vehicle, a maximum concentration of 25% for the ZA model and 20% for the MZA models, which decreased down to 10% along the body. The Park76, Park, Alba and the MURI models all produced similar amounts of around 5%. For the sharp cone simulations, the variations between the all the models are smaller, with between 4-7% maximum concentrations of CO_2 in the boundary layer.

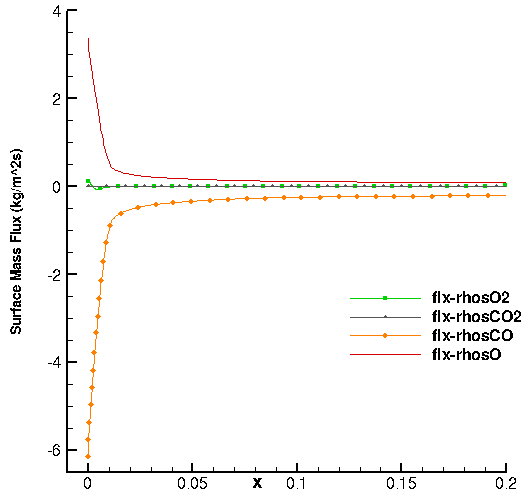

(a) Surface mass flux on Park76 model

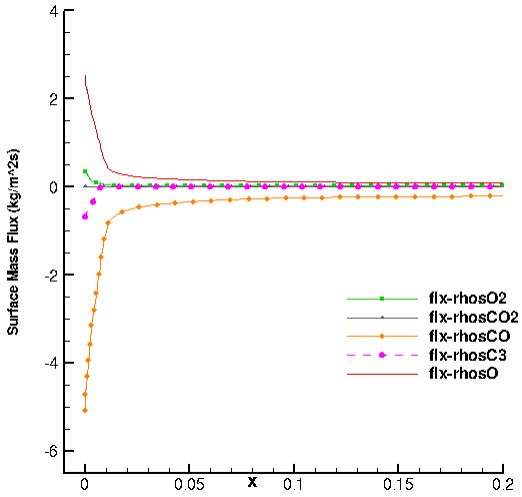

(b) Surface mass flux on Park model

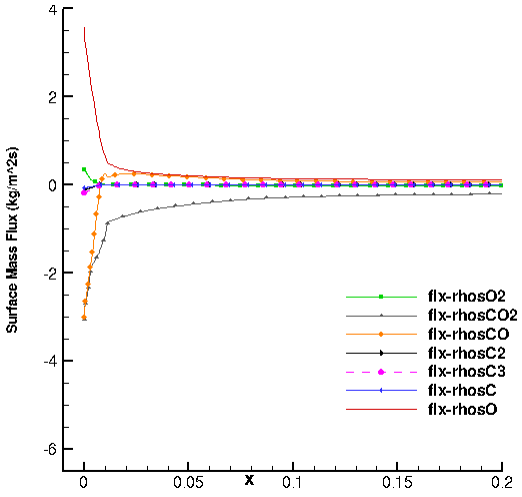

(c) Surface mass flux on ZA model

Figure 6.20. Surface mass flux on blunt cone at V=6000 $\frac{m}{s}$, high density

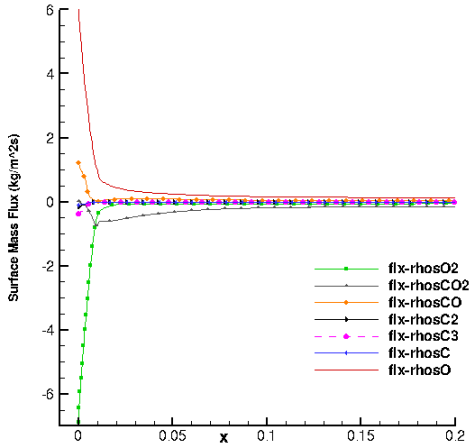

(d) Surface mass flux on MZA model

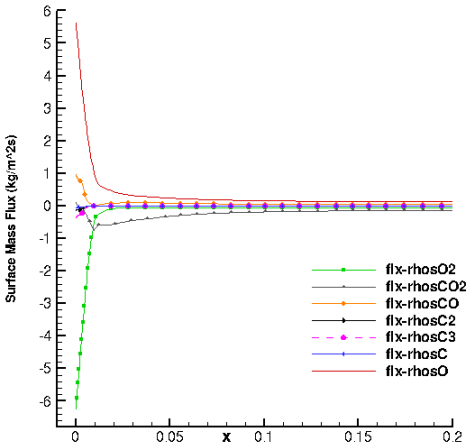

(e) Surface mass flux on ZA with nitridation (Alba) model

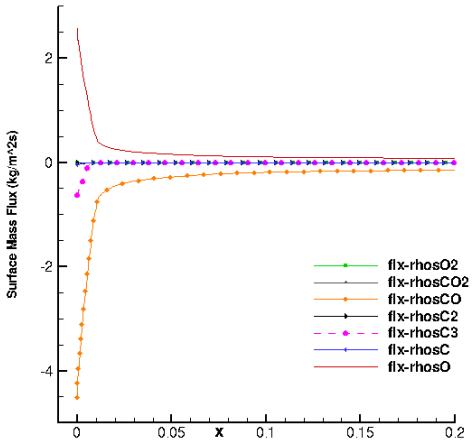

(f) Surface mass flux on MURI model

Figure 6.20. Surface mass flux on blunt cone at V=6000 $\frac{m}{s}$, high density

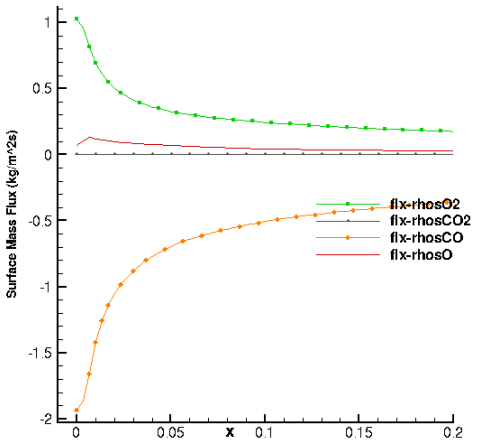

(a) Surface mass flux on Park76 model

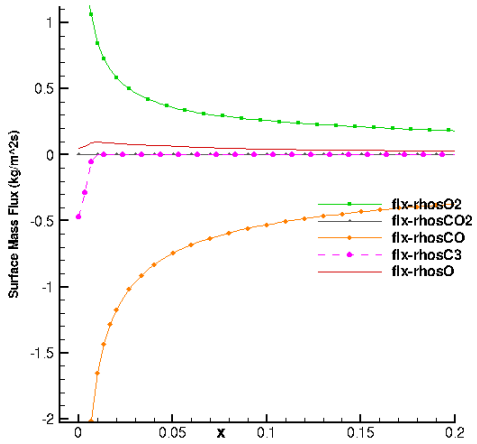

(b) Surface mass flux on Park model

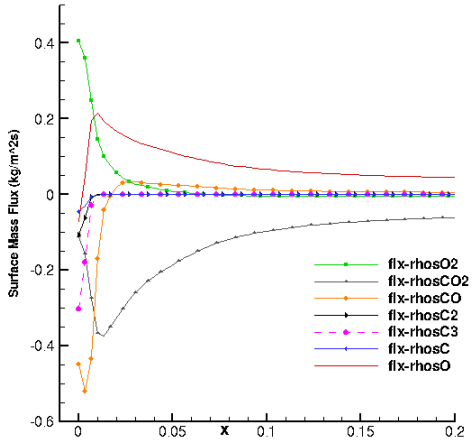

(c) Surface mass flux on ZA model

Figure 6.21. Surface mass flux on sharp cone at V=6000 $\frac{m}{s}$, high density

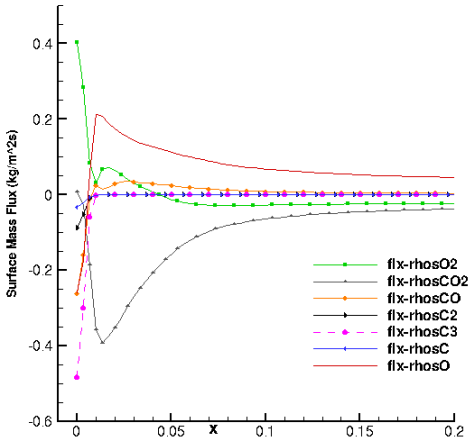

(d) Surface mass flux on MZA model

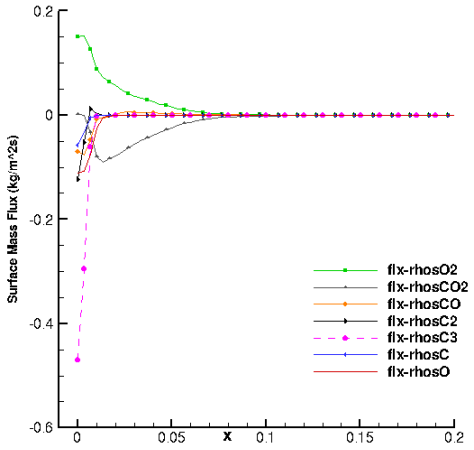

(e) Surface mass flux on ZA with nitridation (Alba) model

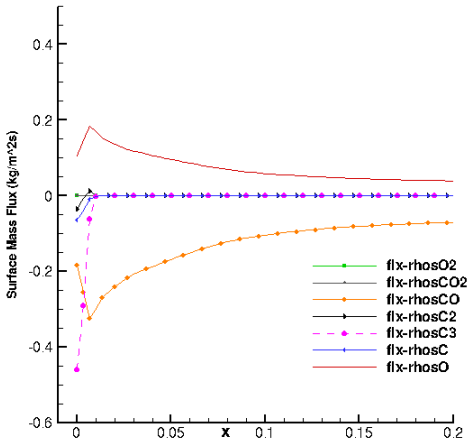

(f) Surface mass flux on MURI model

Figure 6.21. Surface mass flux on sharp cone at V=6000 $\frac{m}{s}$, high density

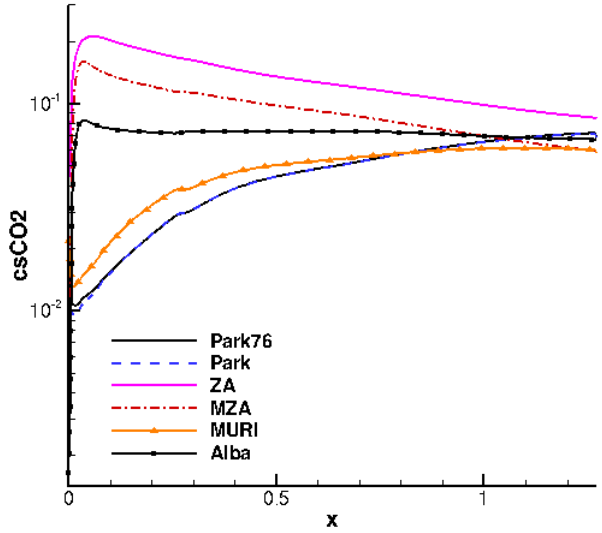

Figure 6.22. CO_2 concentration for blunt cone at V=6000 $\frac{m}{s}$, high density

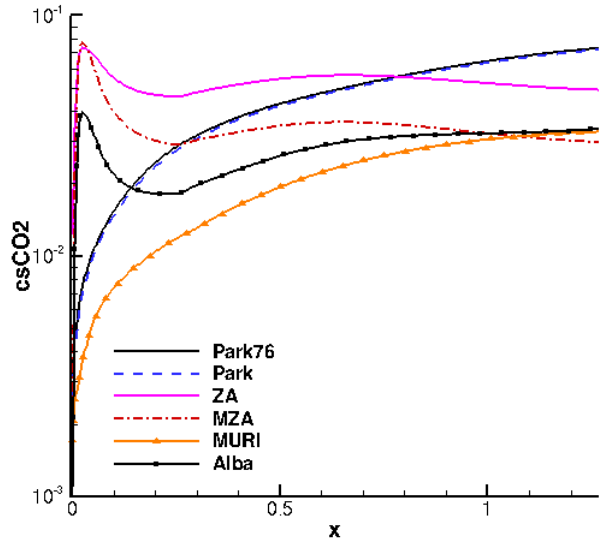

Figure 6.23. CO_2 concentration for sharp cone at V=6000 $\frac{m}{s}$, high density

A comparison of the N factors for all ablation models on the blunt cone is shown in Figure 6.24 and Figure 6.25 for the sharp cone. For the blunt cone, there is a correlation between CO_2 concentration levels and the result boundary layer stability N factor. The no ablation case shows significantly higher N factors than all models containing ablation. The simulations with ablation all show reduced N factors, with the Park, ZA and MURI models, showing the similar stability characteristics. Overall, there is a 0.65 to 0.8 m delay in the start of amplification and a similar delay in transition, if transition occurred at an N factor of 10, clear evidence of CO_2 damping affecting stability and transition characteristics.

For the sharp cone simulations, a correlation between CO_2 concentration and N factor may exist. The simulation with no ablation does show higher amplification rates than any of the flows with CO_2 present. The Park model, which produces marginally more CO_2 than the other models shows a lower N factor, while the MURI, Alba and MZA models, which produce similar CO_2 concentrations, have a higher, but similar, N factor. The no ablation simulation, however, shows less amplification at locations close to the nose tip (body location less than 0.2 m) than do all the simulations with ablation included. This increase in amplification may be due to blowing caused by ablation which has a destabilizing effect on the boundary layer.

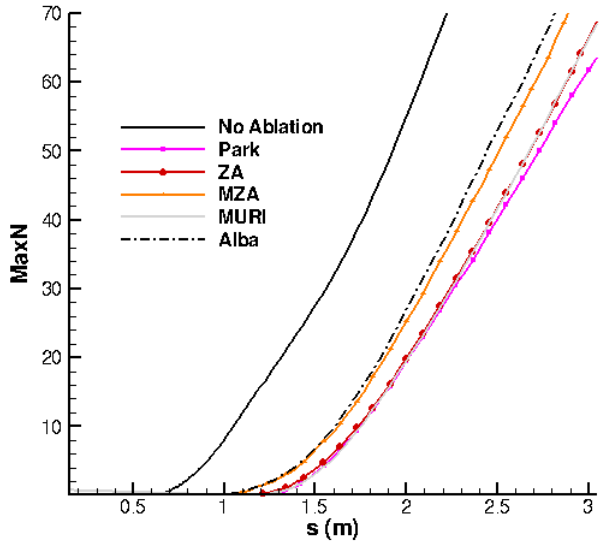

Figure 6.24. Maximum N factors for all ablation models on a blunt cone at V=6000 $\frac{m}{s}$, high density

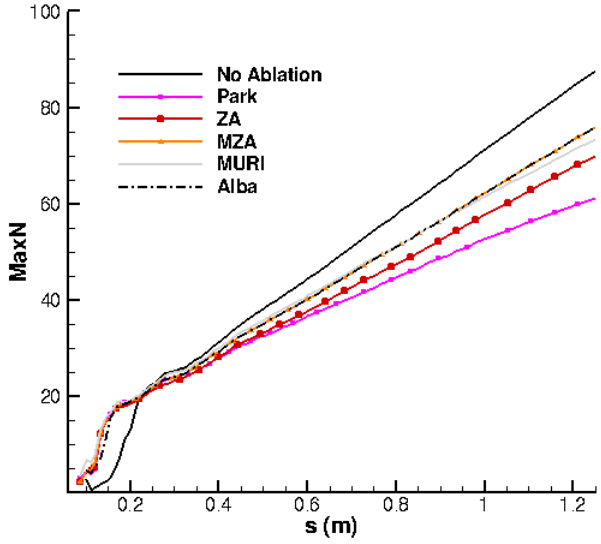

Figure 6.25. Maximum N factors for all ablation models on a sharp cone at V=6000 $\frac{m}{s}$, high density

A frequency analysis of the models for the blunt cone shows a decrease in amplification at the the higher frequencies, 400-700 kHz range) for all ablation models. Figures 6.26a through 6.26c show these frequency analyses results. This damping at the high frequencies result in lower maximum N factors.

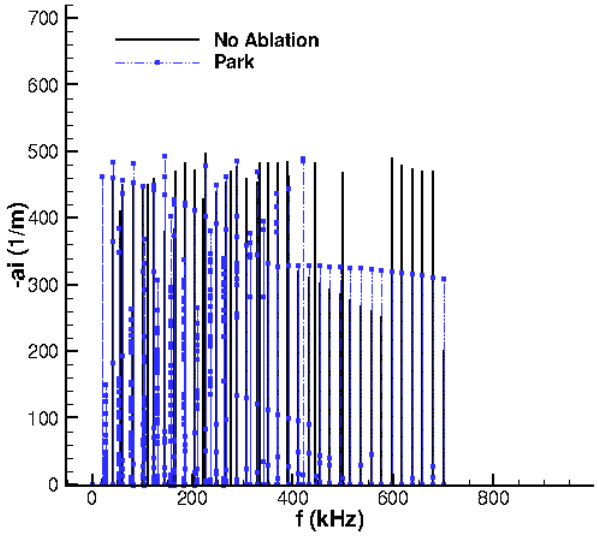

(a) Frequency Comparison with Park model

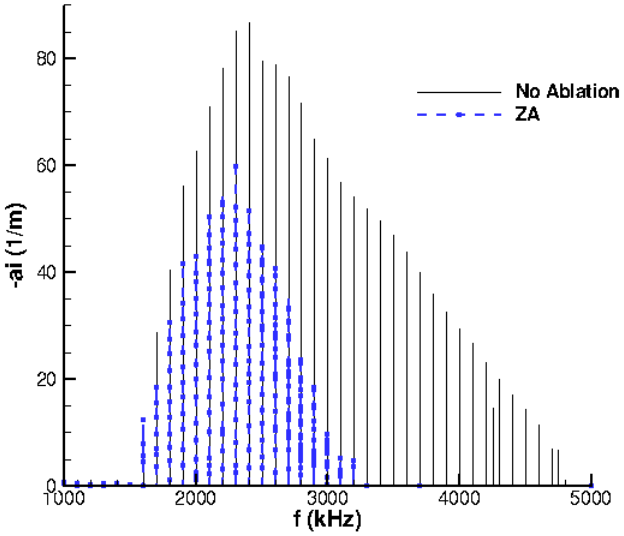

(b) Frequency Comparison with ZA model

Figure 6.26. Frequency Comparison on a blunt cone at V=6000 $\frac{m}{s}$, high density

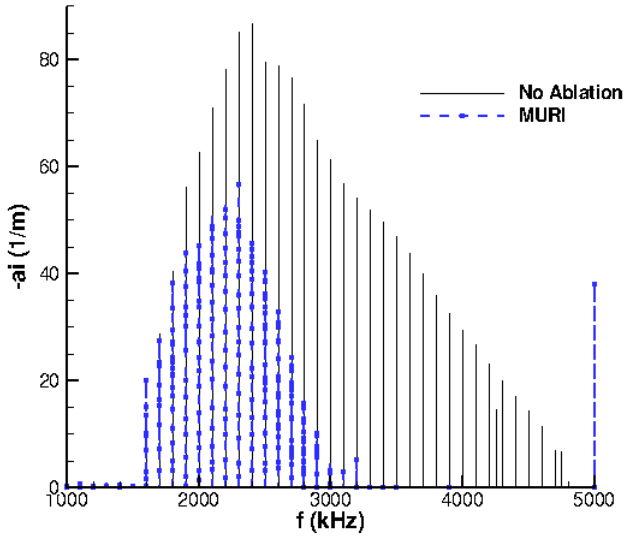

(c) Frequency Comparison with MURI model

Figure 6.26. Frequency Comparison on a blunt cone at V=6000 $\frac{m}{s}$, high density

Given the N factor results of the sharp cone at these conditions, a frequency analysis should show decreased amplification when CO_2 is present and vibrational modes are enabled. Figures 6.27a through 6.27c show the amplification per frequency for on the sharp cone simulations but do not show a significant decrease in amplification with the ablation model simulations as compared to the simulation with no CO_2 in the flow. However, examining the Park model closely, between the frequencies of 2-5 MHz, a slight reduction in the amplification is seen (per Figure 6.27d). These frequencies are amplified over long streamwise distance as is shown by the stability diagram, Figure 6.28, where a small amount of damping would produce a larger N factor effect.

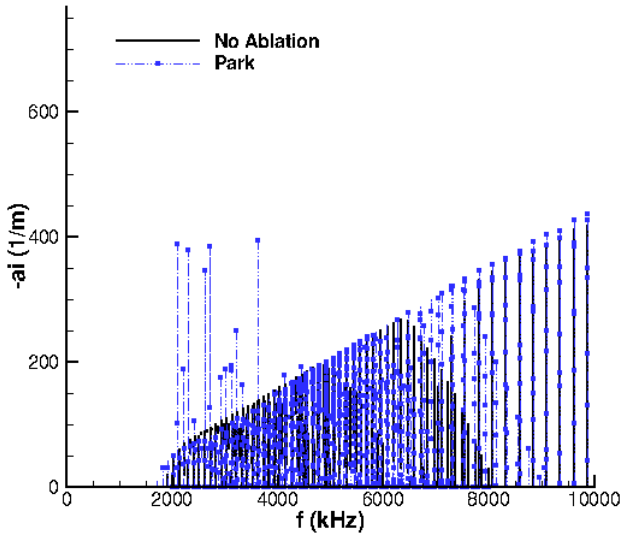

(a) Frequency Comparison with Park model

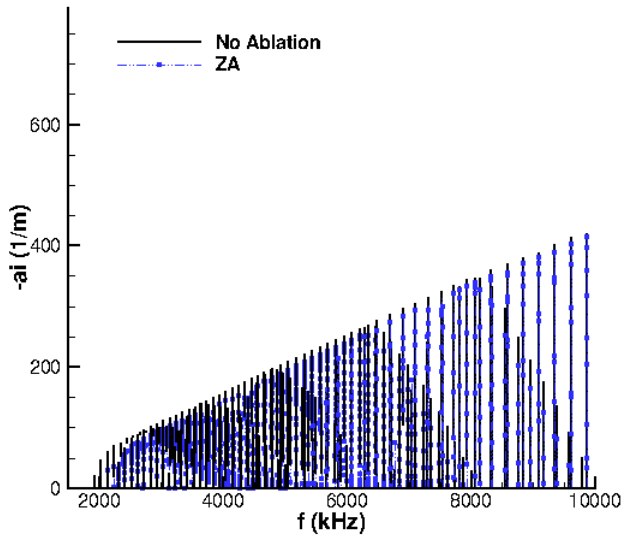

(b) Frequency comparison with ZA model

Figure 6.27. Frequency Comparison on a sharp cone at V=6000 $\frac{m}{s}$, high density

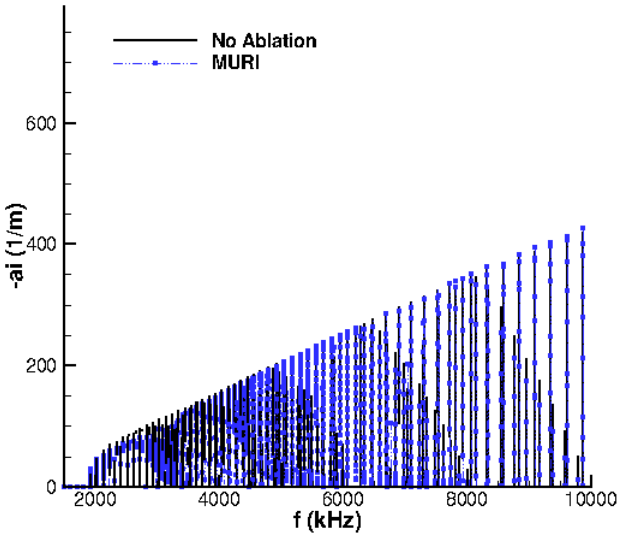

(c) Frequency comparison with MURI model

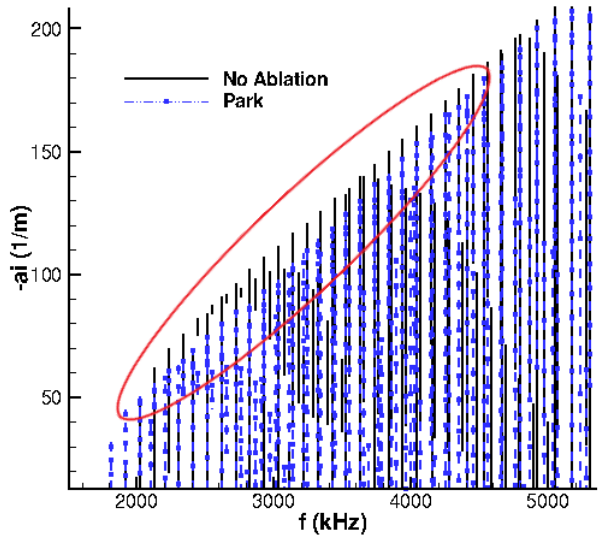

(d) Frequency comparison with Park model

Figure 6.27. Frequency Comparison on a sharp cone at V=6000 $\frac{m}{s}$, high density

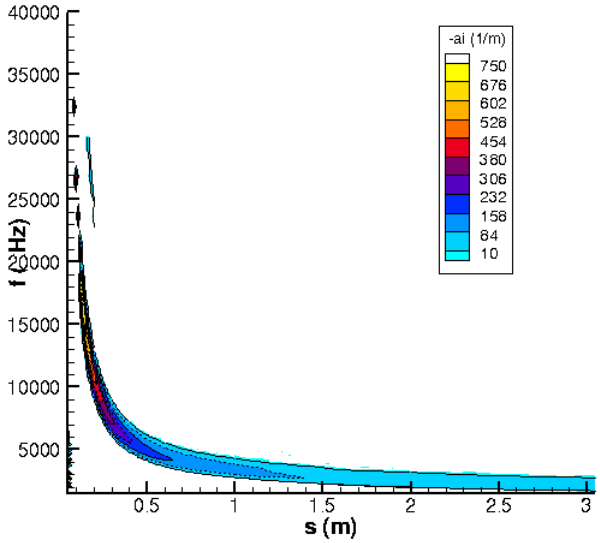

Figure 6.28. Stability diagram for a sharp cone at V=6000 $\frac{m}{s}$, high density

6.2.2 Low Enthalpy Flow - $V_\infty = 3000\frac{m}{s}$, total enthalpy $= 5.0\frac{MJ}{kg}$.

The maximum CO_2 concentrations on the blunt and sharp cones at the high density, low enthalpy simulations are shown in Figures 6.29 and 6.30. For both geometries, the maximum concentration of CO_2 in the boundary layer is less than 10%, than those seen at the high enthalpy cases in both the low and high density simulations. Given this low concentration of CO_2, no correlation between the CO_2 concentration levels and the boundary layer stability results were expected. This lack of correlation can be see in Figures 6.31 and 6.32. This result would further suggest that at these small concentrations, and with the decreasing concentration down the body, CO_2 damping did not affect the overall stability of the boundary layer.

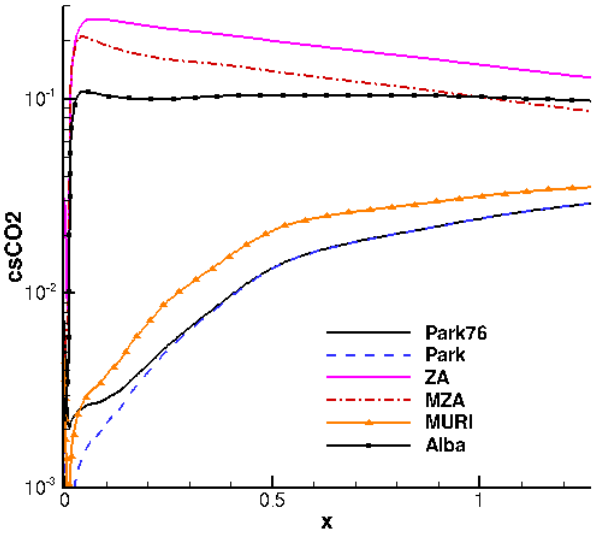

Figure 6.29. CO_2 concentration for blunt cone at V=3000 $\frac{m}{s}$, high density

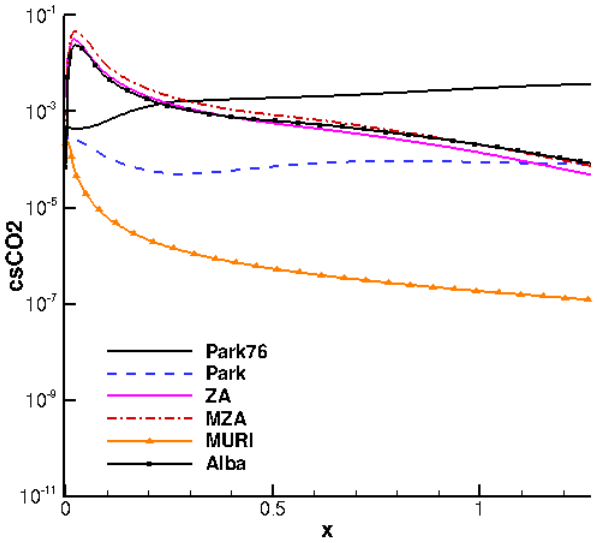

Figure 6.30. CO_2 concentration for sharp cone at V=3000 $\frac{m}{s}$, high density

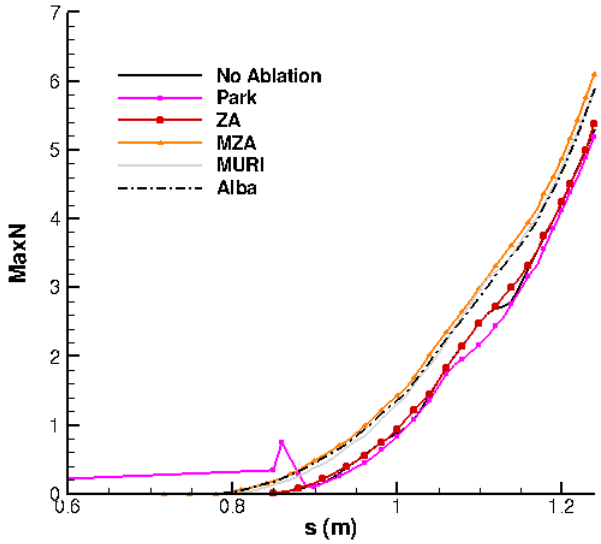

Figure 6.31. Maximum N factor for a blunt cone at V=3000 $\frac{m}{s}$, high density

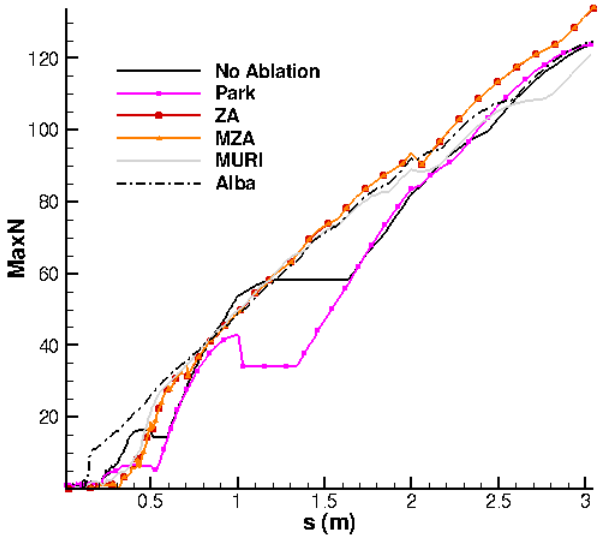

Figure 6.32. Maximum N factor for sharp cone at V=3000 $\frac{m}{s}$, high density

An analysis of the amplification per frequency on both the blunt and sharp cone models is given by Figures 6.33a through 6.34c. There is no trend of amplification reduction at higher frequencies on any of the ablation simulations.

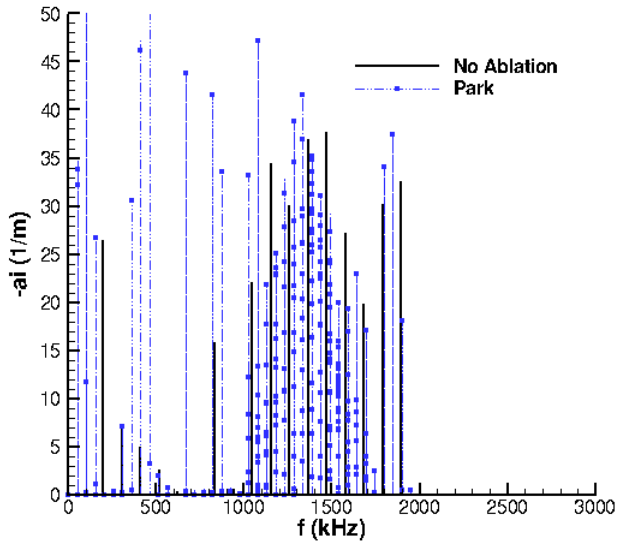

(a) Frequency Comparison with Park model

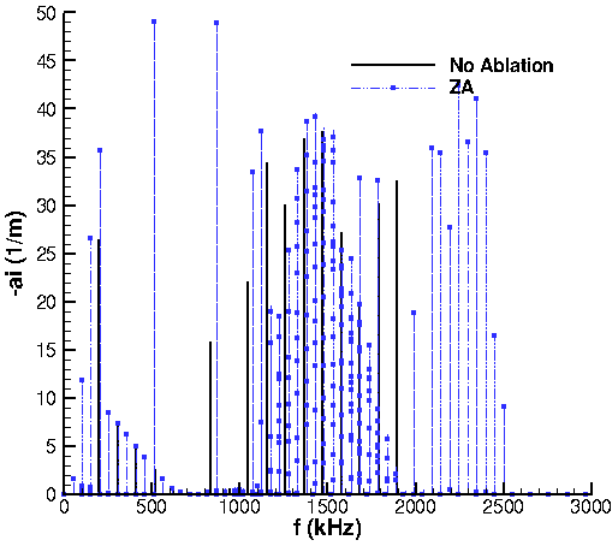

(b) Frequency Comparison with ZA model

Figure 6.33. Frequency Comparison on a blunt cone at V=3000 $\frac{m}{s}$, high density

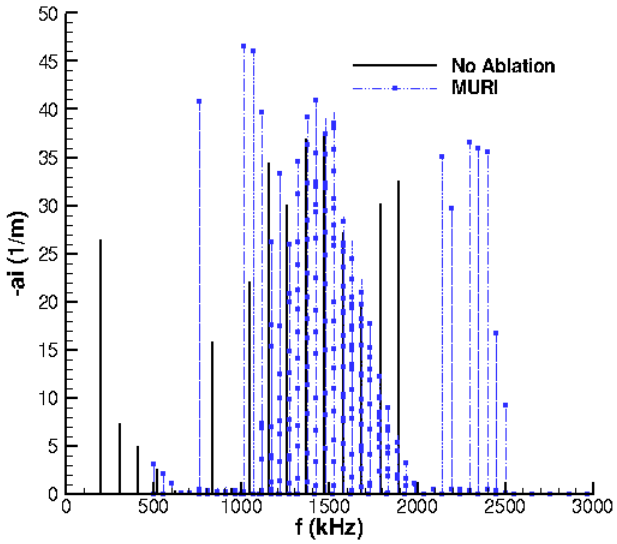

(c) Frequency Comparison with MURI model

Figure 6.33. Frequency Comparison on a blunt cone at V=3000 $\frac{m}{s}$, high density

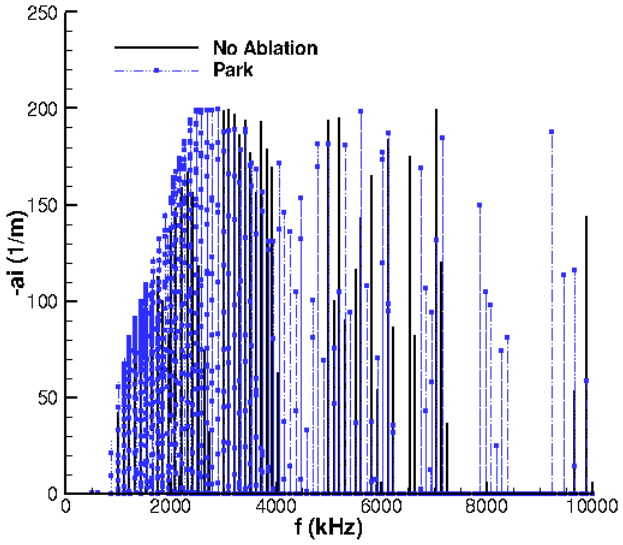

(a) Frequency Comparison with Park model

Figure 6.34. Frequency Comparison on a sharp cone at V=3000 $\frac{m}{s}$, high density

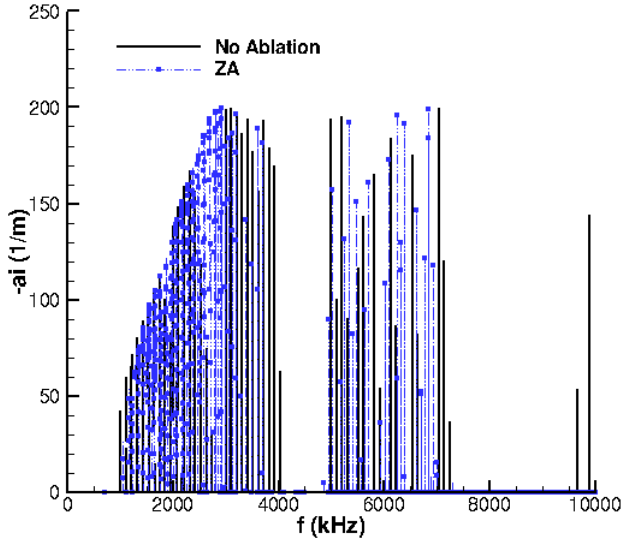

(b) Frequency Comparison with ZA model

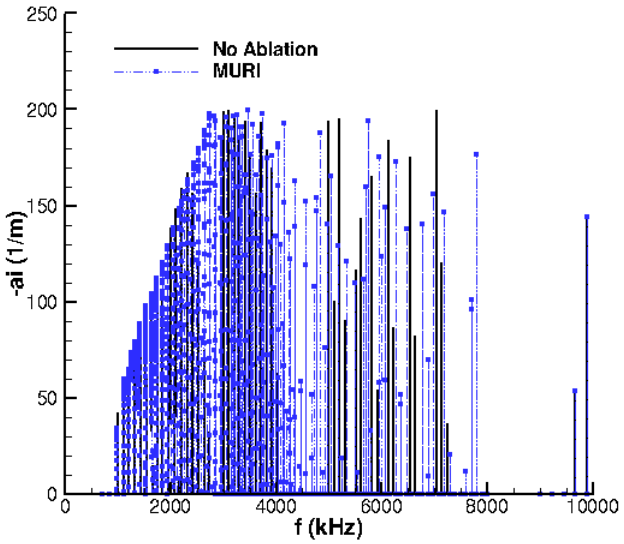

(c) Frequency Comparison with MURI model

Figure 6.34. Frequency Comparison on a sharp cone at V=3000 $\frac{m}{s}$, high density

For all conditions surveyed, only the sharp cone model at the high density and enthalpy flow conditions exhibited any amplification reduction due to CO_2 damping. At the lower density conditions, the concentration of CO_2 in the boundary layer on either the sharp or blunt geometry was less than 10%. The N factors at the low density conditions for all simulations never exceeded a value of 8, which is a very low total amplification and would not signify a boundary layer approaching transition. The low concentration of CO_2 coupled with the overall low amplification values at the low density flow conditions, did not show any effect of CO_2 damping on the boundary layer stability. The higher density flow conditions produced greater concentrations of CO_2 on both the blunt and sharp cones. For the blunt cone, a minimum concentration of approximately 8% CO_2 was achieved for all ablation models at all body locations. Based on the CO_2 concentration study, this concentration should be high enough to show a significant reduction of high frequency amplification. However, the high level on noise in the stability results did not allow for a proper comparison. Also at these flow conditions, the sharp cone model, which had minimum of approximately 5% CO_2 concentration along the body, did show a reduction in the total N factor where CO_2 was present as compared to the no ablation stability results.

6.3 Parameter Study

6.3.1 Model Sensitivity to Site Density.

For all the ablation models used except for the two Park models, a reaction limiting factor was used known as the site density. The site density is a material based property that determines the number of open sites on the surface of the body that are available for adsorption of O or N atoms. The site density value is conserved in the model such that the total number of sites per iteration is constant, while the number of empty sites and those occupied by an N or O atom vary based on the reaction rates. This

parameter sets a limit on the total number of atoms that can be adsorbed on the surface and thus a limit on the surface reactions. All simulations for this parameter study were conducted on the 12.7 mm nose radius cone model at a freestream density of 0.4583 $\frac{kg}{m^3}$, a T and T_v of 238.6 K and a freestream velocity of 6000 $]fracms.$

Previous research on the material properties of graphite show that the site density values $2.1x10^{19}\frac{1}{m^2}$ and $5.8x10^{15}\frac{1}{m^2}$ [110, 60]. The total site density parameter values is affected mainly by the purity of the sample and the average number of defects [60]. This site density translates to a total active site density of between approximately $1x10^{-8}\frac{mol}{m^2}$ and $1x10^{-5}\frac{mol}{m^2}$. The first value was used as the original site density value used in the rate determination constants for the ZA, MZA, and MURI models [14, 16]. Candler et al. accomplished a site density sensitivity analysis for the ZA model but varied site density values by less than a factor of ten, which showed no model sensitivity [102]. However, if the site density is varied between $10^{-8}\frac{mol}{m^2}$ and $10^{-5}\frac{mol}{m^2}$ there is a significant change. Similarly, if the site density is varied to higher rates, simulating both defects or fibers, which increase site density by increasing the total surface area, or by lower rates, simulating highly-organized carbon materials, the sensitivity to this parameter changes. Figures 6.35 through 6.39 show the results of CO_2 concentration by varying only the site density parameter.

The original implementation of the ZA model shows a relative insensitivity to site density parameter values close to the design parameter, but when that site density is either increased or decreased, the production of CO_2 decreases dramatically (see Figure 6.35). The concentrations are represented by a log scale due to the large variation in concentrations based on the site density parameter. This decrease is the due to the desorption reaction not being included as well as the lack of mobile site coefficient. The rate coefficients determined by Zhluktov and Abe in the original model was based on the inclusion of a mobile site coefficient which allows adsorbed

atoms the ability to move sites on the surface [14]. This mobility allows adsorbed atoms to vacate sites near the nose of the cone where a high density of O and N atoms are present allowing for more atoms to be adsorbed and allowing for a greater production of CO and CO_2 molecules where sublimation reactions are not dominant. Without that mobile ability, increasing the site density causes more O and N atoms to be adsorbed at the nose of the cone but decreases the number of atoms available for adsorption further down the cone and for collisions to produce CO and CO_2. The lack of the desorption reactions would cause possible saturation of the active sites when the site density is low, limiting the total surface reaction production of CO and CO_2. Given theses limitations on the ZA model, as the site density is decreased, fewer total ablation products are produced as few O atoms are adsorbed and available for CO_2 reactions. Also, as the site density is increased from the design value, the production of CO_2 also decreases significantly after the nose of the cone. This decrease is not seen in the MZA model (see Figure 6.36) and would be the result of the immobility of the sites. At the nose, the larger available sites allow for more adsorption where the CO_2 concentration is similar to the design conditions. However, farther downstream along the cone, the production of CO_2 is limited, most likely from fewer O atoms available to create CO_2 from reaction 7 of the ZA model leaving the production of CO_2 only to reaction 8 as given in Table 3.4.

The addition of the mobile site parameter and the desorption reactions for the MZA model significantly change model sensitivity to the site density parameter. Figure 6.36 show the CO_2 concentrations for changing site densities for the MZA model. As the number of sites are decreased, which decreased the production of CO_2 in the ZA model, there is a relative insensitivity in the MZA model. This is most likely caused by the ability for the sites to be mobile in the MZA model, so as the sites at the nose become saturated, the O atoms are allowed to diffuse back along the body to

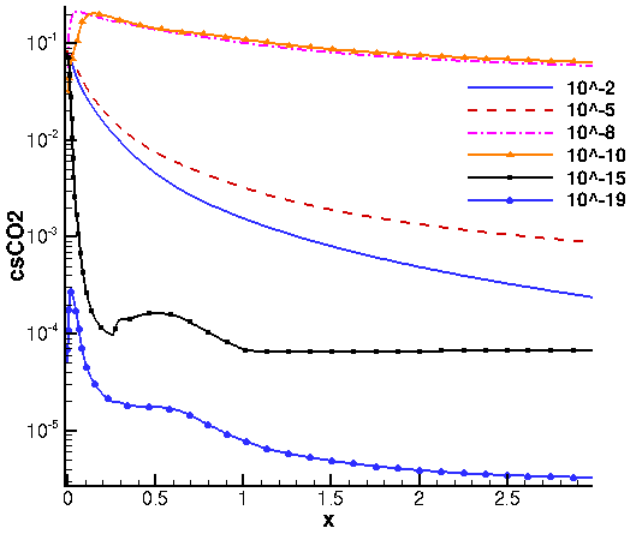

Figure 6.35. Concentration of CO_2 for the ZA model based on varying site density parameter, V= 6000 $\frac{m}{s}$, high density

other sites, allowing for an increased number of site available for the CO_2 reactions. Also, the inclusion of the desorption reaction allows for O atoms to desorb as well as adsorb making saturation less likely. As the site density is increased, however, there is a significant increase in the production of CO_2.

Examining the fluxes of O, O_2 , CO and CO_2 between the ZA and MZA models at a site density of $1x10^{-2}\frac{mol}{m^2}$, there is a marked difference between the two models caused by the mobile site and desorption reaction inclusion. There is nearly twice as much adsorption of O atoms for the ZA model over the MZA model (see Figure 6.37d. The MZA model shows a small adsorption of O_2 while the ZA model shows a high flux of O_2 from the surface shown in Figure 6.37c. Similarly, the MZA and ZA models produce opposite fluxes at the nose for both CO and CO_2. Whereas the ZA model shows a high production of CO_2 which decreases to zero at a body location of 0.1 m, the MZA models produces a small consumption of CO_2 at the nose, but then a small production consistently down the body as given by Figure 6.37a. The flux of CO shows an opposite reaction where a large amount of CO is produced at the nose for

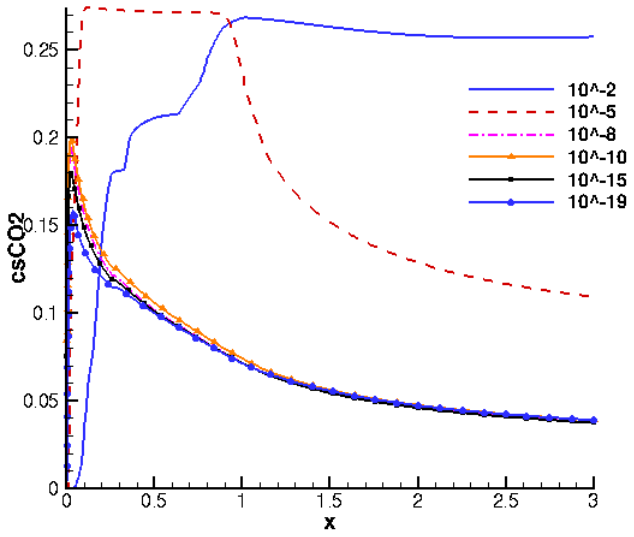

Figure 6.36. Concentration of CO_2 for the MZA model based on varying site density parameter, V= 6000 $\frac{m}{s}$, high density

the MZA model, but an opposite flux occurs for the ZA model (shown in Figure 6.37b. Very similar flux results happen when the site density is set at $1x10^{-5}\frac{mol}{m^2}$. However, when the site density is reduced to $1x10^{-15}\frac{mol}{m^2}$, two models behave very differently. While the flux of O and O_2 remains relatively the same, the production of CO and CO_2 now match direction, with the ZA model producing significantly more of each than the MZA model. These flux results are shown in Figures 6.37a through 6.38d. The complexity of the model results to changing site density most likely is derived from the empirical nature of the model itself and the fact that the rates determined in the model were based on the assumption of a site density [14].

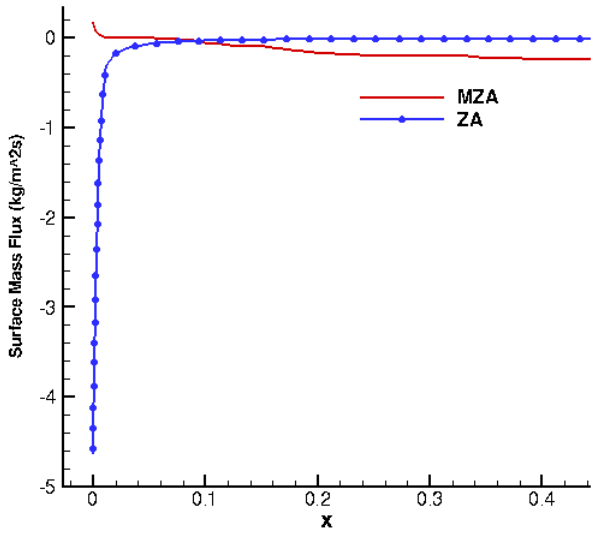

(a) Surface mass flux of CO_2 on ZA and MZA models

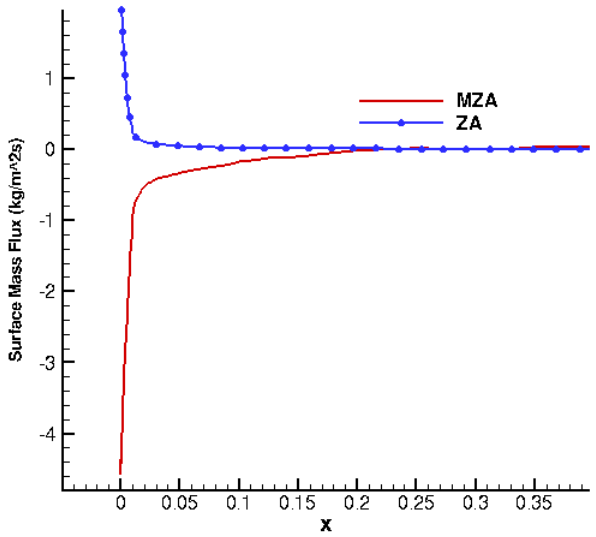

(b) Surface mass flux of CO on ZA and MZA models

Figure 6.37. Surface mass flux on ZA and MZA models at site density parameter of $1x10^{-2}\frac{mol}{m^2}$

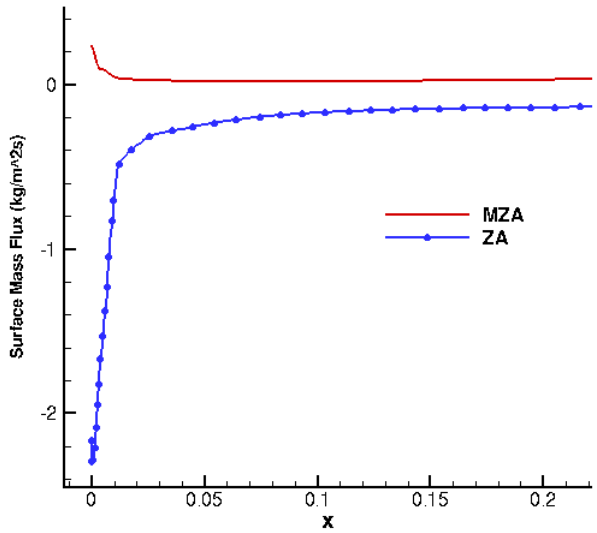

(c) Surface mass flux of O_2 on ZA and MZA models

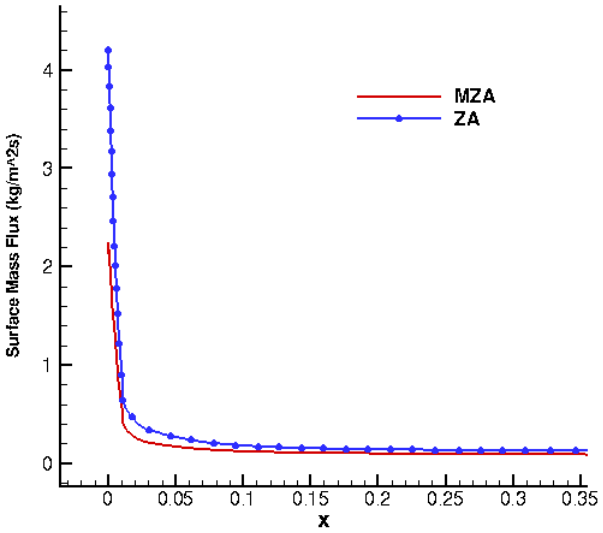

(d) Surface mass flux of O on ZA and MZA models

Figure 6.37. Surface mass flux on ZA and MZA models at site density parameter of $1x10^{-2}\frac{mol}{m^2}$

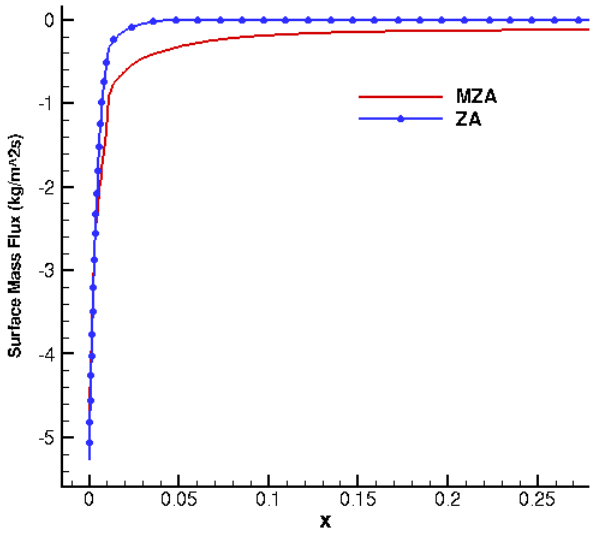

(a) Surface mass flux of CO_2 on ZA and MZA models

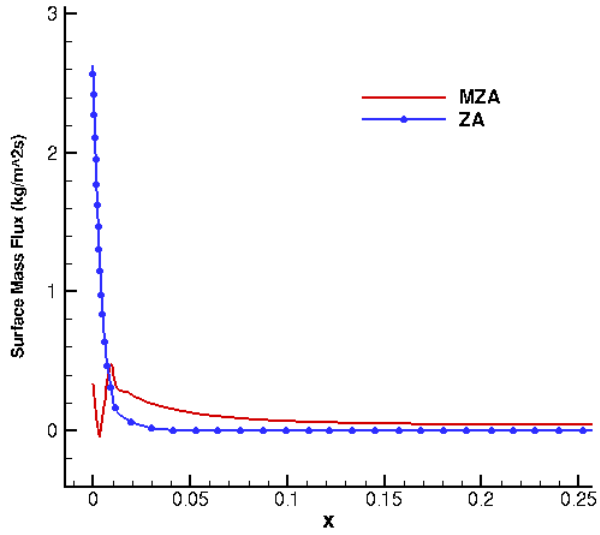

(b) Surface mass flux of CO on ZA and MZA models

Figure 6.38. Surface mass flux on ZA and MZA models at site density parameter of $1x10^{-15}\frac{mol}{m^2}$

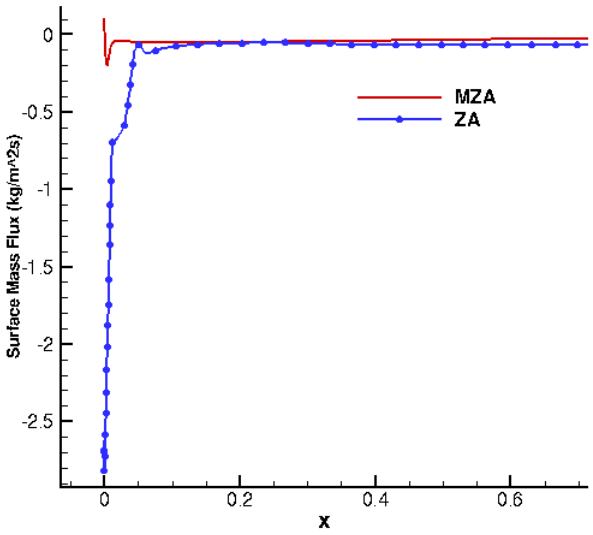

(c) Surface mass flux of O_2 on ZA and MZA models

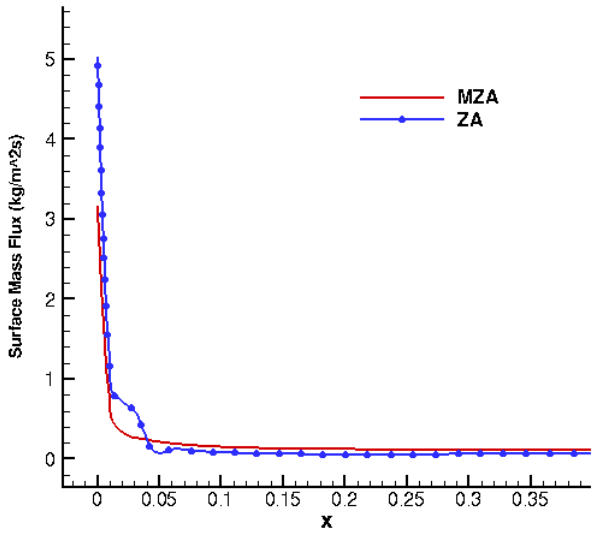

(d) Surface mass flux of O on ZA and MZA models

Figure 6.38. Surface mass flux on ZA and MZA models at site density parameter of $1x10^{-15}\frac{mol}{m^2}$

The MURI model remains relatively insensitive to the site density parameter in CO_2 production (see Figure 6.39). When the site density is decreased, there is not change in the total concentration of CO_2 in the flow. There is a reduction in the total concentration of CO_2 when the site density is increased, the model favors the adsorption of O atoms and the production of CO over CO_2 as is shown in Figure 6.39b. The overall change in CO_2 concentration, however, is minimal compared to the differences in the ZA and MZA models. This difference may be caused by the fact that the rates were experimentally determined from a single set of experiments and less dependent on the assumptions made on material property constants.

Overall, the ZA and MZA models are very sensitive to the site density parameter both between the Duffa and Blytholder values as well as for greater variation. However, the concentration of CO_2 decreased in all cases except for when the site density was increased for the MZA model. As there was a significant increase in the concentration of CO_2 at these larger site densities, there may be an impact on the overall boundary layer stability. Figure 6.40 compares the stability analysis results for the MZA model. Examining the N factor results for the original site density of $1x10^{-8}\frac{mol}{m^2}$ for the MZA model compared to other site densities, decreased site density has little impact on the overall N factor values, changing the total transition location approximately 12 cm. Since the total concentration of CO_2 changes very little with a decrease in the site density parameter limited impact on the stability characteristics would be expected. However, at a site density of $10^{-5}\frac{mol}{m^2}$, where the CO_2 concentration is higher until approximately 1 m along the body and then decreases significantly compared to the $10^{-2}\frac{mol}{m^2}$, the maximum N factor remain below the higher site density. Figures 6.41a through 6.42b show the stability diagrams for both the $10^{-5}\frac{mol}{m^2}$ and $10^{-2}\frac{mol}{m^2}$ site density values with vibrational modes enabled and disabled. From these stability diagrams it is clear that the high concentrations of CO_2 in the flow

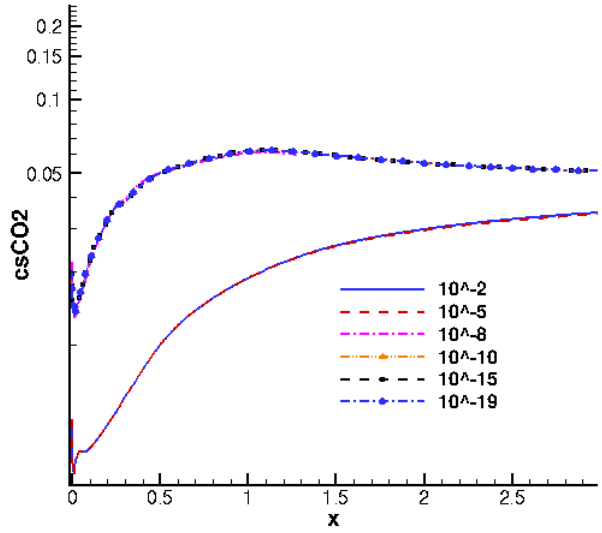

(a) Concentration of CO_2 for the MURI model

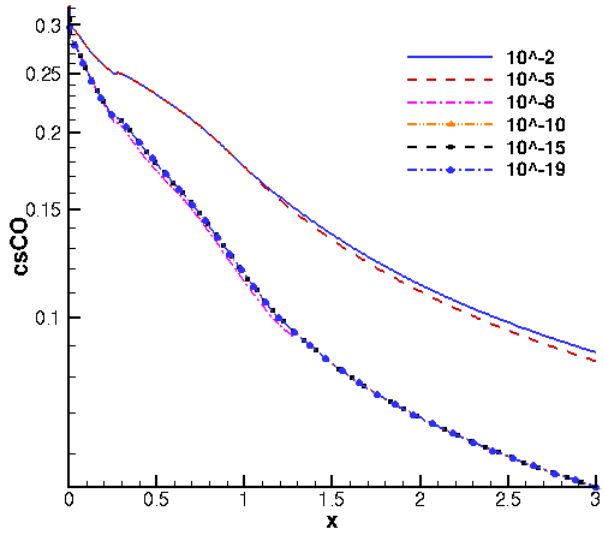

(b) Concentration of CO for the MURI model

Figure 6.39. Concentrations for the MURI model based on varying site density parameter, V= 6000 $\frac{m}{s}$, high density

dampen out all instability at x locations less than approximately 1 m where the CO_2 concentrations begin to decrease. However, past this x location, the $10^{-2}\frac{mol}{m^2}$ shows greater amplification despite having higher concentrations of CO_2 in the flow yet has slightly higher amplification that the $10^{-5}\frac{mol}{m^2}$ results. If the amplification per frequency between these two site density simulations are evaluated, the $10^{-5}\frac{mol}{m^2}$ shows lower amplification at frequencies greater than 2 MHz, which would account for the lower N factor results, as is also seen in the stability diagram. Why this increased amplification occurs is not explained by CO_2 damping nor evident from the frequency analysis. The mechanism that is causing this could be the destabilizing blowing effect. Further simulations would need to be conducted to determine the source of the instability.

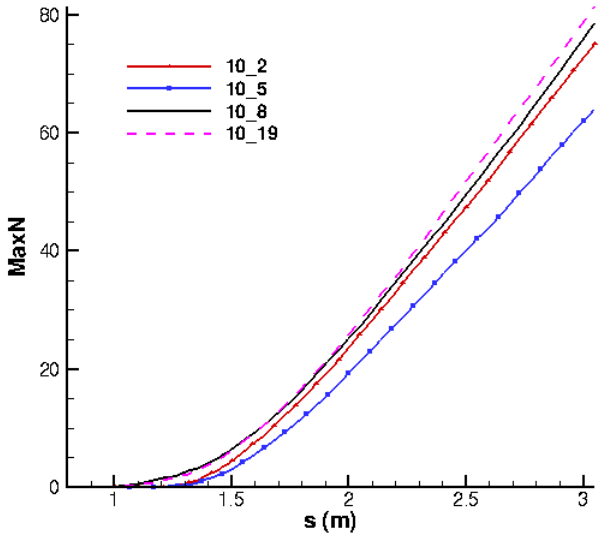

Figure 6.40. Maximum N factors for MZA model with site density variations

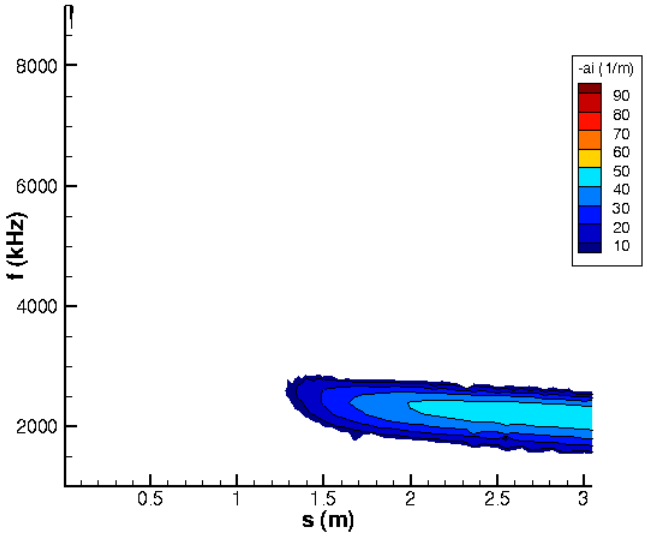

(a) Maximum N factors for MZA model with vibrational modes enabled

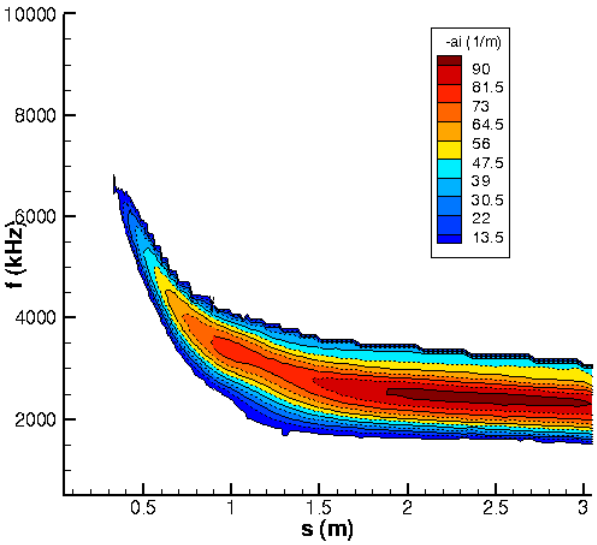

(b) Maximum N factors for MZA model with vibrational modes disabled

Figure 6.41. Maximum N factors for MZA model with site density $10^{-5}\frac{mol}{m^2}$ with vibrational modes enabled (a) and disabled (b)

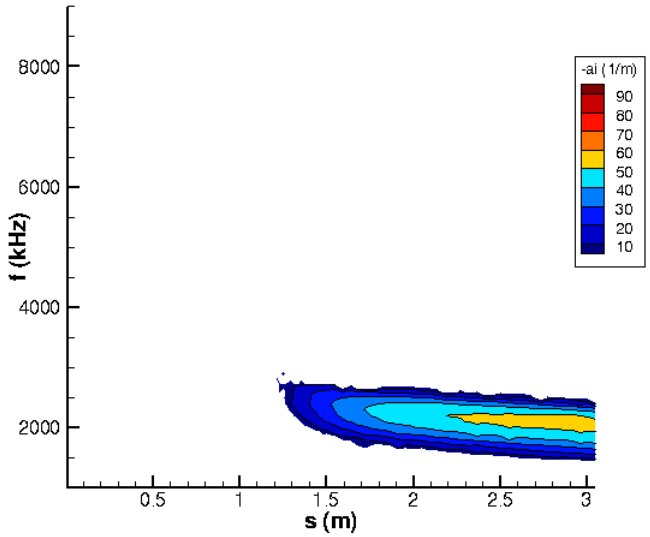

(a) Maximum N factors for MZA model with vibrational modes enabled

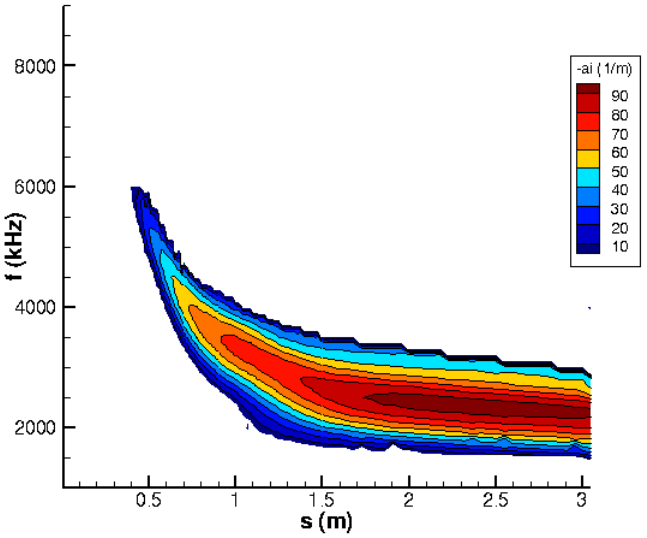

(b) Maximum N factors for MZA model with vibrational modes disabled

Figure 6.42. Maximum N factors for MZA model with site density $10^{-2}\frac{mol}{m^2}$ with vibrational modes enabled (a) and disabled (b)

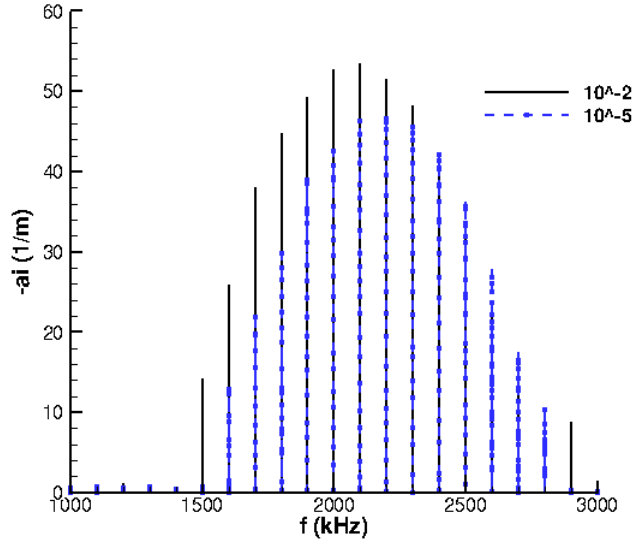

Figure 6.43. Frequency analysis of amplified frequencies at $10^{-2}\frac{mol}{m^2}$ and $10^{-5}\frac{mol}{m^2}$ site density for the MZA model

6.3.2 Model Sensitivity to Surface Temperature.

As was referenced in Chapter 2, the surface temperature not only affects the stability of the boundary layer, but also the reaction types and production rates of the ablative species. In hypersonic flow, an increasing surface temperature increases the stability of the second mode instabilities [12]. Bitter et al. showed that the increasing surface temperature, relative to the freestream temperature, destabilizes first mode instabilities but stabilizes second mode instabilities. The impact of increased surface temperature will also affect the production of different ablative species. Per each ablation model, the temperature of the surface and near surface gas environment favors certain reactions over others. For example, near a surface temperature of 3800 K, the sublimation temperature of graphite, the production of C, C_2 and C_3 are favored over the adsorption of either O or N atoms [61]. Similarly, the creation of CO versus CO_2 is temperature dependent at both the surface and the near surface gas environment as CO_2 production is the favored reaction at temperatures below 3000 K whereas CO production is favored above that temperature [79]. Therefore, the surface temperature is a significant factor when determining the ablation reactions and changes in this temperature would change the total concentrations of the different species.

A sensitivity study, examining the changes in CO_2 concentration and the resulting effect on boundary layer stability was conducted. Only the Park, MZA and MURI models were used in this study. The original implementation of the ZA model is know to overproduce CO_2 due to the lack of mobile site parameter and the desorption reactions not being included [102] and was not included due to this known error. Similarly, the Park76 model was not included due to the lack of sublimation reaction in this model. The surface temperature was increased by 1.5, 2.0 and 2.5 times of the surface temperature model used in the ablation model comparison and the blunt cone

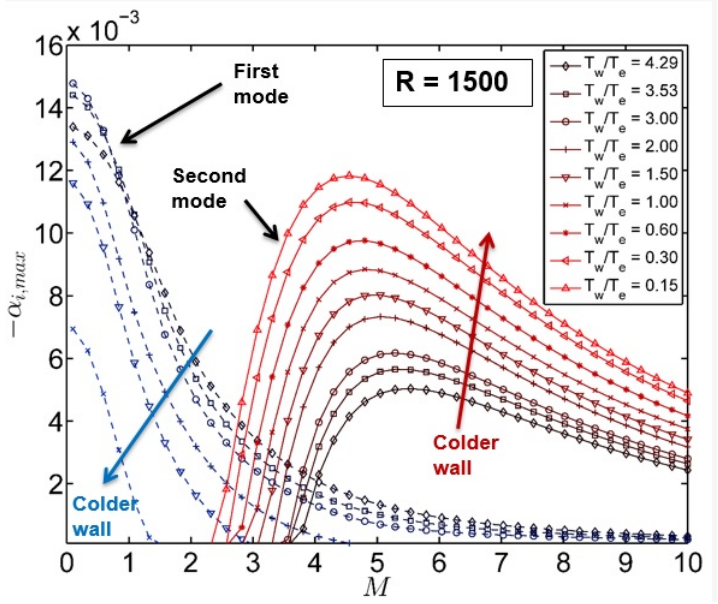

Figure 6.44. Surface temperature effects on the first and second mode instabilities [12] (with permission)

geometry was used. When the surface temperature exceeded 4000 K, the sublimation temperature of graphite, the temperature was limited to 4000 K [61]. The freestream conditions used were the same as the high density, high enthalpy flow conditions for the ablation model study.

The effect of species production for the Park model is shown in Figures 6.45a through 6.45c show the maximum ablative species concentrations along the cone. At the nose of the cone, especially at the higher temperatures, C_3 is the produced at high relative concentrations but decreases back to negligible concentrations as the surface temperature decreases. The relationship between the production of CO versus CO_2 in this model is shown in Figures 6.45a and 6.45b. As the concentration of CO begins to decrease due to lower temperatures along the body, the concentrations of CO_2 increase. For the Park model, as the surface temperature increases, the overall concentration of CO_2 decreases while the concentration of CO increases, as the favored reaction.

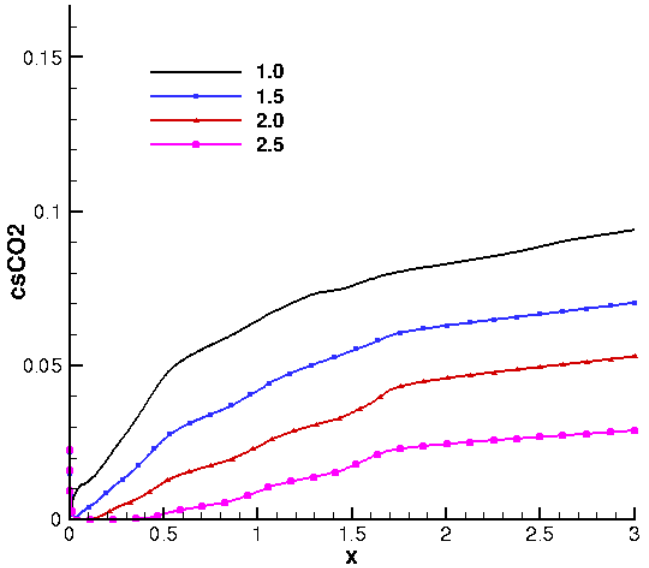

(a) Maximum concentration of CO_2 with Park model

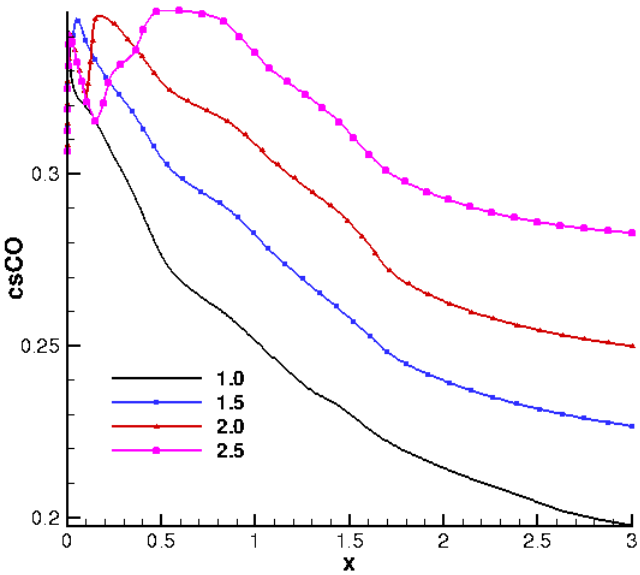

(b) Maximum concentration of CO with Park model

Figure 6.45. Maximum species concentrations with Park model at varying temperatures, V= 6000 $\frac{m}{s}$, high density

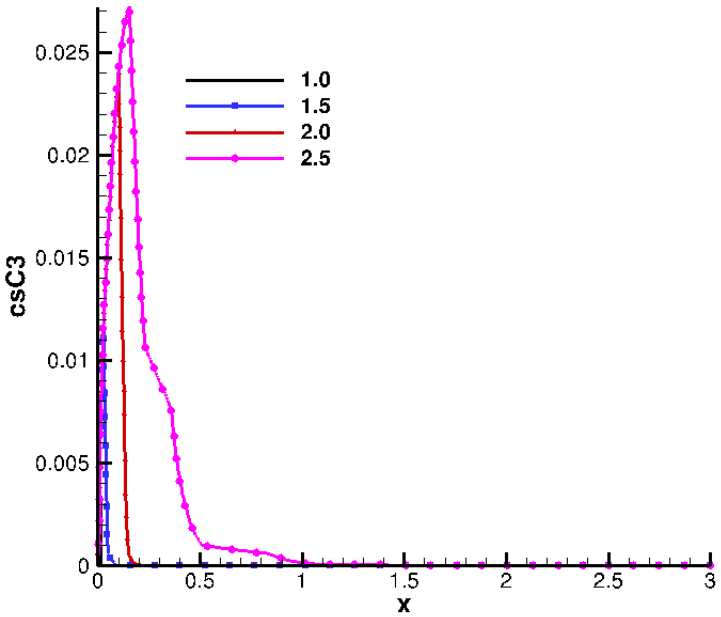

(c) Maximum concentration of C_3 with Park model

Figure 6.45. Maximum species concentrations with Park model at varying temperatures, V= 6000 $\frac{m}{s}$, high density

The results for species production at the same conditions for the MZA model are shown in Figures 6.46a through 6.46e. For the MZA model, the production at the nose of the cone is dominated by not only sublimation of C_3 but also C_2 and C, however, produces less total sublimation products than the Park model. Whereas the Park model favored the production of CO over CO_2 throughout the flow, the MZA model favors CO_2. The same trend is seen in the MZA model as with the Park model where the production of CO and CO_2, vary inversely to each other. In the MZA model, however, the production of CO_2 is favored at a higher temperature and so the concentration increases more rapidly and to a higher value as it becomes the preferred reaction. Unlike the Park model, where increased surface temperature decreased the overall concentration of CO_2 in the flow, the MZA model produces nearly the same maximum concentration. At the lower surface temperatures, 1.0 and 1.5, the concentration of CO_2 spikes near the nose, inversely to the production of both

CO and C_3. At the higher temperatures, 2.0 and 2.5, the maximum concentration reaches a similar amount of around 15%, but maintains the higher concentration for more of the cone length. It also has a slower exponential decrease as compared to the lower temperatures environments. However, as the surface temperature continues to increase, especially at 2.5 times the original value, the MZA model favors the production of CO for longer and the maximum concentration of CO_2 remains below that of the lower surface temperatures. Of the surface temperatures examined, 2.0 times the original value produces the highest concentration of CO_2 in the flow a greater portion of the cone length. Thus simply increasing the surface temperature to higher values will not continue to produce high concentrations of CO_2. As the blunt cone exhibits amplification towards the last half of the cone length due to the entropy layer, this increased concentration of CO_2 should produce greater damping effects.

Similar to the MZA model, the MURI model will produce all 5 of the carbonaceous ablation species. Figures 6.47a through 6.47d show the concentration of each ablative species at the different surface temperatures. The results of the MURI model are very similar in both trend and maximum concentration values as the Park model. While the MZA model produced less sublimation products than the Park model, the MURI model favors sublimation and produces higher concentrations of C_3 at the nose. The maximum concentration of CO_2 in the flow for the MURI model is approximately 5-8%, similar to the Park model results, and as the surface temperature increases, the formation of CO becomes the favored reaction and the production of CO_2 decreases.

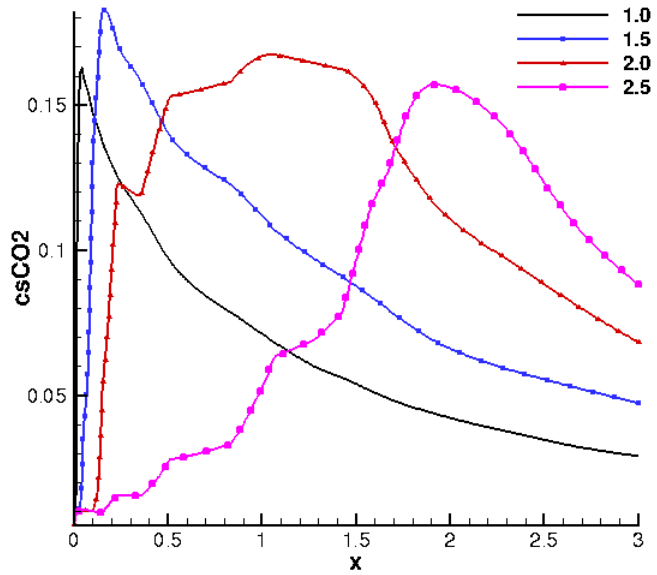

(a) Maximum concentration of CO_2 with MZA model

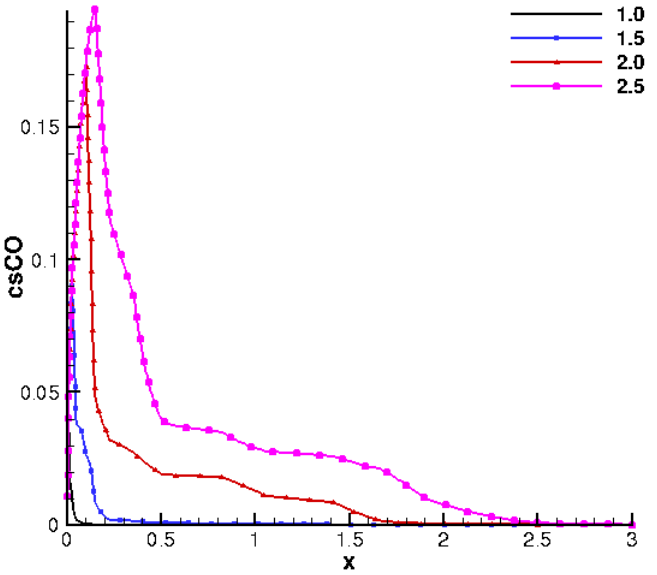

(b) Maximum concentration of CO with MZA model

Figure 6.46. Maximum species concentrations with MZA model at varying temperatures, V= 6000 $\frac{m}{s}$, high density

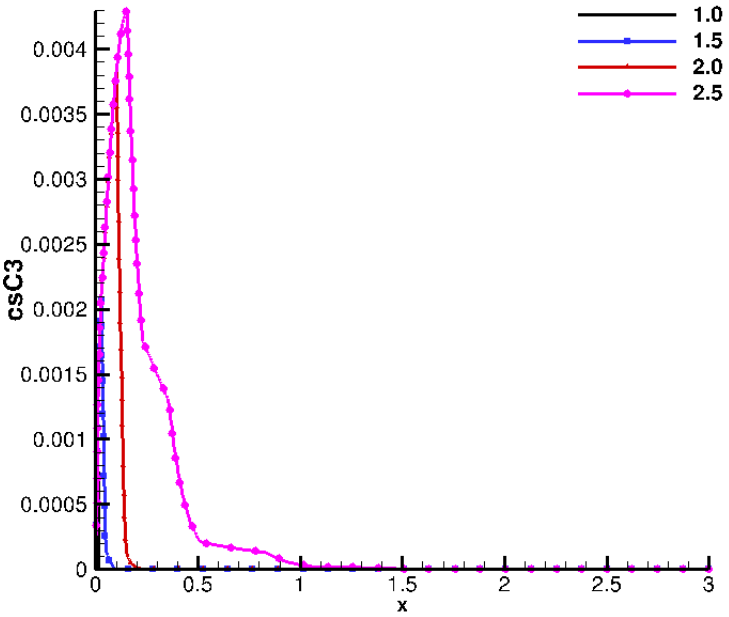

(c) Maximum concentration of C_3 with MZA model

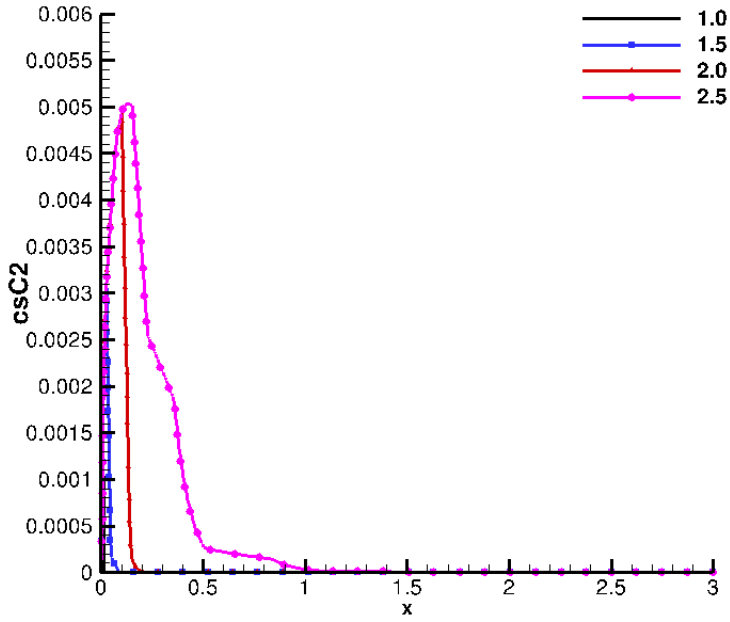

(d) Maximum concentration of C_2 with MZA model

Figure 6.46. Maximum species concentrations with MZA model at varying temperatures, V= 6000 $\frac{m}{s}$, high density

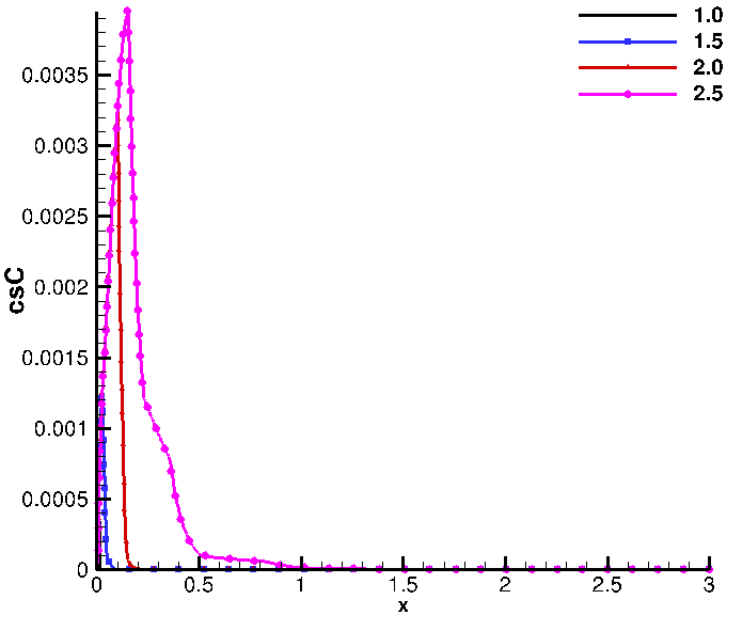

(e) Maximum concentration of C with MZA model

Figure 6.46. Maximum species concentrations with MZA model at varying temperatures, V= 6000 $\frac{m}{s}$, high density

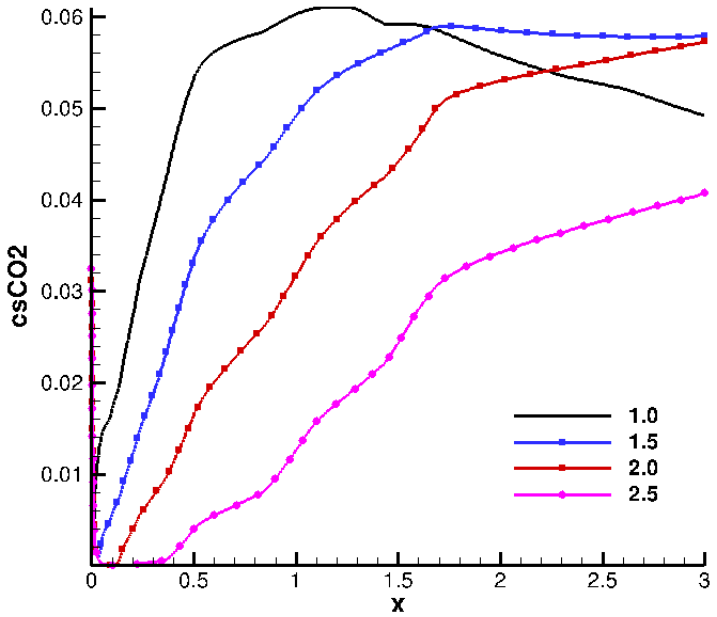

(a) Maximum concentration of CO_2 with MURI model

Figure 6.47. Maximum species concentrations with MURI model at varying temperatures, V= 6000 $\frac{m}{s}$, high density

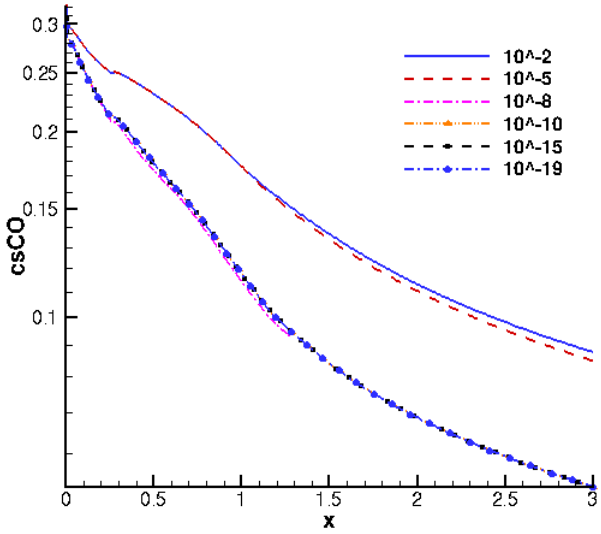

(b) Maximum concentration of CO with MURI model

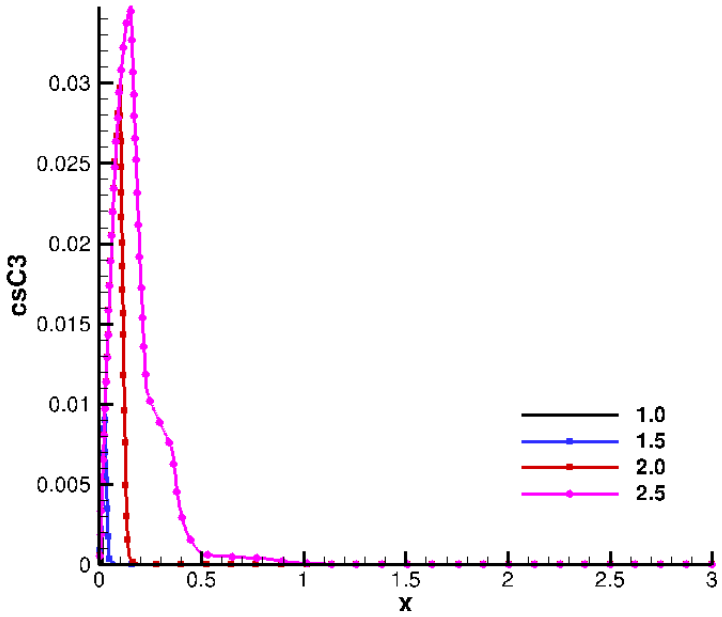

(c) Maximum concentration of C_3 with MURI model

Figure 6.47. Maximum species concentrations with MURI model at varying temperatures, V= 6000 $\frac{m}{s}$, high density

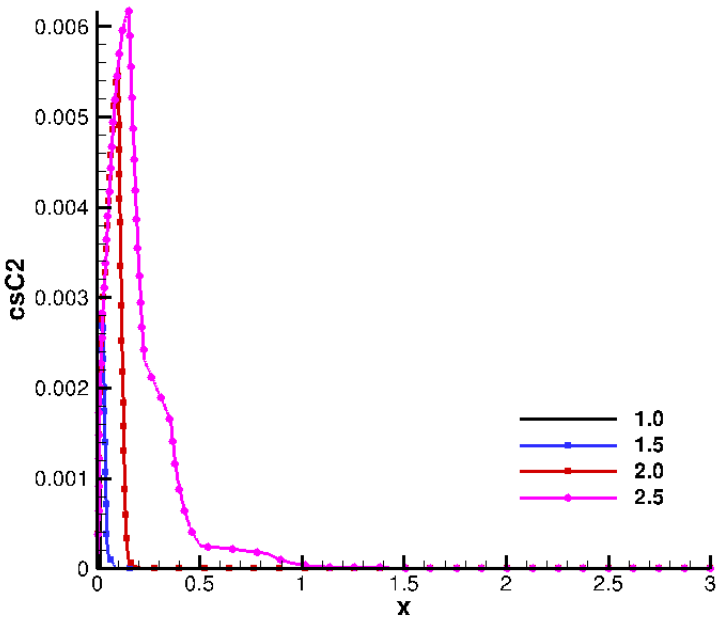

(d) Maximum concentration of C_2 with MURI model

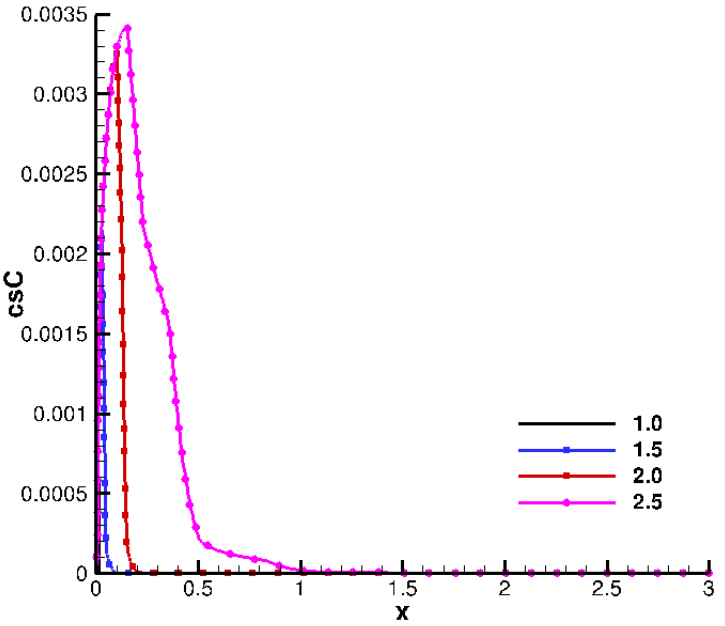

(e) Maximum concentration of C with MURI model

Figure 6.47. Maximum species concentrations with MURI model at varying temperatures, V= 6000 $\frac{m}{s}$, high density

Each of the models shows a high sensitivity to the surface temperature in determining the production of the ablative species. While the Park and MURI models produce nearly monotonically decreasing concentrations of CO_2 as the temperature increases. The MZA model shows a longer sustained higher production of CO_2 along the cone, which results in a sustained high concentration, but exhibits a monotonically increasing concentration of CO_2 at the end of the cone.

Examining the effect this change in concentration of CO_2 has on the stability of the flow, the Park and the MURI models, as the two models have similar trends and concentration values will be assumed to produce similar results and only the Park model stability analysis will be conducted. Figure 6.48 shows the stability results for the Park model comparing the 1.0 and the 2.5 times temperature values. There is a slight decrease in the total N factor for the 2.5 times surface temperature as compared to the original surface temperature. The higher surface temperature is known to stabilize the second mode instabilities, and the increase in surface temperature has a greater stabilizing effect than the decrease in CO_2 damping alone. Examining the stability results for the MZA model, shown in Figure 6.49, increasing the surface temperature increases the stability as well. While some of this increased stability is due to the increased surface temperature, there is also an increase due to the CO_2 damping effect. While the two Park model simulations start amplification at the same location on the body, this is not the case with the MZA model. As the CO_2 concentration increases, the damping effect moves the start of amplification downstream on the body, similar to what was seen during the CO_2 concentration study. This increase in streamwise location for the start of amplification is due to the increase CO_2 in the flow. This conclusion is further supported by a frequency analysis between the original surface temperature and 2.5 times that value. Figure 6.50 shows that at the higher frequencies, CO_2 is effective at damping the amplification. Examining the

amplification per frequency at the lower surface temperature of 1.5 times the original value, there is still an decrease in amplification at the higher frequencies but not as great due to the lower concentration of CO_2 after the start of amplification (see Figure 6.51. Both the higher surface temperature and the increased CO_2 damping effect decreased the total amplification, and both have a significant impact on the stability of the boundary layer.

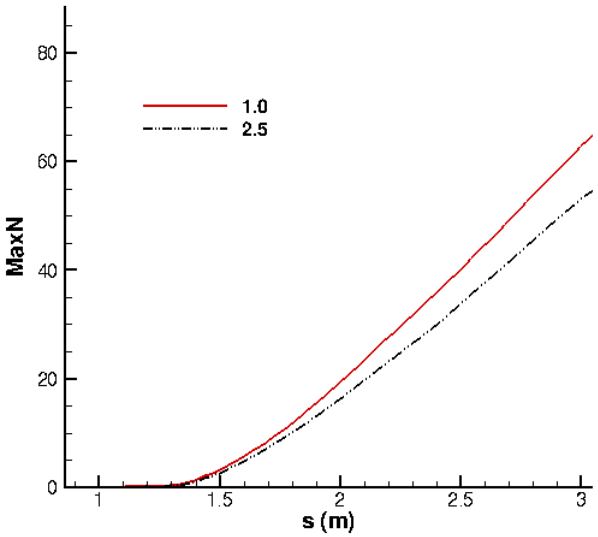

Figure 6.48. Maximum N factor for the Park model at 1.0 and 2.5 times the original surface temperature, V= 6000 $\frac{m}{s}$, high density

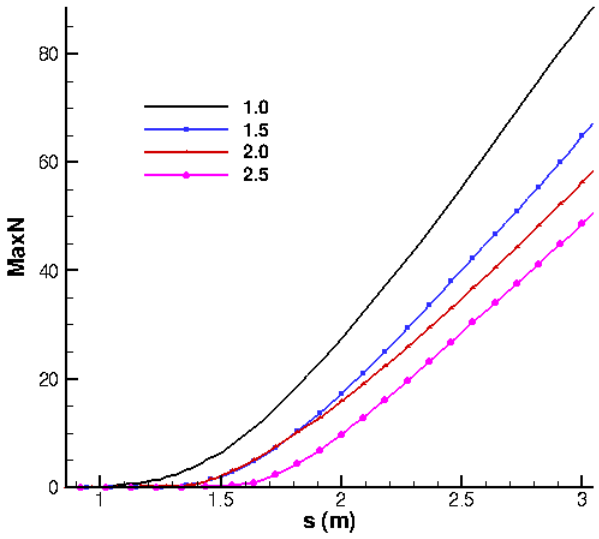

Figure 6.49. Maximum N factor for the MZA model at varying surface temperatures, V= 6000 $\frac{m}{s}$, high density

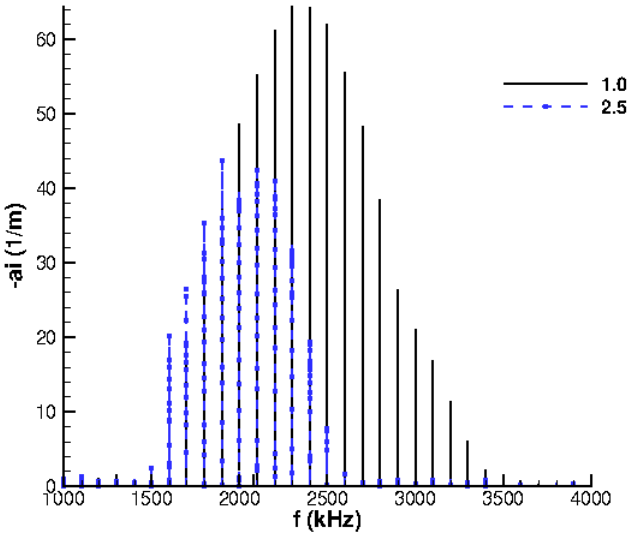

Figure 6.50. Frequency analysis for the MZA model at 1.0 and 2.5 times the original surface temperature, V= 6000 $\frac{m}{s}$, high density

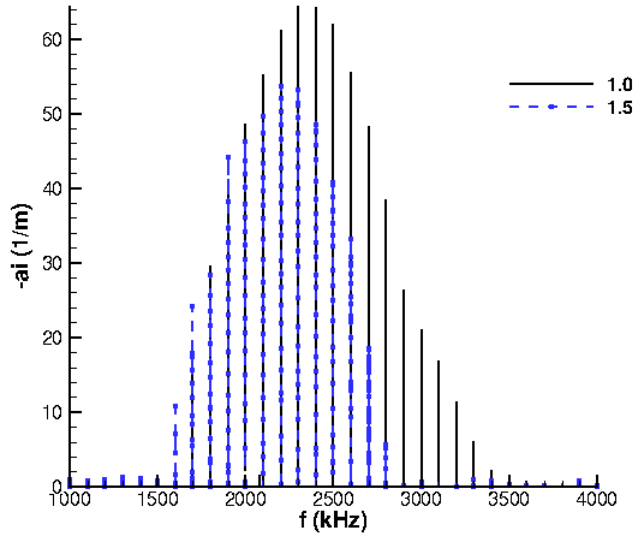

Figure 6.51. Frequency analysis for the MZA model at 1.0 and 1.5 times the original surface temperature, V= 6000 $\frac{m}{s}$, high density

6.3.3 Altitude Effects on Stability.

To examine the sensitivity of the ablation models and the subsequent effects on boundary layer stability to altitude variation, simulations were conducted evaluating CO_2 production at typical reentry trajectory parameters starting. Table 6.1 shows the altitudes and velocities used in this study where the data variable of density, pressure and temperature were determined from the 1976 Standard Atmospheric Tables [2]. Due to the similarities seen between the two Park models as well as the ZA, MZA and Alba models concerning CO_2 production, only the Park, MZA and MURI models were used in this parameter study.

Table 6.1. Freestream input conditions for typical trajectory

Altitude (kft)	$V_\infty(m/s)$	$\rho(kg/m^3)$	$T(K)$
10	2300	0.904	269
20	3500	0.653	248
30	4200	0.458	228
40	5400	0.302	216
50	6100	0.186	216
60	6400	0.115	216
70	6500	0.071	217
80	6600	0.044	221
90	6700	0.027	224
100	6800	0.017	227

Figures 6.52 through 6.54 show the concentrations of CO_2 produced at all altitudes in this parameter study. The surface temperatures were not varied at the different altitude to isolate the altitude effects from surface temperature effects. Though surface temperatures may be lower for high altitude points, the colder wall would destabilize the second mode instabilities. For all models, the maximum concentration of CO_2 was found to be between 40,000 to 60,000 ft. The total concentration of CO_2 for the Park and MURI models varied from 5-8% at these altitudes and decreased for both higher and lower altitudes. The MZA model produced a concentration of approxi-

mately 8% CO_2 along most of the surface after 1.0 m with a spike in production at the nose. Unlike the other two models, the MZA model produced a similar concentration of CO_2 at altitudes above 50,000 ft but significantly less at lower altitudes, showing minimal CO_2 production for altitude below 30,000 ft. These low altitude results are similar to the low enthalpy, high density concentrations seen in the ablation study results. Due to the lower concentrations of CO_2 in the flow, the MZA results will be used in the stability analysis.

Given the concentrations of CO_2 in the boundary layer with the MZA model, a decrease in amplification for altitudes 50,000 and above would be expected with an increase in amplification at lower altitudes. Figure 6.55 shows the N factor results at all altitudes using the MZA model where the N factor decreases with both increasing and decreasing altitudes. Isolating the low altitude results, Figure 6.56 shows a steady increasing stability as the altitude decreases. However, examining the results with vibration disabled (Figure 6.57) shows that at these altitudes, the impact of vibrational damping on boundary layer stability is minimal which would be expected due to a low concentration of CO_2. The cause for this increased stability (decreasing N factor) at lower altitude is most likely a transition from second to first mode dominance as the altitude decreases below 30,000 ft. The edge Mach numbers at these conditions are approximately 3 or below, a flow condition where a transition in mechanisms is shown in the theory.

Examining the high altitudes stability results (Figure 6.58) also shows a steady decrease in N factors (increased stability) as the altitude increase which is caused by the decreasing Reynolds number in the flow. When comparing the results with vibrational modes enabled and disabled (Figure 6.59), there is a significant impact on stability from CO_2 damping and this effect is most prominent at high CO_2 concentrations and lower altitudes. At 90,000 ft there is evidence of CO_2 damping. However, at

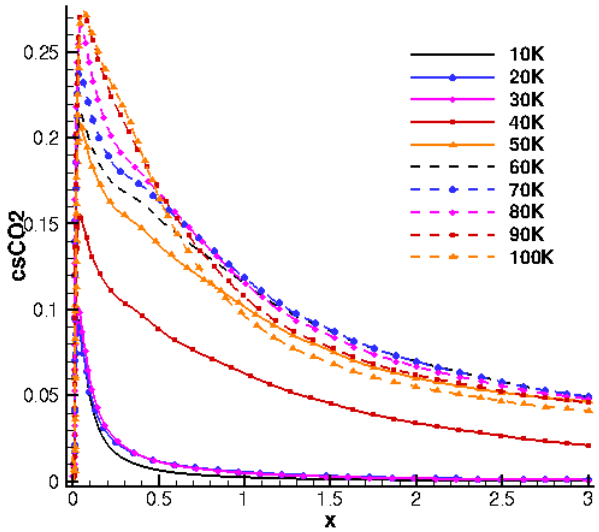

Figure 6.52. Maximum concentration of CO_2 in the boundary layer with the MZA model at typical reentry trajectory altitudes

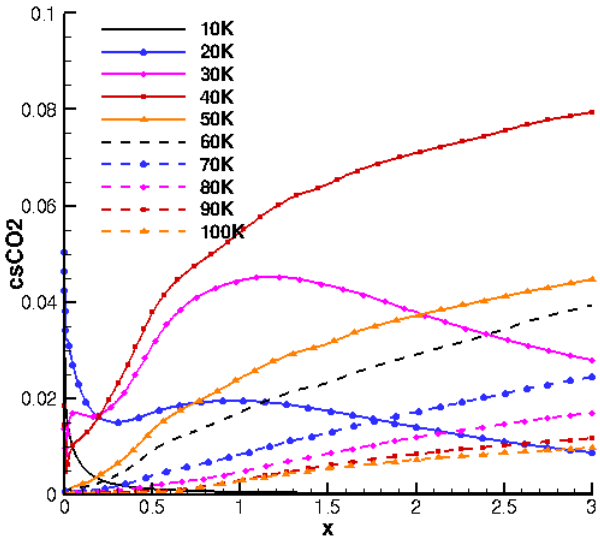

Figure 6.53. Maximum concentration of CO_2 in the boundary layer with the Park model at typical reentry trajectory altitudes

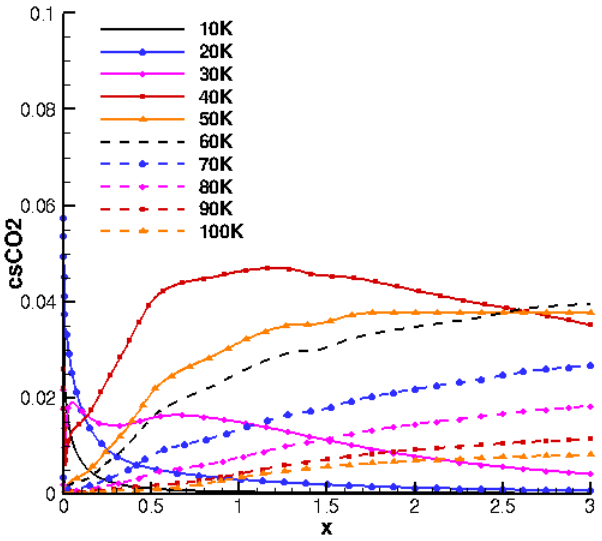

Figure 6.54. Maximum concentration of CO_2 in the boundary layer with the MURI model at typical reentry trajectory altitudes

50,000 ft, the effect of vibrational damping is more pronounced due to higher concentrations and higher amplification rates at this condition. For all high altitude results, the delay in transition due to vibrational damping is greater than 0.5 m (assuming an N factor of 10 marks transition).

At 50,000 ft, due the lower concentration of CO_2 in the boundary layer produced by the Park and MURI model (which is approximately half that produced in the MZA model), the stability results should show an increased N factor when compared to the MZA model results. Figure 6.60 shows that both the Park and MURI models have greater amplification than then MZA model and show a transition location approximately 20 cm earlier than the MZA model. When these simulations are compared with vibrational disabled, all models show similar N factors and thus the increased stability is most likely the result of the damping effects.

The Park model produces a higher concentration of CO_2 in the boundary layer as the MZA model at 40,000 ft, approximately 8% and 5%, respectively at the end of the cone. The stability results at this condition for these two models should be

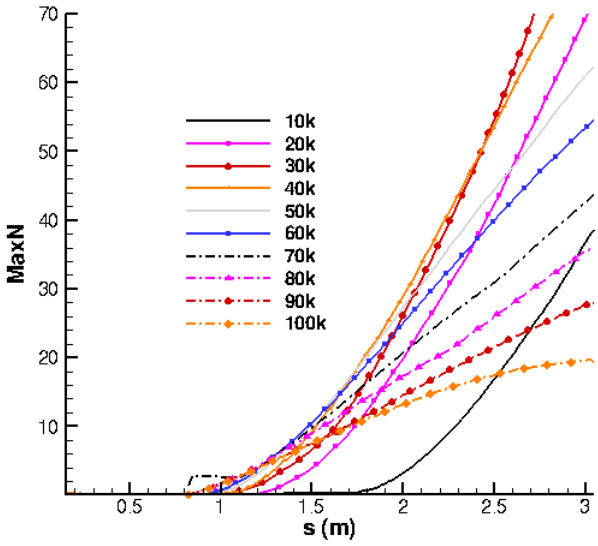

Figure 6.55. Maximum N factors for altitudes from 100k to 10k ft for the MZA model

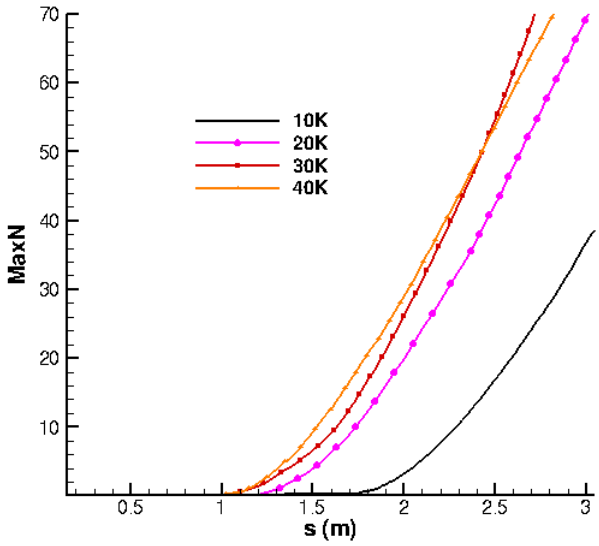

Figure 6.56. Maximum N factors for altitudes below 50k ft for the MZA model

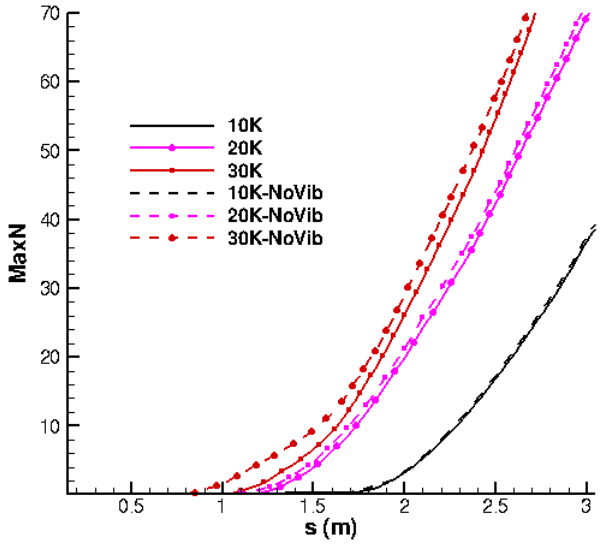

Figure 6.57. Maximum N factors for altitudes below 50k ft with vibration enabled (solid lines) and vibration disabled (dashed lines) for the MZA model

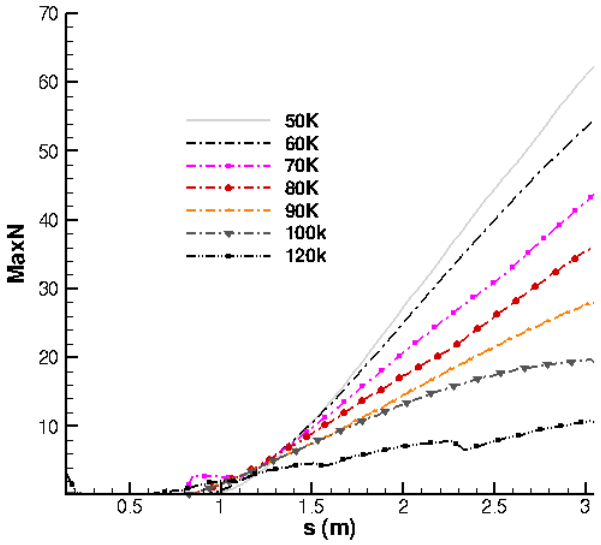

Figure 6.58. Maximum N factors for altitudes above 50k ft for the MZA model

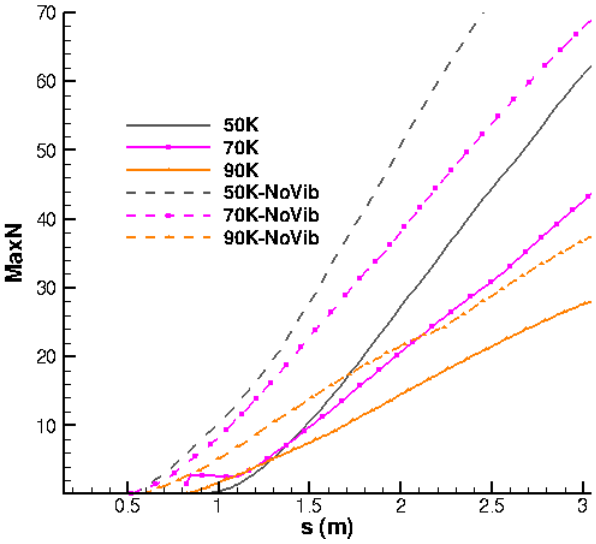

Figure 6.59. Maximum N factors for altitudes above 50k ft with vibration enabled (solid lines) and vibration disabled (dashed lines) for the MZA model

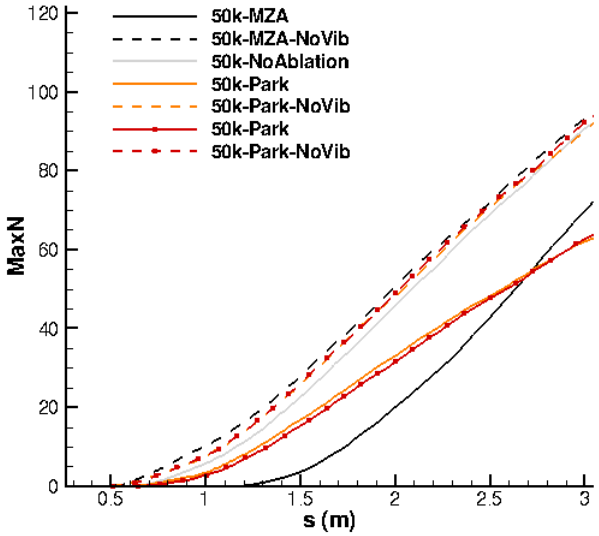

Figure 6.60. Maximum N factors at 50k ft for the Park, MURI and MZA models

similar, with the Park model showing slightly lower amplification if second mode remains the dominant mechanism. Figure 6.61 compares the results of the MZA and the Park models at these conditions and shows a slightly lower amplification with the Park model after approximately 1.3 m. Comparing the concentrations at this x location, both models show 6% with the MZA model concentration decreasing and the Park model concentration increasing. With vibrational modes disable, both models show similar results. Therefore, at 40,000 ft the second mode remains the dominant instability and the CO_2 damping is effective at increasing boundary layer stability. The results from the altitude study show that, for a normal reentry trajectory, as the altitude decreases, CO_2 damping will dampen the second mode disturbances in the boundary layer thus increasing boundary layer stability. When second mode is no longer the dominant instability, below approximately 30,000ft for a typical reentry trajectory, CO_2 damping is no longer effective at stabilizing the boundary layer.

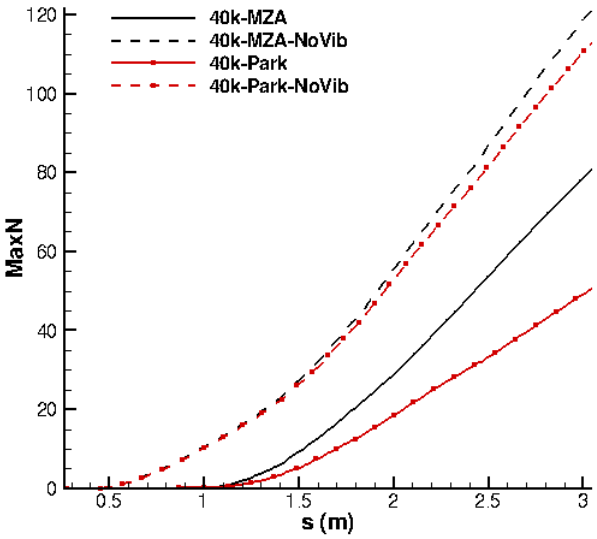

Figure 6.61. Maximum N factors at 40k ft for the Park and MZA models

7. Conclusions

The main purpose of this research was to examine the effects of carbon-based ablative products, specifically CO_2, on second mode instabilities. The research was done in two steps: determine the minimum concentration of CO_2 required to impact the stability characteristics and the transition location and use current carbon gas-surface models at various flow conditions to determine if ablation results in sufficient CO_2 to impact transition characteristics. As each gas-surface model produces different concentrations of chemical species, each boundary layer has unique characteristics. In addition, as uncertainties exist in the models, the effects of altitude, surface temperature and material characteristics were examined to determine the impact on the stability characteristics.

The specific research questions addressed in this study were:

1. What is the sensitivity of a hypersonic boundary layer stability to changes in the species concentrations of carbon-based ablative species, specifically CO_2, at both wind tunnel and flight representative freestream parameters?

2. What are the variations in the current gas-surface chemical models and what effects do these variations have on the CO_2 concentrations and the stability of a hypersonic boundary layer over a sharp and blunt cone?

3. What is the sensitivity of the current gas-surface chemical models to changes in the freestream flow parameters, surface temperature and site density and what are the stability effects?

A concentration study was conducted to determine the sensitivity of the boundary layer to varying CO_2 concentrations on both a sharp and 12.7 mm blunt cone. Using

wind tunnel experimental flow conditions, simulations were conducted at CO_2 concentration from 10%-50% over the sharp cone and 2.5%-50% over the blunt cone at both high and low enthalpy condition. To determine transition location, an N factor value of 10 was used. This N factor value is a typical value seen for transition in a wind tunnel. This study determined, for low enthalpy (approximately 5 $\frac{MJ}{kg}$) wind tunnel conditions, a minimum of 30% CO_2 is required for a 10 cm transition location change over a sharp cone. However, for a blunt cone, a concentration of only between 5-10% is required for the same transition location change. This study found similar results for the high enthalpy flow, at approximately 8.5 $\frac{MJ}{kg}$, where a concentration of 10% over a sharp cone and 2.5% over a blunt cone are required for a 10 cm delay in transition location. The study showed that these variations were caused by the higher temperature in the boundary layer over a blunt cones, highlighting the importance of boundary layer maximum temperature and temperature gradients on the effect of CO_2 damping of second mode instabilities. Also, the differences in boundary layer thickness for both the velocity and thermal boundary layers between the sharp and blunt cone impact the frequencies of the instabilities amplified which also affects the efficacy of CO_2 damping.

Examining flight representative flow condition while maintaining a similar enthalpy or maximum boundary layer temperature as the wind tunnel conditions, CO_2 had a similar impact on amplification. The simulations were conducted at the minimum CO_2 concentration determined from the wind tunnel conditions. While the flight representative cases showed higher total N factor values due to higher Reynolds numbers at flight conditions, the variation between the amplification when vibrational modes were enabled and disabled were similar to those seen in the wind tunnel conditions for similar enthalpy values. When the maximum temperature in the boundary layer was matched at the flight representative conditions, the differences between

the amplification with and without vibrational modes were also similar to those seen under the wind tunnel conditions. This trend was the same for both the high and low enthalpy flows. Further work would need to be conducted to fully understand the impact flight representative flow conditions versus wind tunnel condition on CO_2 damping and stability.

Concerning hypersonic flight within the Earth's atmosphere, the only CO_2 found in the boundary layer comes from the ablation of carbon species from the TPS. Examining CFD simulations at high and low enthalpies, using the different gas-surface models: Park76, Park, ZA, MZA, MURI and ZA with nitridation models, showed the estimated concentrations of CO_2 that would be found in the boundary layer in flight. Simulations were conducted using all models at a low and high density flow conditions and at 3000 $\frac{m}{s}$ and 6000 $\frac{m}{s}$, for low and high enthalpy flows, respectively. In general, the study showed that the models vary significantly on the amount of CO_2 produced from the gas-surface interactions and the interactions with the gas. The study showed that the ZA, MZA and ZA with nitridation models produced similar amounts of CO_2 at all conditions and produced significantly more CO_2 at the nose and along a greater length of the body. These models produced high concentrations at the nose, especially for the blunt cone, and would asymptotically decrease down the body. The Park76, Park and MURI also produced similar quantities of CO_2 in the flow and were generally less prolific than the ZA-based models. The trend for these models was to produce little CO_2 at the nose and have an asymptotically increasing concentration down the body. This reversal in the trend of production sometimes resulted in similar concentrations at the aft section of the 3 m simulated cone. The study found that over a sharp cone, due to the lower surface area at the higher temperatures, all gas-surface models produce significantly less CO_2 in the flow as compared to the blunt, 12.7 mm nose radius, cone.

For the low density simulations, the study showed that neither high nor low enthalpy flow over either cone produced high enough quantities of CO_2 to show clear evidence of damping of the second mode instabilities. However, none of the simulations showed significant amplification of second mode instabilities at either of these conditions, and the low N factor results showed that the boundary layer would not be close to a transitional state. At higher density flow conditions, significantly higher concentrations of CO_2 were produced for all the models, with the greatest concentrations produced at higher enthalpy (6000 $\frac{m}{s}$). The study showed that at high enthalpy and density, the sharp and blunt cones both produced high enough concentrations of CO_2 to impact transition characteristics, based off the CO_2 concentration results. For the sharp cone, there was a slight decrease in the N factors which coincided with the CO_2 concentrations along the body. The study determined, after examination of the amplification per frequency, a slight decrease in amplification around 2-5 MHz existed. For the blunt cone at this condition, the study showed a decrease in N factors for all models, which produced between 5-10% CO_2, and the amplification per frequency showed damping of disturbances at frequencies above 2 MHz. The study determined that, while significant differences exist in the total CO_2 produced by the different models, high enough concentrations of CO_2 to impact transition characteristics can be accomplished with the ablation of a carbon-based TPS at specific freestream conditions. For vehicle design purposes, if the CO_2 in the flow approaches the required concentration it is vital to include vibrational modes when determining transition predictions.

A sensitivity study of the ZA, MZA and the MURI models to material site density parameter was conducted using the blunt cone model. The Park models were not used as they do not include a site density parameter. The ZA model showed great sensitivity to the site density parameter and once this parameter was varied more

than two order of magnitude, higher or lower, the amount of CO_2 produced by the model was greatly reduced. A similar result in not seen in the MZA model, leading to the assumption that it is the lack of desorption reactions and immobility of the sites in the original coding of the ZA model which was the cause of sensitivity. However, the study showed that the MZA model remained highly sensitive to an increase in the site density parameter which caused a higher production of CO_2. The MURI model was extremely insensitive to decreases in the site density parameter but a 50% reduction in CO_2 production is seen when the parameter is increased as the model favor the production of CO to CO_2 in these conditions.

Examining the changes to stability characteristics from this sensitivity, only the MZA model was examined as all other models produced less CO_2. At site density parameters of $1x10^{-5}$ and $1x10^{-2}$, large concentrations of CO_2, around 25% were achieved. The study determined the overall impact on stability, however, was minimal, only changing the transition location by a maximum of 12 cm. Given this low impact on stability, change in material properties with regards to defects or fiber orientation would not significantly impact transition prediction, despite model sensitivity to the site density parameter. Further work would need to be conducted to determine the precise reactions that cause the variations to occur between the models as well as to fully understand the interaction between the increased ablation and CO_2 damping with regards to stability.

The sensitivity of the Park, MZA and MURI models to surface temperature variations was examined for the blunt cone geometry. All models showed an increase in the production of sublimation products at higher surface temperatures, directly corresponding to a surface temperature near the vaporization temperature of graphite. The study determined that the Park and MURI model both favored the production of CO versus CO_2 as the surface temperature was increased and the total concentration

of CO_2 monotonically decreased as the temperature increased. The study showed that the MZA model favored the production of CO_2 after the surface temperature decreased to below approximately 3500 K. However, the maximum concentration of CO_2 in the boundary layer did not increase for the MZA model, which remained around 15%, but concentrations peaked farther downstream and did not decrease as quickly as the temperature was increased. The study determined that the impact on stability of the increased CO_2 concentration for the MZA model was noticeable, in both a delay in the start of transition and lower amplification which resulted in a total change of transition location from the lowest to highest temperatures of approximately 0.5 m. The impact of the decreased CO_2 concentration from the Park model was also examined and showed a slight decrease in the overall N factor as well. While not fully resolved in this analysis, this result is assumed to be due to the higher surface temperature stabilizing the second mode instabilities as opposed to vibrational damping effects. Further work would need to be conducted to determine the overall impact surface temperature has versus CO_2 damping on second mode instability stabilization.

Again, using the MZA, Park and MURI models, an analysis of the sensitivity of the models to changes in altitudes was examined. For this study, typical reentry trajectory conditions and standard atmosphere values were used for the freestream conditions. The study showed that the Park and MURI models had similar CO_2 production and the maximum concentration occurred at 40,000 ft, decreasing at both higher and lower altitudes. For the MZA model, there was a slight decrease in the CO_2 concentrations as altitude decreased up to 50,000 ft, though variations were limited to less than 5%. Between 10,000 and 30,000 ft similar CO_2 concentrations were shown to decrease significantly.

The resulting impact of altitude variation on stability was more difficult to determine. The study determined that, along with the changing CO_2 concentrations, the changing Reynolds number of the flow impacted the transition characteristics as much as the CO_2 damping effects. However, the study revealed general trends that could be determined and examined overall stability, with respect to vibrational modes enabled or disabled. At altitude above 50,000 ft, a trend of decreasing N factor as altitude increases is seen, most likely due to the decreased Reynolds number at higher altitude. However, the study showed, when examining the stability results with vibrational modes disabled, the impact of CO_2 damping remained evident at these altitudes. Examining stability results below 30,000 ft, there is a reduction in N factor as the altitude decreases. This reduction is most likely caused by the change in dominant instability modes from second to first mode instabilities due to the lower edge Mach number. Examining the stability results with vibrational modes disabled, no significant damping is occurring, though whether from the lower concentrations of CO_2 or from the transition of second to first mode dominated flow is unclear. Further work needs to be conducted at the lower altitudes to examine the first mode instability to determine its impact on the stability characteristics.

Bibliography

[1] Leyva, I. A., Laurence, S., Beierholm, A. K.-W., Hornung, H. G., Wagnild, R. W., and Candler, G. C., "Transition Delay in Hypervelocity Boundary Layers by Means of CO_2/Acoustic Instability Interactions," *47th AIAA Aerospace Sciences Meeting Including the New Horizons Forum and Aerospace Exposition*, AIAA-2009-1287, Orlando, FL, 2009. doi:10.2514/6.2009-1287.

[2] *1976 Standard Atmosphere Tables*, NASA, https://ntrs.nasa.gov/archive/nasa/casi.ntrs.nasa.gov/19770009539, 1976.

[3] White, F. M., *Viscous Fluid Flow, 3rd edition*, McGraw-Hill, New York, 1991.

[4] Stetson, K. F., "Nosetip Bluntness Effects on Cone Frustrum Boundary Layer Transition in Hypersonic Flow," *16th Fluid and Plasma Dynamics Conference*, AIAA-1983-1763, 1983. doi:10.2514/6.1983-1763.

[5] Rotta, N. R., "Effects of nose bluntness on the boundary layer characteristics of conical bodies at hypersonic speeds," Tech. rep., New York University, 1966. NYUAA-66-66.

[6] Stetson, K. F., Thompson, E. R., Donaldson, J. C., and Siler, L. G., "Laminar Boundary Layer Stability Experiments on a Cone at Mach 8, Part 2: Blunt Cone," *AIAA 22nd Aerospace Sciences Meeting*, AIAA-1984-0006, 1984. doi: 10.2514/6.1984-0006.

[7] Adam, P., and Hornung, H. G., "Enthalpy Effects on Hypervelocity Boundary Layer Transition: Ground and Flight Data," *Journal of Spacecraft and Rockets*, Vol. 34, 1997, pp. 614–626.

[8] Johnson, H. B., Seipp, T. G., and Candler, G. V., "Numerical Study of Hypersonic Reacting Boundary Layer Transition on Cones," *Physics of Fluids*, Vol. 10, No. 10, 1998.

[9] Fujii, K., and Hornung, H. G., "Experimental investigation of high-enthalpy effects on attachment-line boundary layer transition," *AIAA Journal*, Vol. 41, No. 7, 2003.

[10] Jewell, J. S., Wagnild, R., Leyva, I. A., Candler, G. V., and Shepherd, J., "Transition within a hypervelocity boundary layer on a 5-degree half-angle cone in a freestream of air/CO_2 mixtures," *51st AIAA Aerospace Science Meeting*, AIAA 2013-523, 2013.

[11] Marschall, J., and MacLean, M., "Surface Chemistry in Non-Equilibrium Flows," *Hypersonic Nonequilibrium Flows:Fundamentals and Recent Advances*, edited by E. Josyula, AIAA, Atlanta, Georgia, 2015, 1st ed., pp. 239–328.

[12] Bitter, N., and Shepherd, J., "Stability of highly cooled hypervelocity boundary layers," *Journal of Fluid Mechanics*, Vol. 778, 2015, pp. 586–620.

[13] Marschall, J., and MacLean, M., "Finite-Rate Surface Chemistry Model, I: Formulation and Reaction System Examples," *42nd Thermophysics Conference*, 2011.

[14] Zhluktov, S. V., and Abe, T., "Viscous Shock-Layer Simulation of Airflow past Ablating Blunt Body with Carbon Surface," *Journal of Thermophysics and Heat Transfer*, Vol. 13, No. 1, 1999, pp. 50–59.

[15] Alba, C. R., "A Nonequilibrium Finite-Rate Carbon Ablation Model for Radiating Earth Re-Entry Flows," Ph.D. thesis, Air Force Institute of Technology, 2015.

[16] Poovathingal, S., and Schwartzentruber, T. E., "Finite-Rate Oxidation Model for Carbon Surfaces from Molecular Beam Experiments," *AIAA Journal*, Vol. 55, No. 5, 2017.

[17] Jewell, J. S., "Boundary-Layer Transition on a Slender Cone in Hypervelocity Flow with Real Gas Effects," Ph.D. thesis, California Institute of Technology, Pasadena, CA, 2014. doi:10.7907/Z9H9935V.

[18] Schlichting, H., and Gerten, K., *Boundary-Layer Theory*, Springer, Berlin, Germany, 2017.

[19] Mack, L. M., "Special Course on Stability and Transition of Laminar Flow," Tech. Rep. AGARD-R-709, AGARD Special Course, 1984.

[20] Demetriades, A., "Hypersonic Viscous Flow over a Slender Cone, Part III: Laminar Instability and Transition," *7th Fluid Dynamics Conference*, AIAA 1974-535, 1974.

[21] Kendall, J. M., "Wind Tunnel Experiments Relating to Supersonic and Hypersonic Boundary Layer Transition," *AIAA Journal*, Vol. 13, No. 3, 1975, pp. 290–299.

[22] Stetson, K. F., and Kimmel, R. L., "On Hypersonic Boundary Layer Stability," 1992.

[23] Stetson, K. F., "On Predicting Hypersonic Boundary Layer Transition," Tech. Rep. AFWAL-TM-87-160-FIMG, Flight Dynamics Laboratory, 1987.

[24] Malik, M. R., "Hypersonic Flight Transition Data Analysis Using Parabolized Stability Equations with Chemistry Effects," *Journal of Spacecraft and Rockets*, Vol. 40, No. 3, May-June 2003, pp. 332–344.

[25] Germain, P. D., and Hornung, H. G., "Transition on a Slender Cone in Hypersonic Velocity Flow," *Experiments in Fluids*, Vol. 22, No. 3, 1997, pp. 183–190.

[26] Camac, M., "CO_2 Relaxation Processes in Shock Waves," *Fundamental Phenomena in Hypersonic Flow*, edited by J. G. Hall, Cornell University Press, Ithica, New York, 1966, 1st ed., pp. 195–215.

[27] Mack, L. M., "Transition and Laminar Instability," Tech. Rep. JPL Publication 77-15, Jet Propulsion Lab, 1977.

[28] Herbert, T., "Parabolized Stability Equations," *Annual Review of Fluid Mechanics*, Vol. 29, 1997, pp. 245–283.

[29] Leyva, I. A., Jewell, J. S., Laurence, S., Hornung, H. G., and Shepherd, J. E., "On the Impact of Injection Schemes on Transition in Hypersonic Boundary Layers," *16th AIAA/DLR/DGLR International Space Planes and Hypersonic Systems and Technologies Conference*, AIAA-2009-7204, Bremen, Germany, 2009. doi:10.2514/6.2009-7204.

[30] *US3D Users Manual*, University of Minnesota, Minneapolis, MN, 2017.

[31] Park, C., *Nonequilibrium Hypersonic Aerodynamics*, Wiley and Sons, Inc., New York, 1990.

[32] Park, C., "Effects of Atomic Oxygen on Graphite Ablation," *AIAA Journal*, Vol. 14, No. 11, 1976, pp. 1640–1642.

[33] *STABL3D Users Manual*, Brooklyn Park, MN, 2012.

[34] Saric, W. S., Reed, H. L., and White, E. B., "Stability and Transition of Three-Dimensional Boundary Layers," *Annual Review of Fluid Dynamics*, Vol. 35, No. 1, 2003, pp. 413–440.

[35] Schneider, S. P., "Developing mechanism-based methods for estimating hypersonic boundary-layer transition in flight: the role of quiet tunnels," *Progress in Aerospace Sciences*, Vol. 72, 2015, pp. 17–29.

[36] Reshotko, E., "Transition Issues at Hypersonic Speeds," *44th AIAA Aerospace Science Meeting*, AIAA-2006-707, 2018. doi:10.2514/6.2006-707.

[37] Fedorov, A., "Transition and Stability of High-Speed Boundary Layers," *Annual Review of Fluid Mechanics*, Vol. 43, 2011, pp. 79–95.

[38] Cook, D. A., Thome, J. S., Brock, J. M., Nichols, J. W., and Candler, G. V., "Understanding effects of nose-cone bluntness on hypersonic boundary layer transition using input-output analysis," *AIAA SciTech*, AIAA 2018-0378, 2018. doi:10.2514/6.2018-0378.

[39] Herbert, T., and Santos, G. R., "On the Mechanism of Transition in Boundary Layers," *19th Fluid Dynamics, Plasma Dynamics and Lasers Conference*, AIAA 1987-1201, 1987.

[40] Stetson, K. F., and Rushton, G. H., "Shock Tunnel Investigation of Boundary-Layer Transition at M = 5.5," *AIAA Journal*, Vol. 5, No. 5, 1967, pp. 899–906.

[41] Mack, L. M., "Boundary-layer stability theory, Part B," Tech. Rep. JPL Doc 900-277, Jet Propulsion Lab, 1969.

[42] Mack, L. M., "Linear Stability Theory and the Problem of Supersonic Boundary-Layer Transition," *AIAA Journal*, Vol. 13, No. 3, 1975, pp. 278–289.

[43] Malik, M. R., Spall, R. E., and Chang, C.-L., "Effects of Nose Bluntness on Boundary Layer Stability and Transition," *AIAA*, Vol. Paper 90-0112, 1990.

[44] Malik, M. R., and Anderson, E. C., "Real Gas Effects on Hypersonic Boundary Layers," *Physics of Fluids*, Vol. 3, 1991.

[45] Stuckert, G. K., and Reed, H. L., "Linear Disturbances in Hypersonic, Chemically Reacting Shock Layers," *AIAA Journal*, Vol. 32, 1994, p. 1384.

[46] Morkovin, M. V., "Critical Evaluation of Transition from Laminar to Turbulent Shear Layers with Emphasis on Hypersonically Traveling Bodies," Tech. Rep. AFFDL-TR-68-149, Air Force Flight Dynamics Laboratory, 1969.

[47] Smith, A. M. O., and Gamberoni, N., "Transition, Pressure Gradient, and Stability Theory," Tech. Rep. Report No: ES-26388, Douglas Aircraft Company, 1956.

[48] Van Ingen, J. L., "A Suggested Semi-Empirical Method for the Calculation of the Boundary Layer Transition Region," Tech. Rep. Report V.T.H.-74, Technische Hogeschool Vliegtuigbouwkunde, 1956.

[49] Jaffe, N. A., Okamura, T., and Smith, A. M. O., "Determination of Spatial Amplification Factors and Their Application to Predicting Transition," *AIAA Journal*, Vol. 8, No. 2, 1970, pp. 301–307.

[50] Van Ingen, J. L., "The e^N method for Transition Prediction: Historical Review of Work at TU Delft," *38th Fluid Dynamics Conference*, AIAA 2008-3830, 2008.

[51] Wagnild, R. M., "High Enthalpy Effects on Two Boundary Layer Disturbances in Supersonic and Hypersonic Flow," Ph.D. thesis, University of Minnesota, 2012.

[52] John D. Anderson, J., *Fundamentals of Aerodynamics*, McGraw-Hill, New York, 2011.

[53] Sakakeeny, J., Bartista, A., and Kuehl, J., "How nose bluntness suppresses second-mode growth," *AIAA AVIATION Forum*, AIAA 2019-3083, 2019. doi: 10.2514/6.2019-3083.

[54] Hirschel, E. H., *Basics of Aerothermodynamics*, Springer, Switzerland, 2015.

[55] Ferri, A., and Libby, P. A., "Note on the Interaction Between the Boundary Layer and the Inviscid Flow," *Journal of Aeronautics*, Vol. 21, 1953, pp. 130–136.

[56] Zakkay, V., and Krause, E., "Boundary Conditions at the Outer Edge of the Boundary Layer on Blunted Conical Bodies," *AIAA Journal*, Vol. 1, No. 7, 1963, pp. 1671–1672. doi:10.2514/3.1884.

[57] Softley, E. J., "Boundary Layer Transition on Hypersonic Blunt Slender Cones," *AIAA Fluid and Plasma Dynamics Conference*, AIAA 1969-705, 1969. doi: 10.2514/6.1969-705.

[58] Muir, J. F., and Trujillo, A., "Experimental Investigation of the Effects of Nose Bluntness, Free-stream Unit Reynolds Number and Angle of Attack on Cone Boundary Layer Transition at a Mach Number of 6," *10th Aerospace Sciences Meeting*, AIAA 1972-216, 1972. doi:10.2514/6.1972-216.

[59] Stetson, K. F., "Effect of Bluntness and Angle of Attack on Boundary Layer Transition on Cones and Biconic Configurations," *17th AIAA Aerospace Science Meeting*, AIAA 1979-0269, 1979. doi:10.2514/6.1979-269.

[60] Blyholder, G., and Eyring, H., "Kinetics of graphite oxidation," *Journal of Physical Chemistry*, Vol. 61, No. 5, 1957, pp. 682–688. doi:10.1021/j150551a039.

[61] Scala, S. M., and Gilbert, L. M., "Sublimation of graphite at hypersonic speeds," *AIAA Journal*, Vol. 3, No. 9, 1965, pp. 1635–1644. doi:10.2514/3.3220.

[62] Metzger, J. W., Engel, M. J., and Diaconis, N. S., "Oxidation and sublimation of graphite in simulated re-entry environments," *AIAA Journal*, Vol. 5, No. 3, 1967, pp. 451–460. doi:10.2514/3.4001.

[63] Lundell, J. H., and Dickey, R. R., "Ablation of ATJ graphite at high temperatures," *AIAA Journal*, Vol. 11, No. 1, 1973, pp. 216–222. doi:10.2514/3.504515.

[64] Schmitt, S., Grana-Otero, J., and Mahmoudi, S., "Molecular-sclae carbon oxidation at hypersonic speeds," *AIAA AVIATION Forum*, AIAA 2019-3129, 2019. doi:10.2514/6.2019-3129.

[65] Grana-Otero, J., Schmitt, S., and Mahmoudi, S., "Surface ablation regime of a moel of porous material," *AIAA AVIATION Forum*, AIAA 2019-3127, 2019. doi:10.2514/6.2019-3127.

[66] Zeldovich, Y. B., and Raizer, Y. P., *Physics of Shock Waves and High-Temperature Hydrodynamic Phenomena*, College Publishing, Mineola, New York, 2002.

[67] Vincenti, W. G., and Kruger, C. H., *Introduction to Physical Gas Dynamics*, Krieger Publishing Company, Florida, 1965.

[68] Armenise, I., and Kustova, E. V., "State-to-state models for CO_2molecules: from the theory to an application to hypersonic boundary layers," *Journal of Chemical Physics*, Vol. 145, 2013, pp. 269–281.

[69] Kustova, E., Mekhonoshina, M., and Kosareva, A., "Relaxation process in carbon dioxide," *Physics of Fluids*, Vol. 31, 2019. doi:10.10163/1.5093141.

[70] Stull, V. R., Wyatt, P., and Plass, G., "Vibrational energies of the CO_2molecule," *The Journal of Chemical Physics*, Vol. 37, 1962. doi:10.10163/1.1733302.

[71] Joly, V., and Robin, A., "Vibrational relaxation of CO_2(m,n^l,p) in a CO_2-N_2 mixture. Part 1: Survey of available data," *Aerospace Science and Technology*, Vol. 4, 1999, pp. 229–238. doi:10.1016/S1270-9638(99)80045-5.

[72] Aldoshin, G., and Yakovlev, S., "Analytic model of vibrations of a carbon dioxide molecule. Fermi resonance," *Mechanics of Solids*, Vol. 50, 2015, pp. 33–43. doi:10.3103/S0025654415010045.

[73] Leyva, I. A., "Transition Delay in Hypervelocity Boundary Layers by Means of Vibrational Relaxation and Acoustic Instability Interactions," Tech. Rep. AFRL-RQ-ED-TR-2013-0054, Air Force Research Laboratory, 2013.

[74] Buresti, G., "A note on Stoke's hypothesis," *Acta Mechanica*, Vol. 226, 2015. doi:10.1007/S00707-015-1380-9.

[75] Boukharfane, R., Martinez Ferrer, P., and Mura, A., "On the role of bulk viscosity in compressible reactive shear layer developments," *10th International Conference on Computational Fluid Dynamics*, ICCFD10, 2018.

[76] Gnoffo, P. A., Gupta, R. N., and Shinn, J. L., "Conservation Equations and Physical Models for Hypersonic Air Flows in Thermal and Chemical Nonequilibrium," Tech. Rep. NASA-TP 2867, NASA Langley, Hampton, Virginia, 1989.

[77] Park, C., "Review of Chemical-Kinetic Problems of Future NASA Missions I: Earth Entries," *Journal of Thermophysics and Heat Transfer*, Vol. 18, No. 1, 1994.

[78] C. Park, J., and Partridge, "Chemical-Kinetic Parameters of Hyperbolic Earth Entry," *AIAA*, 2000, pp. AIAA Paper 00–0210.

[79] Park, C., "Assessment of Two-Temperature Kinetic Model for Ionizing Air," *AIAA*, 1987, pp. AIAA Paper 87–1574.

[80] Park, C., "Assessment of the Two-Temperature Kinetic Model for Ionizing Air," *Journal of Theromophysics and Heat Transfer*, Vol. 3, No. 3, 1989.

[81] *NASA CEA Database*, NASA, https://www.grc.nasa.gov/www/CEAWeb, 2018.

[82] Millikan, R. C., and White, D. R., "Systematics of Vibrational Relaxation," *Journal of Chemical Physics*, Vol. 39, 1963, pp. 3209–3213.

[83] Dorrance, W. H., *Viscous Hypersonic Flow: Theory of Reacting and Hypersonic Boundary Layers*, Dover Publishing, Inc, New York, 2017.

[84] Lin, C. C., "On the Stability of Two-Dimensional Parallel Flows Part I," *Quarterly of Applied Mathematics*, Vol. III, No. 3, 1945, pp. 117–142.

[85] Liepmann, H. W., "Investigations on laminar boundary-layer stability and transition on curved boundaries," Tech. Rep. NACA Wartime Report W-107, NACA, 1943.

[86] Schubauer, G. B., and Scramstad, H. K., "Laminar Boundary-Layer Oscillations and Stability of Laminar Flow," *Journal of the Aeronautical Sciences*, Vol. 14, No. 2, 1947, pp. 69–78.

[87] Lees, L., "The Stability of the Laminar Boundary Layer in a Compressible Fluid," Tech. Rep. NASA TR No 876, NASA, 1947.

[88] Dunn, D. W., and Lin, C. C., "On the Stability of the Laminar Boundary Layer in a Compressible Fluid," *Journal of the Aeronautical Sciences*, Vol. 22, 1955, pp. 455–473.

[89] Lees, L., and Reshotko, E., "Stability of the Compressible Laminar Boundary Layer," *Journal of Fluid Mechanics*, Vol. 12, No. 4, 1962, pp. 555–589.

[90] Chang, C. L., Vihn, H., and Malik, M. R., "Hypersonic Boundary-Layer Stability with Chemical Reactions using PSE," *28th Fluid Dynamics Conference*, AIAA 1997-2012, 1997.

[91] Gaster, M., "A note on the relation between temporally-increasing and spatially-increasing disturbances in hydrodynamic stability," *Journal of Fluid Mechanics*, Vol. 14, 1962, pp. 222–224.

[92] MacCormack, R., *Numerical Computation of Compressible and Viscous Flows*, AIAA Educational Series, Virginia, 2014.

[93] Steger, J. L., and Warming, R. F., "Flux Vector Splitting of the Inviscid Gas-Dynamic Equations with Application to Finite-Difference Methods," *Journal of Computational Physics*, Vol. 40, No. 2, 1982, pp. 263–293.

[94] Van Leer, B., "Towards the Ultimate Conservative Difference Scheme: Second-Order Sequel to Godunov's Method," *Journal of Computational Physics*, Vol. 32, No. 1, 1979, pp. 101–136. doi:10.1016/002-9991(79)90145-1.

[95] Subbareddy, P., and Candler, G. V., "A Fully Discrete, Kinetic Energy Consistent Finite-Volume Scheme for Compressible Flows," *Journal of Computational Physics*, Vol. 228, No. 4, 2009, pp. 1347–1364.

[96] Wright, M., Candler, G., and Bose, D., "A Data-Parallel Line Relaxation Method for the Navier-Stokes Equations," *13th Computational Fluid Dynamics Conference*, AIAA-1997-2046, 1997. doi:10.2514/6.1997-2046.

[97] Candler, G. V., Subbareddy, P. K., and Brock, J. M., "Advances in Computational Fluid Dynamics Methods for Hypersonic Flow," *Journal of Spacecraft and Rockets*, Vol. 52, No. 1, 2015, pp. 17–28. doi:10.2514/1.A33023.

[98] MacLean, M. J., M., and Driver, D. M., "Finite-Rate Surface Chemistry Model, II: Coupling to Viscous Navier-Stokes Code," *AIAA Journal*, 2011.

[99] Park, C., "Stagnation-Point Ablation of Carbonaceous Flat Disks-Part I: Theory," *AIAA Journal*, Vol. 21, No. 11, 1983, pp. 1588–1594.

[100] Park, C., and Bogdanoff, D. W., "Shock-tube Measurement of Nitridation Coefficient of Solid Carbon," *Journal of Thermophysics and Heat Transfer*, Vol. 20, No. 3, 2006.

[101] Chen, Y. K., and Milos, F. S., "Navier-Stokes Solutions with Finite-Rate Ablation for Planetary Mission Earth Reentries," *Journal of Spacecraft and Rockets*, Vol. 42, No. 6, 2005, pp. 961–970.

[102] Candler, G. V., Alba, C. R., and Greendyke, R. B., "Characterization of carbon ablation models including effects of gas-phase chemical kinetics," *Journal of Thermophysics and Heat Transfer*, Vol. 31, No. 3, 2017, pp. 512–526. doi: 10.2514/1.T4752.

[103] Candler, G. V., "Nonequilibrium Process in Hypervelocity Flow: An Analysis of Carbon Ablation Models," *AIAA*, 2012, pp. AIAA Paper 2012–0724.

[104] Swaminathan-Goplan, K., Borner, A., Murray, V. J., Poovathingal, S., Minton, T. K., Mansour, N. N., and Stephani, K. A., "Development and validation of a finite-rate model for carbon oxidation by atomic oxygen," *Carbon*, Vol. 137, 2018, pp. 313–332. doi:10.1016/j.carbon.2018.04.088.

[105] Jewell, J. S., and Shepherd, J. E., "T5 Conditions Report: Shots 2526–2823," Tech. rep., California Institute of Technology, Pasadena, CA, June 2014. doi: 10.7907/Z9H9935V, gALCIT Report FM2014.002.

[106] I., N., Drayna, T., and Candler, G. V., "Development of a Hybrid Unstructured Implicit Solver for the Simulation of Reacting Flows over Complex Geometries," *AIAA Aviation*, AIAA 2004-2227, 2004.

[107] Blottner, F. G., Johnson, M., and Ellis, M., "Chemically Reacting Viscous Flow Program for Multi-component Gas Mixture," Tech. Rep. TR-SC-RR-70-754, Sandia National Labs, 1971.

[108] Wilke, C. R., "A Viscosity Equation for Gas Mixtures," *Journal of Chemical Physics*, Vol. 18, No. 4, 1950, pp. 517–519.

[109] Abrahamson, J., "Graphite sublimation temperatures, carbon arcs and crystallite erosion." *Carbon*, Vol. 12, No. 2, 1975, pp. 111–141. doi:10.1016/008-6223(74)90019-0.

[110] George, D., *Ablative Thermal Protection System Modeling*, AIAA Education Series, Reston, VA, 2013.

REPORT DOCUMENTATION PAGE

Form Approved
OMB No. 0704-0188

The public reporting burden for this collection of information is estimated to average 1 hour per response, including the time for reviewing instructions, searching existing data sources, gathering and maintaining the data needed, and completing and reviewing the collection of information. Send comments regarding this burden estimate or any other aspect of this collection of information, including suggestions for reducing the burden, to Department of Defense, Washington Headquarters Services, Directorate for Information Operations and Reports (0704-0188), 1215 Jefferson Davis Highway, Suite 1204, Arlington, VA 22202-4302. Respondents should be aware that notwithstanding any other provision of law, no person shall be subject to any penalty for failing to comply with a collection of information if it does not display a currently valid OMB control number.

PLEASE DO NOT RETURN YOUR FORM TO THE ABOVE ADDRESS.

1. REPORT DATE *(DD-MM-YYYY)*	2. REPORT TYPE	3. DATES COVERED *(From - To)*
12-08-2019	PhD Dissertation	23 Aug 2016 - 12 Sep 2019

4. TITLE AND SUBTITLE

Effects of Carbon-based Ablation Products on Hypersonic Boundary Layer Stability

5a. CONTRACT NUMBER

5b. GRANT NUMBER

5c. PROGRAM ELEMENT NUMBER

6. AUTHOR(S)

Elliott, Olivia S., Lt Col

5d. PROJECT NUMBER

5e. TASK NUMBER

5f. WORK UNIT NUMBER

7. PERFORMING ORGANIZATION NAME(S) AND ADDRESS(ES)

Air Force Institute of Technology
Graduate School of Engineering and Management (AFIT/EN)
2950 Hobson Way
Wright-Patterson AFB OH 45433-7765

8. PERFORMING ORGANIZATION REPORT NUMBER

AFIT-ENP-DS-19-S-074

9. SPONSORING/MONITORING AGENCY NAME(S) AND ADDRESS(ES)

Air Force Research Laboratory/Weapons Directorate
3000 Eglin Blvd
Eglin AFG, FL 32543

10. SPONSOR/MONITOR'S ACRONYM(S)

AFRL/RW

11. SPONSOR/MONITOR'S REPORT NUMBER(S)

12. DISTRIBUTION/AVAILABILITY STATEMENT

Approved for Public Release. Distribution Unlimited

13. SUPPLEMENTARY NOTES

This material is declared work of the U.S. Government and is not subject to copyright protection in the United States.

14. ABSTRACT

Hypersonic vehicles require an accurate prediction of the transition of the boundary layer for the design of the thermal protection system due to the high heating rates under turbulent flow. Many thermal protection systems are carbon-based and introduce new species, specifically CO2, into the boundary layer flow which are known to dampen the instabilities that lead to transition for hypersonic vehicles. A Computation Fluid Dynamics study was accomplished examining the concentration of CO2 required to impact boundary layer transition over both sharp and blunt cones. These results were used in conjunction with air-carbon ablation models models to determine if these concentrations are possible through ablation alone and the impact on a flight representative vehicle transition. The study revealed that sufficient CO2 was present in the boundary layer at high enthalpy flow conditions to delay transition. Furthermore, a parametric study of the model uncertainties showed relative insensitivity to the gas-surface interaction model used but rather a high sensitivity to freestream flow parameters, vehicle geometry and surface temperature.

15. SUBJECT TERMS

hypersonic, transition, second mode damping, CO2 damping, thermal protection system, ablation models

16. SECURITY CLASSIFICATION OF:			17. LIMITATION OF ABSTRACT	18. NUMBER OF PAGES	19a. NAME OF RESPONSIBLE PERSON
a. REPORT	b. ABSTRACT	c. THIS PAGE			Dr. Robert B. Greendyke, AFIT/EN
U	U	U	UU	233	19b. TELEPHONE NUMBER *(Include area code)* (937) 255-3636 x4601 robert.greendyke@afit.edu

Reset

Standard Form 298 (Rev. 8/98)
Prescribed by ANSI Std. Z39.18

INSTRUCTIONS FOR COMPLETING SF 298

1. REPORT DATE. Full publication date, including day, month, if available. Must cite at least the year and be Year 2000 compliant, e.g. 30-06-1998; xx-06-1998; xx-xx-1998.

2. REPORT TYPE. State the type of report, such as final, technical, interim, memorandum, master's thesis, progress, quarterly, research, special, group study, etc.

3. DATES COVERED. Indicate the time during which the work was performed and the report was written, e.g., Jun 1997 - Jun 1998; 1-10 Jun 1996; May - Nov 1998; Nov 1998.

4. TITLE. Enter title and subtitle with volume number and part number, if applicable. On classified documents, enter the title classification in parentheses.

5a. CONTRACT NUMBER. Enter all contract numbers as they appear in the report, e.g. F33615-86-C-5169.

5b. GRANT NUMBER. Enter all grant numbers as they appear in the report, e.g. AFOSR-82-1234.

5c. PROGRAM ELEMENT NUMBER. Enter all program element numbers as they appear in the report, e.g. 61101A.

5d. PROJECT NUMBER. Enter all project numbers as they appear in the report, e.g. 1F665702D1257; ILIR.

5e. TASK NUMBER. Enter all task numbers as they appear in the report, e.g. 05; RF0330201; T4112.

5f. WORK UNIT NUMBER. Enter all work unit numbers as they appear in the report, e.g. 001; AFAPL30480105.

6. AUTHOR(S). Enter name(s) of person(s) responsible for writing the report, performing the research, or credited with the content of the report. The form of entry is the last name, first name, middle initial, and additional qualifiers separated by commas, e.g. Smith, Richard, J, Jr.

7. PERFORMING ORGANIZATION NAME(S) AND ADDRESS(ES). Self-explanatory.

8. PERFORMING ORGANIZATION REPORT NUMBER. Enter all unique alphanumeric report numbers assigned by the performing organization, e.g. BRL-1234; AFWL-TR-85-4017-Vol-21-PT-2.

9. SPONSORING/MONITORING AGENCY NAME(S) AND ADDRESS(ES). Enter the name and address of the organization(s) financially responsible for and monitoring the work.

10. SPONSOR/MONITOR'S ACRONYM(S). Enter, if available, e.g. BRL, ARDEC, NADC.

11. SPONSOR/MONITOR'S REPORT NUMBER(S). Enter report number as assigned by the sponsoring/ monitoring agency, if available, e.g. BRL-TR-829; -215.

12. DISTRIBUTION/AVAILABILITY STATEMENT. Use agency-mandated availability statements to indicate the public availability or distribution limitations of the report. If additional limitations/ restrictions or special markings are indicated, follow agency authorization procedures, e.g. RD/FRD, PROPIN, ITAR, etc. Include copyright information.

13. SUPPLEMENTARY NOTES. Enter information not included elsewhere such as: prepared in cooperation with; translation of; report supersedes; old edition number, etc.

14. ABSTRACT. A brief (approximately 200 words) factual summary of the most significant information.

15. SUBJECT TERMS. Key words or phrases identifying major concepts in the report.

16. SECURITY CLASSIFICATION. Enter security classification in accordance with security classification regulations, e.g. U, C, S, etc. If this form contains classified information, stamp classification level on the top and bottom of this page.

17. LIMITATION OF ABSTRACT. This block must be completed to assign a distribution limitation to the abstract. Enter UU (Unclassified Unlimited) or SAR (Same as Report). An entry in this block is necessary if the abstract is to be limited.